UNIVERSITY OF SOUTHAMPTON

FACULTY OF NATURAL AND ENVIRONMENTAL SCIENCES

CHEMISTRY

Volume 1 of 1

Optical and Mechanical Studies of the Air/Water Interface and Crystallisation Processes

by

Mr Matthew D Parsons

Thesis for the degree of Doctor of Philosophy

January 2018

UNIVERSITY OF SOUTHAMPTON

ABSTRACT

The air/water interface and crystallisation have long been challenging to study despite their crucial importance in many areas of modern science. They can be difficult to study without interfering in some way with the process being observed and once the work it can be very challenging to interpret the results which have been gathered. This work attempts to understand the air/water interface and other air/solvent interfaces using variable angle spectroscopic ellipsometry. The values of the complex refractive index which are measured give insight into the nature of these interfaces and the apparent differences between water and other solvents. Work has also been performed to study the process of crystallisation through second harmonic imaging microscopy and single crystal x ray diffraction. To bridge these two areas, p-Nitrophenol has been studied in depth, with a literature review of the surrounding work on the compound, as well as studies on the effects of irradiation on the α crystal polymorph. Finally, the growth of a p-Nitrophenol layer at the air/water interface has been studied using Langmuir Blodgettry and tensiometry to understand the rate and mechanism of the growth.

FACULTY OF NATURAL AND ENVIRONMENTAL SCIENCES

Chemistry

Thesis for the degree of Doctor of Philosophy

Optical and Mechanical Studies of the Air/Water Interface and Crystallisation Processes

Matthew David Parsons

Contents

Table of Tables vii

Table of Figures viii

List of Accompanying Materials xiv

Academic Thesis: Declaration Of Authorship xv

Acknowledgements xvi

Definitions and Abbreviations xvii

Chapter 1 - Introduction 1

1.1 – Interfaces 1

1.1.1 – Surface Tension 1

1.1.2 – Monolayers 2

1.1.3 – Langmuir Isotherm 4

1.1.4 – Air/Liquid Interfaces 5

1.1.5 – Air/Water Interface 6

1.2 – Crystals 6

1.2.1 – Unit Cell 7

1.2.2 – Symmetry 7

1.2.3 – Polymorphism 7

1.3 – Light 8

1.3.1 – Anisotropy 8

1.3.2 – Reflection and Refraction 8

1.3.3 – Fresnel Equations 9

1.3.4 – Complex Reflectance Ratio 9

1.3.5– Brewster Angle 10

1.3.6 – Stokes Parameters 11

1.3.7 – Second Harmonic Generation 12

1.3.8 – Mechanism 12

1.3.9 – Phase Matching 14

Chapter 2 – p-Nitrophenol Literature Review 15
2.1 – Chemical Structure 15
2.2 – Crystal Structure 16
2.3 – Uses 17
2.4 – Surface Second Harmonic Generation 18
2.5 – Surface Activity 21
2.6 – Thermal Instability 21
2.7 – Photostability 22
2.8 – Pollutant Studies 25
Chapter 3 – Experimental Techniques 26
3.1 – Second Harmonic Imaging Microscopy 26
3.1.1 – Laser 26
3.1.2 – Optical Path 26
3.1.3 – Detection 27
3.1.4 – Piezoelectric Stage 27
3.1.5 – Data Acquisition 27
3.1.6 – Noise Removal 30
3.2 – Langmuir Blodgettry 32
3.2.1 – Wilhelmy Plates 33
3.2.2 – Langmuir Blodgett Experimental 33
3.2.3 – Experimental Sensitivity to Environment 34
3.2.4 – Compression 35
3.3 – Tensiometry 36
3.3.1 – Tensiometer Experimental 36
3.3.2 – Volume Sensitivity 36
3.4 – Ellipsometry 37
3.4.1 – Theory 37
3.4.2 – Experimental Procedure 38

3.4.3 – Alignment 38

3.4.4 – Psi and Delta 40

3.4.5 – Liquid Ellipsometry 41

3.4.6 – Anti-Vibration control 42

3.5 – Single Crystal X Ray Diffraction 42

Chapter 4 - Crystal Growth Studies 44

4.1 – Crystal Sample Growth 44

4.2 – PNP Irradiation 45

4.3 – Single Crystal X Ray Diffraction Sublimation Experiment 47

4.4 – Conclusions and Further Work 50

Chapter 5 – Second Harmonic Imaging Microscopy 52

5.1 – Amplitude Data 52

5.1.1 – Amplitude Variance 54

5.1.3 – Low Intensity Images 55

5.2 – Crystallisation Experiment 55

5.3 - Equipment Malfunction 58

5.4 – Conclusions and Further Work 58

Chapter 6 – p-Nitrophenol Study 59

6.1 – Small Langmuir Blodgett Trough Work 59

6.1.1 – 15 mM Data 59

6.1.2 – Short and Long time scale growth 59

6.2 – NIMA Trough Experiments 61

6.2.1 – Sample Preparation 62

6.2.2 – Open trough 62

6.2.3 – Area Isotherms 63

6.2.4 – T1 and T3 Isotherm Equilibration 64

6.3 – Curve Fitting 67

6.3.1 – Short Time Scale 67

6.3.2 - Nonlinear Long Term Growth 70

6.3 – Tensiometry 71

6.3.1 – Surface Tension Change by Concentration 71

6.3.2 – PNP Literature Comparison 72

6.3.3 – Surface Pressure Conversion 72

6.4 – Surface Data Analysis 73

6.4.1 - Surface Growth Mechanism 73

6.4.2 - Micelles and Multilayers 74

Chapter 7 – Air/Solvent Interface Ellipsometry 76

7.1 Water Ellipsometry Data 77

7.1.1 - 70° AOI 77

7.1.2 - Brewster Angle Ellipsometry 78

7.1.3 – Change in Δ in Brewster Angle Ellipsometry 81

7.1.4 – Variance in Delta Data for Water 82

7.1.5 - Variable Angle Spectroscopic Ellipsometry 82

7.1.6 – High Resolution Variable Angle Spectroscopic Ellipsometry 84

7.2 Organic Solvent Data 90

7.2.1 – Solvent Choice 90

7.2.2 – Experimental Data 90

7.2.3 – Water/Ethanol Mixtures 92

7.3– Water Impurities 96

7.3.1 – Water Purity 96

7.3.2 – Acid and Alkali Impurities 97

7.3.3 –Salt Impurities 97

7.4 – PNP Ellipsometry 102

7.4.1 – 70° Angle of Incidence 102

7.4.2 – Brewster Angle 102

7.4.3 – Titration 104

7.5 – Simulation Data 106

7.6 Conclusions and Further Work 111

Chapter 8 – Final Conclusions 112

Table of Tables

Table 1 – Crystal properties of PNP polymorphs 16
Table 2 – Varying volume of water to test variability in surface tension 37
Table 3 – Samples grown for SHIM by slow crystal growth. 45
Table 4 – Fit parameters for first order time dependent Langmuir 68
Table 5 – Water/Ethanol solutions used in variable angle spectroscopic ellipsometry by mole and mass percentage 92

Table of Figures

Figure 1 – Stearic acid 3
Figure 2 – Increasing organisation of monolayer with increasing surface concentration. 3
Figure 3 – Simple air/liquid interface profile showing the gradual increase in density from near 0 for air, up to the density of the liquid. The interfacial region is a phase made of loosely bound solvent molecules at a lower density to the bulk. 6
Figure 4 – Multiple reflections from a thin film. 10
Figure 5 – Brewster angle illustration 10
Figure 6 – Mechanism of SHG showing virtual energy levels 13
Figure 7 – Acid/base equilibrium for PNP 15
Figure 8 – Tautomeric forms of PNP 15
Figure 9 – UV/Vis spectrum two PNP solutions in acidic and basic conditions. 16
Figure 10 – PNP and three of its derivatives. 18
Figure 11 –p-Nitrophenylphosphate 18
Figure 12 – Second Harmonic Intensity vs PNP solution pH. Reproduced from citation[68]. 19
Figure 13 – Intermolecular bonding of PNP polymorphs, β polymorph top, α polymorph bottom. Reproduced from citation[85]. 23
Figure 14 – ONP rearrangement leading to HONO photolysis. 24
Figure 15 – Laser table schematic – 1, laser, 2, interlock, 3, chopper, 4, Fresnel rhomb, 5, linear polariser, 6, faraday isolator, 7, iris, 8, front telescope lens, 9, rear telescope lens, 10, iris, 11, periscope, 12, microscope 28
Figure 16 – Microscope schematic representing object 12 in Figure 15, where 1, dichroic mirror, 2, sample, 3, mirror with backlight, 4, 400 nm filter, 5, rotatable optic for either 100% of light to camera, 100% of light to detector or 50/50 split, 6, optical camera, 7, mirror, 8, optional ND filter, 9, 400 nm filter, 10, pinhole, 11, fW detector. 29
Figure 17 – Quadratic relationship between laser power and SH signal 31
Figure 18 – 40 µm images of Methylbenzylaminonitropyridine (MBANP) Melt on glass slide. Top left, Camera image; top right, amplitude; bottom, phase. See Chapter 5 for further details 31
Figure 19 – LB Trough schematic: 1 - LB trough, 2 - liquid subphase, 3 - monolayer, 4 - Wilhelmy plate, 5 - Electrobalance, 6 - Barrier, 7 - Barrier Controller, 8 - Computer. 32
Figure 20 – Representation of a Wilhelmy Plate. 32
Figure 21 – Surface Pressure spikes caused by air movement highlighted by arrows. 35
Figure 22 – Tensiometer Schematic. 1, Tensiometer Enclosure, 2, liquid subplase, 3 monolayer, 4, sample holder, 5, platinum wire, 6, electrobalance, 7, height control, 8, computer. 36

Figure 23 - Ellipsometer Schematic: 1 - Sample, 2 - Xenon Lamp, 3 - Monochromator, 4 - Polariser, 5 - Photoelastic Modulator, 6 - Analyser, 7 - Detector, θ is the angle of incidence. 38
Figure 24 – Angle reference data collected over one month for Brewster angle of glass. 40
Figure 25 – Comparison of Ψ and Δ data at 70° AOI for water and 30 mM PNP solution. Ψ is plotted as a solid line, Δ as scatter plot. 41
Figure 26 – X ray diffraction. 43
Figure 27 – PXRD spectra of MBANP samples. Due to the much higher intensity of the red data set for methanol, the y axis was limited to 10000 in order to see the other data clearly. 45
Figure 28 – Urea crystal used in SCXRD sublimation experiment glued to goniometer tip. Top left, front view before experiment, bottom left, side view before experiment, top right, front view after experiment, bottom right, side view after experiment. 48
Figure 29 – SCXRD pattern from experiment 1 showing Bragg and non-Bragg diffraction. 49
Figure 30 – SCXRD pattern from experiment 8 with analysed spot highlighted. Fewer Bragg peaks are still visible, with weak non-Bragg diffraction in between them. 49
Figure 31 – Crystal thickness vs Peak intensity over eight experiments. 50
Figure 32 – SHIM image of different sections of a DAN crystal. Left images are optical camera images, right images are amplitudes of the SH signal from the lock in amplifier. Top images show the corner of the crystal. Bottom images show the edge of the crystal. 53
Figure 33 – Two SHIM images: MBANP melt (top) and MBANP crystal edge (bottom). Left images are optical camera images, right images are amplitudes of the SH signal from the lock in amplifier. 54
Figure 34 – SHIM images of two samples: the edge of a DAN melt crystal (top) and the edge of a thin DAN melt (bottom). Left images are optical camera images, right images are amplitudes of the SH signal from the lock in amplifier. 55
Figure 35 – Recrystallisation of urea. SH spot can be seen in image centre left as a purple spot. 57
Figure 36 – Laser Burn on crystal in centre left of image highlighted by an arrow. 57
Figure 37 – Surface pressure change for a 15 mM PNP solution over 2.5 hours. 59
Figure 38 – Surface pressure data for a 70 mM PNP solution which has been sonicated. From 0 to 8000 s, the exponential-like curve is seen, giving way to a linear surface pressure increase after this. 60
Figure 39 – Three surface pressure data sets trending towards the same growth rate for 15 mM PNP solutions. Black shows the same data as in Figure 37, while the red and blue curves show data sets where the exponential-like growth was not observed due to a preformed structure at the surface before the start of the experiment. The red data set shows an initial decrease in surface pressure due to the solution cooling slightly at the start of the experiment. 61

Figure 40 – Flow chart of experimental work for NIMA trough 62
Figure 41 – Surface Pressure data for open trough. The surface pressure is increasing at the same rate as the other 15 mM solutions shown in Figure 39. 63
Figure 42 – Area isotherms for 15 mM PNP solution. The black and blue curves show the compression and expansion immediately after being placed in the trough, showing no surface pressure increase. The red curve shows a compression after 4 hours where the expansion did not correctly execute. The green and cyan curves show the compression after 6 hours equilibration in the trough, with the maximum surface pressure change. 64
Figure 43 – T1 Compression and subsequent equilibration. This is shown in red in Figure 42. The trough was compressed to 80 cm^2 over the first 600 s shown. Subsequently the expansion did not occur as intended, instead the layer remained compressed, and equilibration of the surface PNP back into the bulk was observed as the surface pressure decreased. 65
Figure 44 – Surface pressure change over 12 hours of the compressed surface layer. The PNP at the surface is returning to the bulk due to the increased surface concentration after compression. 66
Figure 45 – First order time dependent Langmuir fitting for the 15 mM data shown in Figure 37. Each graph shows the first order Langmuir fit from the start of the experiment through to a different time. The fit is shown in red for each case and the difference between the experimental data and fit is shown in yellow. 67
Figure 46 – Deviation between experimental and fit for 15 mM data. Beyond t = 10000 s, the data is generated from the gradient calculated from the data for 15 mM shown in Figure 39 and Figure 41. The first order Langmuir fit does not fit to this long term linear growth, but tends towards 6.5 mN/m. 68
Figure 47 – Combination fit of time dependent Langmuir and zero order with K' = 5.315, k_0 = 0.0001414 and K_a = 0.0005686. 69
Figure 48 – First order Langmuir and $t^{1/2}$ fit for the surface pressure data shown in Figure 37 with an added linear section calculated from the gradients of the lines shown in Figure 39. K' = 3.165, k_1 = 0.0008325 and K_a = 0.03591. 70
Figure 49 – Combination of surface tension data of PNP from various sources. The three lines represent data collected by Paluch and Filek. The Xs show tensiometry data collected by researchers at KTH and the Os show data collected in this work. Both the KTH data, and data for this work show a greater change in surface tension with respect to concentration than the literature data, and a range of surface tension values can be seen for each concentration. 71
Figure 50 – Surface pressure by concentration for tensiometry calculated from the difference between the highest surface tension value for each concentration, and each other point. The

maximum surface pressure seen increases with concentration, though two points with a surface pressure greater than 10 mN/m can be seen for 15 and 70 mM. 72
Figure 51 – Some highlighted trends in the surface pressure data as bolder lines in red, orange, purple and green. These represent higher concentrations of PNP at the surface, and greater levels of organisation. 74
Figure 52 – Four data sets for Ψ (left) and Δ (right) for deionised water at a 70° angle of incidence. 78
Figure 53 – Ψ (left) and Δ (right) data for Brewster Angle Ellipsometry of deionised water. The angle of incidence was set at 52.9° and the wavelength was varied from 200 to 800 nm. 79
Figure 54 – Ψ (top) and Δ (bottom) data for Brewster Angle Ellipsometry at different angles of incidence for deionised water. Ψ is plotted as a scatter plot for each data set, with a moving average of 5 points plotted as a solid line to highlight the trend. The maximum values of Ψ are less than in Figure 53 due to the proximity to the Brewster angle, but the noise levels within the data are equivalent. 80
Figure 55 – Polar plot of Δ of water at 52.9° angle of incidence. Wavelength is displayed on the radius of the plot, and Δ is displayed around the edge of the circle. Since Δ is expressed as an angle, it can be seen that 0° = 360°. 81
Figure 56 – Δ of deionised water showing a transition to both 0° and 360° at a recorded angle of incidence of 53.1°. 82
Figure 57 – Variable angle spectroscopic ellipsometry data of deionised water. Ψ is plotted as a solid line with + symbols denoting the data points. Δ points are plotted as circles. The Brewster angle is observed at 53°. Δ transitions from 180° to 360°. 83
Figure 58 – High resolution variable angle spectroscopic ellipsometry data for deionised water. Ψ is plotted as a solid line with + symbols denoting the data points. Δ points are plotted as circles. The transition through the Brewster angle can be seen with Δ going from 0° to 360°. 84
Figure 59 – Variable angle spectroscopic ellipsometry data for deionised water. The top figure shows Ψ data and the bottom figure shows Δ. Three data sets are plotted in different colours: black, blue, and red. Each data set was collected under the same conditions, each two days apart. All three data sets show Δ transition to 360°. The data sets in red and blue are near identical, while the black data set is slightly offset. This is likely caused by the systematic inaccuracy of the angle of incidence. 86
Figure 60 – Variable angle spectroscopic ellipsometry data for two samples of deionised water. Both data sets show near identical values of Ψ, while Δ transitions to 360° for one sample, and 0° for the other. 88

Figure 61 – Variable angle spectroscopic ellipsometry data for two samples of deionised water. The data set depicted in blue shows distinctly different data than was otherwise observed. Ψ and Δ both transition very slowly through the Brewster angle. 89
Figure 62 – Variable angle ellipsometry data for water, Ethanol, Methanol and Dodecane. Ψ plotted as a line with + symbols denoting data points, Δ is depicted as circles. For all experiments, theta passes through the Brewster angle of the liquid causing a 180° shift in Δ. In the case of water, this transition passes upwards to 360°, while the other three solvents tested transition downwards to 0°. 90
Figure 63 – Top, Ψ and Δ data for water (52.9°) from Greef 2008 paper. Bottom, Δ data for organic solvents, from left to right, with their angles of incidence, paraffin (56°), DMSO (55.8°), ethanol (53.7°), dodecane (54.7°) from Greef 2008 paper. 91
Figure 64 - Ψ (top) and Δ (bottom) data for low percentage water/ethanol mixtures. The values of theta are not precise due to the imprecision in measuring the angle of incidence of the ellipsometer. The change from Δ transitioning from 360° to 0° can be seen at 0.5 mol%. 93
Figure 65 - Ψ (Top) and Δ (Bottom) data for deionised water and water/ethanol mixtures from 1 mol% up to 100 mol%. Due to the number of data sets for Δ, each data set is highlighted with a line. The Brewster angle can be seen to shift towards the value for ethanol as the concentration of ethanol increases. 94
Figure 66 – Comparison of surface and bulk properties by percentage mass ethanol. Dashed line shows y=x. The bulk properties of density and freezing point mostly stay below the dashed line, while the surface properties increase at a much greater rate with a lower percentage of ethanol. .. 95
Figure 67 - Ψ and Δ data for different purity of waters. Ψ is shown as a solid line, while Δ is shown as a scatter plot. Deionised water and tap water show Δ transition to 360°, while the higher purity water samples show Δ transition to 0°. 96
Figure 68 – Comparison of Ψ and Δ data for ion chromatography purity water and deionised water mixture. Ψ is shown as a solid line, while Δ is shown as a scatter plot. Addition of deionised water to ion chromatography water alters the Δ transition from 360° to 0°. 98
Figure 69 – Ψ (left) and Δ (right) data for HCl solutions in IC water. A change in the recorded values for Δ is seen between 100 µM and 1 mM. 99
Figure 70 – Ψ (top) and Δ (bottom) data for NaOH solutions in IC water. Both 1mM and 10 mM show Δ transition to 360°. 100
Figure 71 – Comparison of Ψ (top) and Δ (bottom) data for three neutral salts in IC water at 1 mM. At this concentration, only $CaCO_3$ had an observable impact at the surface. 101

Figure 72 - Ψ (left) and Δ (right) data for 15 mM PNP solution at 70° AOI with UVVis spectrum of a PNP solution in water overlaid in blue. Δ is close to 360° across the entire spectrum since the experiment was performed far past the Brewster angle. 102
Figure 73 - Ψ (solid line with +s) and Δ (circles) data for a 15 mM PNP solution. 103
Figure 74 - Ψ (solid line) and Δ (scatter plot) data of a 15 mM PNP solution at 52.9° angle of incidence. 103
Figure 75 - Ψ data for the titration of a 30 mM PNP solution. The solution started at a pH of 4.62, and an alkaline solution of PNP was added between each run and the pH was remeasured. 104
Figure 76 – Δ data for the titration of the same 30 mM PNP solution described in Figure 75 105
Figure 77 – Two intrinsic surface models for a simulated surface. The blue dots show molecular positions and the red mesh indicates the location of the intrinsic surface. The top image shows a loose fit to the molecular locations, while the bottom image is much higher resolution. 107
Figure 78 – Density profiles for water (top) and methanol (bottom) for different resolutions of the intrinsic surface. q_m is the resolution of the intrinsic surface, z is the distance through the simulation and ρ(z) is the density. Increasing resolution of the intrinsic surface in both cases leads to a higher surface density peak as the surface is more tightly constrained to the surface molecule location... 109
Figure 79 – Calculated refractive indices of the simulations of water (top) and methanol (bottom) for different resolutions of the intrinsic surface. n_0 and n_e are the calculated refractive indices for the ordinary and extraordinary polarisations of light. These values were calculated using the Clausius-Mosetti-Lorenz-Lorenz method. At high resolutions there is a noticeable increase of the refractive index for water, which is not observed for methanol. 110
Figure 80 – Example images collected by SHIM of MBANP crystals. Left images show optical images, right images show second harmonic intensity. Top images show a small MBANP crystal, bottom images show the edge of a larger crystal. 112
Figure 81 – Left, surface pressure data of a 15 mM solution of PNP over four hours, initial growth is a time dependent first order Langmuir, while this gives way to a pseudo linear step. Right, tensiometer data for PNP solutions with respect to concentration, showing the increasing potential surface pressure change with as the concentration increases. 114
Figure 82 – Left, Polar plot of a Brewster angle ellipsometry experiment on deionised water showing a transition from 180° to 360°. Right, variable angle ellipsometry experiments showing the effect of purity on the measurement of Δ. Both high purity waters show a transition to 0°, while the lower purity samples show a transition to 360°. 115

List of Accompanying Materials

Zip file, “Crystallising Videos.zip”, containing three .mp4 video files, “Crystallising 1.mp4”, “Crystallising 2.mp4” and “Crystallising 3.mp4” pertaining to section 5.2.

Academic Thesis: Declaration Of Authorship

I, Matthew D Parsons

declare that this thesis and the work presented in it are my own and has been generated by me as the result of my own original research.

Optical and Mechanical Studies of the Air/Water Interface and Crystallisation Processes

I confirm that:

1. This work was done wholly or mainly while in candidature for a research degree at this University;
2. Where any part of this thesis has previously been submitted for a degree or any other qualification at this University or any other institution, this has been clearly stated;
3. Where I have consulted the published work of others, this is always clearly attributed;
4. Where I have quoted from the work of others, the source is always given. With the exception of such quotations, this thesis is entirely my own work;
5. I have acknowledged all main sources of help;
6. Where the thesis is based on work done by myself jointly with others, I have made clear exactly what was done by others and what I have contributed myself;
7. None of this work has been published before

Signed: .....

Date: .....

Acknowledgements

Many thanks to my family and friends who have helped me through this work. Thanks to Adam, Ed, Duncan, Jess and Rich for their friendship and support over the years. Thanks to Frank for his help and very useful discussions regarding the ellipsometry experiments performed for this work and how they related to his simulations of the air/water interface, as referenced in chapter 7. Thanks to Matthew for his support and for hosting me at Cranfield University to perform Langmuir Blodgettry and tensiometry experiments. Many thanks to my supervisor Jeremy for his endless help and enthusiasm to push me onwards.

Finally, thanks to my family, my parents, Gerard and Vicki, for all their support to get me this far, my brother and sister-in-law, Jon and Rachel, and my nieces, Florence and Clara for keeping me distracted as I finish this thesis.

Definitions and Abbreviations

BBO – β-barium borate

CMC – Critical micelle concentration

DAN - 4-(N,N-Dimethylamino)-3-acetamidonitrobenzene

CTAB - cetyltrimethylammonium bromide

Δ – delta, imaginary component of the complex refractive index

γ – surface tension

γ_P – surface pressure

HSM – Hot stage microscopy

k – Extinction coefficient

LB – Langmuir Blodgett

MBANP - Methylbenzylaminonitropyridine

MHB – Methyl p-hydroxybenzoate

n – Refractive Index

NLO – Nonlinear Optics

NMBA - 4-nitro-4 -methyl benzylidene aniline

ONP – o-Nitrophenol

PEM – Photoelastic Modulator

PNP – p-Nitrophenol

Ψ – psi, real component of the complex refractive index

PTFE - Polytetrafluoroethylene

PXRD – Powder x ray diffraction

SCXRD – Single crystal x ray diffraction

SH – Second harmonic

SHG – Second harmonic generation

SSH – Surface second harmonic

SSHG – Surface second harmonic generation

TBP – Tributyl phosphate

UV – Ultraviolet

Chapter 1 – Introduction

Crystallisation is a key part of modern chemistry. This work aims to study crystallisation and study crystals through a variety of techniques. Initial work looks at the growth of crystals in two opposing directions. Second harmonic imaging microscopy work aims to study the growth of crystals through their second harmonic generation, while single crystal X ray diffraction experiments study the sublimation of urea, and the relationship between Bragg and non-Bragg diffraction as the size of the crystal changes.

Crystallisation occurs at nucleation points, often at interfaces. p-nitrophenol for example commonly starts crystallising at the air/water interface. This is preceded by the growth of a surface layer, which can be observed by the effect it has on the surface tension of the solution over time. This work aims to study this layer as it forms at the interface through Langmuir Blodgettry, tensiometry and ellipsometry to understand the rate, and mechanism of its growth and use this information to provide insights into the nature of the solution before crystallisation begins.

Finally, since crystallisation commonly occurs at interfaces, this work aims to look at the air/water interface through the lens of ellipsometry. To properly understand crystallisation at the air/water interface, it is important to have a sound model of the interface. Past ellipsometry work has indicated that there is a layer of higher density than the bulk at the air/water interface and this work aims to investigate this phenomenon further along with the effects of impurities on the interface in order to build a more accurate model for the surface of water.

1.1 – Interfaces

Interfaces are the boundaries between two different media. Interfaces are important chemically as the point where many chemical processes take place, such as chemical deposition. Surface science covers what occurs at many different types of interface, including solid/liquid, liquid/gas and solid/vacuum, however of particular interest to this project is the air/water interface, as well various air/organic solvent interfaces.

1.1.1 – Surface Tension

At gas/liquid interfaces, surface tension is a very important force. This is the elastic tendency of a liquid to try and minimise its surface area[1], caused by the attractive intermolecular forces between the molecules of the liquid[2]. Water, for example has a particularly high surface tension of 72.4 mN/m at 293 K[3], caused by strong hydrogen bonding. Most organic solvents have a much lower surface tension, ethanol and acetone have values of 22.2 and 25.2 mN/m[4,5] respectively due to

weaker intermolecular forces. Even in these cases however, the solvent-solvent intermolecular forces are much more energetically favourable than solvent-gas interactions.

In the bulk of a liquid, a given molecule experiences an equal force in all directions since it is completely surrounded by other equivalent solvent molecules. Comparatively, at the surface, molecules are not completely surrounded, and as such experience an inwards pressure. This pressure is minimised when the liquid has a minimum area, leading to liquids forming spherical shapes since this has the highest volume to surface area ratio.

Surface tension is responsible for many properties of liquids, and are especially notable for water, due to its high surface tension. For example, surface tension allows small objects which are denser than water to float at the air/water interface if they are light enough to be carried by the force of surface tension. This can be seen with pond striders sitting on the water surface[6]. Additionally the difference between the solvent-solvent interactions and solvent-medium interactions governs the contact angle at the interface[7], unfavourable solvent-medium interactions will lead to beading, as can be seen for water droplets on waxy surfaces, the solvent minimises the contact with the hydrophobic medium.

Surface tension is an important property because it can be indicative of properties of the surface and the bulk[8]. Probing the surface tension can therefore give information of the environment at the surface, as well as a way of looking deeper into the bulk of the material. Many methods have been developed to measure surface tension, or a related property, surface pressure. Surface pressure is the negative change in surface tension. It is useful for measuring the change over time in surface tension, when the absolute values are not needed, or can be otherwise determined.

$$\gamma_0 - \gamma_t = \gamma_p \qquad \textbf{(1.1)}$$

Where γ_0 is the surface tension at time = 0 γ_t is the surface tension at time = t and γ_p is the surface pressure at time = t. Different methods have different use cases, either by having better accuracy at certain surface tension ranges, or for collecting over different time scales. As a result, surface tension can be measured over a range of milliseconds using the oscillating jet method[9], up to several hours using Langmuir Blodgettry[10,11].

1.1.2 – Monolayers

Many compounds have a tendency to adsorb at interfaces due to more a favourable chemical environment. These are known as surfactants, a shortening of “surface active agents”. Surfactants lower the surface tension of the liquid, since they disrupt the chemical environment at the surface[12].

Many surfactants are organic compounds with a hydrophilic “head” and an amphiphilic “tail”[13,14]. Long chain fatty acids such as stearic acid are a typical example. Stearic acid is a carboxylic acid with an eighteen carbon chain[15,16]. At the air/water interface, its hydrophilic carboxylic acid head group orients itself towards the water, while the long alkyl tail points away. At high surface concentrations of stearic acid, the alkyl chains line up together, stabilising through Van de Waals forces. This ability for organisation highlights another requirement to be a surfactant. Compared to other surface active compounds such as mid and long chain alcohols which decrease the surface tension of water, surfactants must be able to undergo orientation into organised structures such as micelles at high surface concentrations[17].

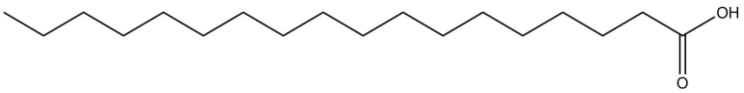

Figure 1 – Stearic acid

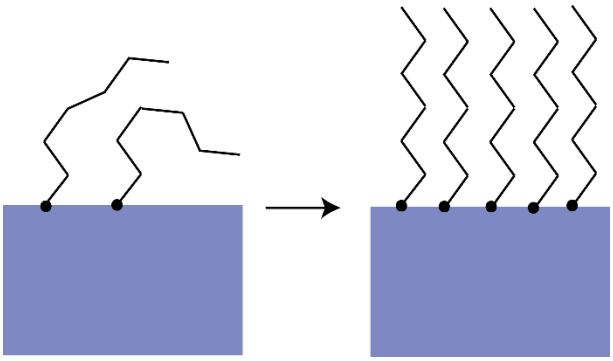

Figure 2 – Increasing organisation of monolayer with increasing surface concentration.

Micelles are surfactant structures which start to occur in solution at the critical micelle concentration (CMC)[18,19]. Micelles are aggregates of surfactant molecules in solvent, for example forming spherical structures with the head groups at the surface and the tail groups in the centre. Additionally, certain compounds area able to form multilayers at the surface at high surfactant concentration[20,21]. These layers form with the hydrophobic tails lined up inside the bilayer and the hydrophilic heads pointing outwards.

Two methods are commonly used to create monolayers at the air/water interface, spreading[22] and self-assembly[23]. Spreading is useful for surfactants which are at most, sparingly soluble in water. It consists of dissolving the surfactant in a solvent which is immiscible with water and adding it slowly to the surface of the solution, allowing each drop to fully evaporate before adding the next. This causes the surfactant to form a layer at the interface since it will not dissolve into the water. Immiscible solvents should be used to ensure that it completely evaporates, rather than mixing with the bulk solvent, and thus, all of surfactant is left at the surface. The concentration of this layer can

be calculated from the volume and concentration of the solution used, and the surface area of the solution. These layers can then be characterised and studied, or used for practical purposes such as coating another material[24,25].

Certain compounds can also assemble at the interface from the bulk solution[23]. This is mostly studied at the liquid/solid interface or solid/vacuum interface. Techniques such as a chemical vapour deposition involve the growth of thin films on semiconductors[26].

1.1.3 – Langmuir Isotherm

The most widely used description for the formation of monolayers is the Langmuir adsorption isotherm. This was proposed by Irving Langmuir in 1916[27] as a method to describe how gaseous molecules stick to surfaces rather than rebounding elastically. This relationship finds the maximum surface coverage of the adsorbate at the surface for a given pressure. This behaviour can be applied to monolayers at the air/water interface as well, if the following assumptions are deemed applicable. The adsorbate must be treated as an ideal gas with no interactions between adsorbate molecules. The surface is treated as flat, with all sites on the surface being equivalent, and able to hold one adsorbate molecule. Finally, the process of adsorption is treated as a chemical reaction between the adsorbate and the surface site. Assuming that these conditions are true, the rate of adsorption and desorption can be stated as the following two rate equations.

$$r_{ad} = k_{ad}\, c\, [S] \qquad \textbf{(1.2)}$$

$$r_{des} = k_{des}\, [A_{ad}] \qquad \textbf{(1.3)}$$

Where r_{ad} and r_{des} are the rate of adsorption and desorption respectively, k_{ad} and k_{des} are the rate constant of adsorption and desorption respectively, c is the concentration of the adsorbate, A, in the bulk solution, [S] is the concentration of free sites, and $[A_{ad}]$ is the concentration of A adsorbed at the surface. At equilibrium, these two rates are equal.

$$k_{ad}\, c\, [S] = k_{des}\, [A_{ad}] \qquad \textbf{(1.4)}$$

$$\frac{[A_{ad}]}{c\, [S]} = \frac{k_{ad}}{k_{des}} = K_{eq} \qquad \textbf{(1.5)}$$

Where K_{eq} is the equilibrium constant. The total number of sites can be defined as the sum of the free sites and adsorbed sites. Rearranging the above equation for [S], and substituting into this expression gives the following:

$$[S_0] = [S] + [A_{ad}] \qquad \textbf{(1.6)}$$

$$[S_0] = \frac{[A_{ad}]}{c\,K_{eq}} + [A_{ad}] = \frac{1 + c\,K_{eq}}{c\,K_{eq}}[A_{ad}] \quad \textbf{(1.7)}$$

Defining the surface coverage, θ_A, as the concentration of adsorbed sites divided by the total number of sites, and substituting this in gives:

$$\theta_A = \frac{[A_{ad}]}{[S_0]} \quad \textbf{(1.8)}$$

$$\theta_A = \frac{c\,K_{eq}}{1 + c\,K_{eq}} \quad \textbf{(1.9)}$$

This yields an expression for the surface coverage for a given material, at a partial pressure. The surface coverage is a percentage, so varies between 0 and 1. It can be seen that if c or K_{eq} is very low, θ_A will tend towards 0, whereas at high values of these variables, the surface coverage will near 1.

The rate of growth of a Langmuir monolayer over time can be described as follows[28].

$$\frac{d\theta}{dt} = k_{ad}(1 - \theta)c - k_{des}\theta \quad \textbf{(1.10)}$$

Integration of equation 1.10 with respect to time gives the following equation.

$$\theta(t) = \frac{c}{c + \left(\frac{k_{des}}{k_{ad}}\right)}(1 - \exp(-(k_{ad}c + k_{des})t)) \quad \textbf{(1.11)}$$

This can be simplified down to the following.

$$\theta(t) = K'(1 - \exp(-K_a t)) \quad \textbf{(1.12)}$$

This gives an expression for the formation of a Langmuir monolayer with respect to time.

1.1.4 – Air/Liquid Interfaces

Air/liquid interfaces exist at the boundary between liquids and gases. The simplest model for an interface consists of two phases which have an ideal surface phase of 0 thickness between them. This was initially proposed by Gibbs[29]. More realistic models for the density of a liquid interface involve a surface phase which transitions from one medium to the other, as shown in Figure *3*. The density of the liquid tapers down gradually to that of the atmosphere, with the interface region comprised of the liquid molecules in a loosely bound state.

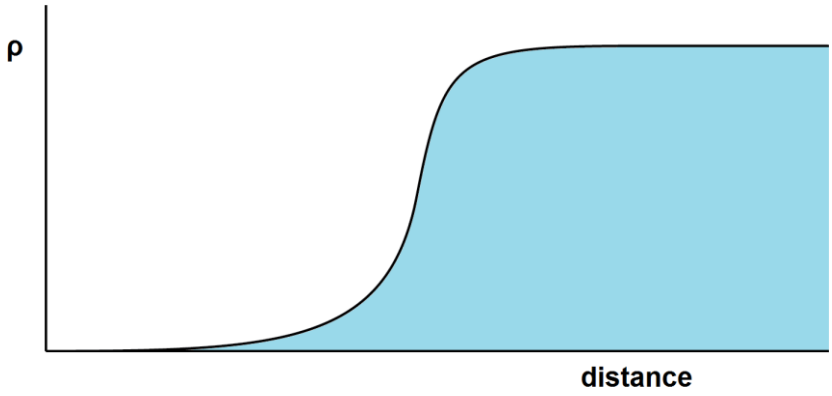

Figure 3 – Simple air/liquid interface profile showing the gradual increase in density from near 0 for air, up to the density of the liquid. The interfacial region is a phase made of loosely bound solvent molecules at a lower density to the bulk.

1.1.5 – Air/Water Interface

Water has long been noted for its strange properties, for example, looking at other group 6 hydrates, it would be expected that water would be gaseous at room temperature and pressure, rather than liquid due to its low molecular weight. However, due to the strong hydrogen bonding which occurs, water has much stronger intermolecular bonding than similar compounds such as H_2S, and is therefore liquid at room temperature.

The air/water interface has proved hard to study due to the high sensitivity of the surface to environmental parameters such as temperature and pH[3,30]. This can cause problems in knowing the exact properties of the surface being studied, for example absorption of atmospheric CO_2 can easily increase the pH of pure water. Additionally, different techniques probe the interface to different depths, with some techniques such as sum frequency generation vibrational spectroscopy probing a single molecular layer[31], to other techniques which look much deeper into the sample.

The exact structure of the air/water interface is thus not well understood, as evidenced by the difference of opinion between experimentalists and theoreticians regarding the charge [32,33]. Experimental results since 1861 have suggested that the water surface has a negative charge due to air bubbles migrating to the positively charged electrode in an electrophoresis cell, as well as many experiments since[34]. Simulations however have traditionally found the opposite, giving the surface of water a positive charge, with an acidic pH around 4.8[32]. One thing which is clear however that the surface of water appears to be a more complex system than other liquids.

1.2 – Crystals

Crystals are a highly ordered solid form of matter. The simplest crystals are composed of single atoms arranged in cubic close packed structures, such as NaCl, however much more complex

compounds can form also crystals such as proteins[35]. Regardless of the compound, crystals obey the following rule, they are made of a repeating microscopic structure which extends in all directions from a given point. This differentiates crystals from other amorphous solids which do not have this high level of order. Polycrystalline materials are common in the real world, they are made from multiple crystals which fuse together during crystal growth. This is different to single crystals which are formed from one nucleation.

1.2.1 – Unit Cell

The unit cell of a crystal is the smallest repeating unit which wholly encapsulates the symmetry of the structure. This is important because it contains all of the information of the crystal structure required to build the crystal by repeatedly translating the unit cell through space. As they describe a volume, the unit cell of a crystal consists of three lengths, a, b and c of the three axes, and three angles, α, β and γ for the angles between them. This gives the size and shape of the unit cell. The variations of these values give fourteen Bravais lattices, the simplest of which is a=b=c, α=β=γ=90° for a cubic system, and the most complex of a≠b≠c, α≠β≠γ≠90° for a triclinic system[36].

Miller indices are used to define planes through a crystal. They have three integer values, l, m and n which are orthogonal to each other, and are, in cubic cells, aligned with the axis of the unit cells. The value indicates the number of times the plane intercepts the unit cell in one unit cell length. Therefore, the (1 2 0) would intercept the a axis once per cell length, twice per b axis length and it would be parallel to the c axis. It is possible to have negative integers within a Miller index, since it can be seen that a (1 1 1) plane would be different to a (1 -1 1) plane, however two indices where all the numbers are the same, but of a reverse sign will be equivalent, such as (1 -2 0) and (-1 2 0)[36].

1.2.2 – Symmetry

There are many symmetry elements which can occur within a crystal structure, such as planes of symmetry and axes of rotation. These occur when applying this symmetry element to the unit cell results in the exact same structure. Centres of inversion are of particular interest to this work[37]. Centres of inversion are points within the unit cell through which the entire structure can be inverted to retain the same structure. The space group of a crystal gives the full description of all of the symmetry elements present within a crystal[38].

1.2.3 – Polymorphism

Polymorphism occurs when a compound is capable of crystallising in multiple different crystal structures[39]. This is caused by the molecules packing together in a different fashion, leading to different space groups or unit cells between the two polymorphs. There are many conditions which

can affect which polymorph of a compound forms. Most commonly observed are the effects of temperature of crystallisation and the solvent used. Other conditions such as the pH, presence of impurities or a voltage across the solution can also have effects on crystallisation[40–42].

Pseudopolymorphism comparatively is the ability of a compound to form a different structure as it incorporates solvent molecules into its structure as it crystallises. It is easy to imagine how this will change the unit cell and space group of the crystal as the packing changes with the addition of solvent molecules.

1.3 – Light

Light is an electromagnetic, transverse wave and so it has a polarisation perpendicular to the direction of motion[43]. This can be separated into two components also perpendicular to each other denoted as p and s. These refer to parallel and senkrecht, where senkrecht is German for opposed. These are usually defined relative to a reference point within the experiment. Any polarised light can be created by a combination of the s and p components, however to do this, the phase of the light must also be considered. The phase of light is the position through the sinusoidal wave that the light is at. The phase difference is therefore the difference of this between the s and p polarised light. A phase difference of 0° or 180° gives linearly polarised light, since the waveforms of the s and p light match up. If the intensities of the s and p light are equal and the phase difference is a quarter of a wavelength apart, at 90° or 270°, the light is circularly polarised. These are however special cases, most polarised light is some combination of s and p, and have a phase which is not a round number. This gives the ellipticity of the light, a combination of the intensity and phase difference of a light source.

1.3.1 – Anisotropy

Anisotropy is the property of a medium's response to be dependent on direction[44]. With regards to light, this is observed with materials which have different optical properties for s and p polarised light, such as refractive index or absorbance.

1.3.2 – Reflection and Refraction

Reflection of light occurs at the interface of two media with different refractive indices and results in the light reflecting back into the original medium. In the case of specular reflection, like that of a mirror, the angle of reflection is equal to the angle of incidence. Refraction occurs when the light is transmitted into the second medium[45]. As the light passes into the second medium, it changes speed, and thus the light bends according to Snell's Law, as shown in equation 1.13, where θ_i and θ_r

are the angle of incidence and refraction respectively, and n_1 and n_2 are the refractive indices of the initial and refracting media respectively.

$$\frac{\sin(\theta_i)}{\sin(\theta_r)} = \frac{n_2}{n_1} \quad \textbf{(1.13)}$$

1.3.3 – Fresnel Equations

The Fresnel equations describe the behaviour of light as it passes between two media, and the intensities of reflection and refraction seen, assuming that the interface is flat and the media are homogeneous[45]. The four Fresnel equations are shown below for the relative intensities of the p and s polarised components of for both the reflected and refracted beams.

$$\frac{E_{rp}}{E_{ip}} = r_p = \frac{n_1 cos\theta_i - n_0 cos\theta_t}{n_1 cos\theta_i + n_0 cos\theta_t} = \frac{\tan(\theta_i - \theta_t)}{\tan(\theta_i + \theta_t)} \quad \textbf{(1.14)}$$

$$\frac{E_{rs}}{E_{is}} = r_s = \frac{n_0 cos\theta_i - n_1 cos\theta_t}{n_0 cos\theta_i + n_1 cos\theta_t} = \frac{-\sin(\theta_i - \theta_t)}{\sin(\theta_i + \theta_t)} \quad \textbf{(1.15)}$$

$$\frac{E_{tp}}{E_{ip}} = t_p = \frac{2n_0 cos\theta_i}{n_1 cos\theta_i + n_0 cos\theta_t} = \frac{2sin\theta_t cos\theta_i}{\sin(\theta_i + \theta_t)\cos(\theta_i - \theta_t)} \quad \textbf{(1.16)}$$

$$\frac{E_{ts}}{E_{is}} = t_s = \frac{2n_0 cos\theta_i}{n_0 cos\theta_i + n_1 cos\theta_t} = \frac{2sin\theta_t cos\theta_i}{\sin(\theta_i + \theta_t)} \quad \textbf{(1.17)}$$

Where E_{ip} and E_{is} are the incident electric fields of the p and s polarisations respectively, E_{rp} and E_{rs} are the reflected electric fields of the p and s polarisations, E_{tp} and E_{ts} are the refracted electric fields of both polarisations, n_0 and n_1 are the refractive indices of each medium, θ_i is the angle of incidence, and θ_t is the angle of refraction. These equations calculate r_p, r_s, t_p and t_s, the quantity of p and s light reflected and refracted, compared to the intensity of the incident light.

1.3.4 – Complex Reflectance Ratio

The complex reflectance ratio shows the difference in the intensities of reflection of the s and p components of a beam of light[46]. This is used in this work in ellipsometry to show the effect a thin film has on the light. The complex reflectance ratio is shown below in equation 1.18, where ρ is the complex reflection ratio, r_p and r_s are the amplitudes of the p and s components after reflection respectively, normalised to their incident value, where the p is parallel to the plane of incidence. Ψ and Δ represent this ratio in the form of a complex number, with Ψ is representative of the intensity difference between r_p and r_s, and Δ is the phase difference between them.

$$\rho = \frac{r_p}{r_s} = \tan(\Psi)e^{i\Delta} \quad \textbf{(1.18)}$$

When dealing with the reflections of thin films as is commonly seen in ellipsometry, multiple reflections must be considered, as shown below in Figure *4*. The initial reflection off of the top of the film must be considered along with the subsequent reflection off the bottom of the film[47]. By using Drude's equations[48], multilayer models can be built which incorporate all of the reflections through a thin film.

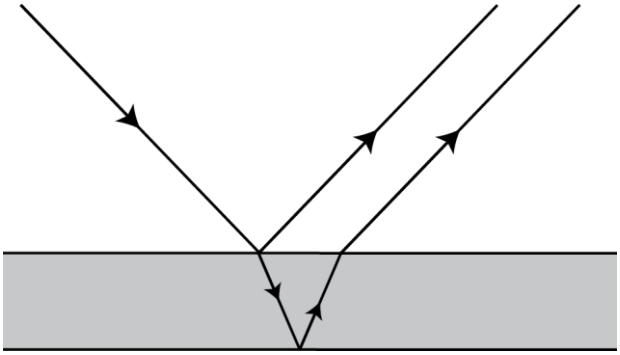

Figure 4 – Multiple reflections from a thin film.

1.3.5– Brewster Angle

The Brewster angle is the angle of incident light at an interface where no p polarised light is reflected where p is parallel to the plane of incidence[49,50].

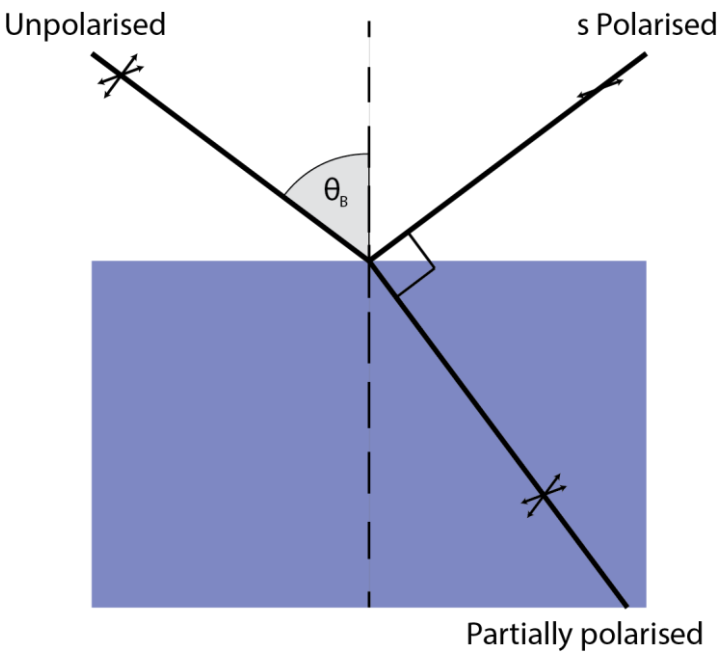

Figure 5 – Brewster angle illustration

This can be understood by looking at the mechanism of reflection. It can be imagined that upon reaching an interface light is absorbed and then immediately reradiated by the electric dipole of the medium. This dipole oscillates in the same direction as the polarisation of the light. This oscillating

dipole then generates the reflected light, however cannot generate a photon along this dipole. Therefore if the polarisation of light is exactly perpendicular to the angle of refraction then no light can be reflected. The angle at which this will occur for a given interface can be found stating the following:

$$\theta_B + \theta_R = 90° \tag{1.19}$$

Where θ_B is the Brewster angle and θ_R is the angle of refraction. Using Snell's law, it can also be shown that:

$$n_1 * \sin(\theta_B) = n_2 * \sin(\theta_R) \tag{1.20}$$

Where n_1 and n_2 are the refractive indices of the initial and subsequent media respectively. Substituting in the Brewster angle for the angle of refraction gives the following equation, 1.21, which can be solved to give an expression for the Brewster angle.

$$n_1 * \sin(\theta_B) = n_2 * \sin(90 - \theta_B) = n_2 * \cos(\theta_B) \tag{1.21}$$

$$\frac{\sin(\theta_B)}{\cos(\theta_B)} = \frac{n_2}{n_1} \tag{1.22}$$

$$\theta_B = \arctan\left(\frac{n_2}{n_1}\right) \tag{1.23}$$

The Brewster angle is therefore dependent on the refractive indices of the two media of the interface. Since air has a refractive index of 1, and water, 1.33, it can be calculated that the air/water interface has a Brewster angle of approximately 53°. Similarly, glass' refractive index of 1.5 gives a Brewster angle of around 56°. It is worth noting that since the refractive index of a material changes with wavelength, so does the Brewster angle.

It is worth noting that a nonzero value of the extinction coefficient (k) has an effect on the reflection at the Brewster angle. The absorption at the surface prevents the p-reflectance from reaching 0, resulting in real samples reflecting at lease a small amount of p polarised light at the Brewster angle even when they are effectively transparent.

1.3.6 – Stokes Parameters

The Stokes parameters are a matrix which characterises the polarisation of light which are used in ellipsometry[51]. It is made of four parameters which are summarised below. The first value represents the intensity of the light. This is typically represented as a value of one. The second and third values give linearly polarised light. Linearly polarised light at s and p polarisations give a second value of 1 and -1 respectively. Linear polarised light at 45° between s and p and s and –p also have values of 1

and -1 respectively. The final value of the Stokes parameters represents circularly polarised light, with a value of 1 for right hand polarised light, and -1 for left hand polarised light. Other polarisations of light can be constructed from combining these parameters.

The Stokes parameters can be calculated from the ellipticity of the light, using the parameters shown below, where I, p, Ψ and X are the spherical coordinates of the light.

$$S_0 = I \tag{1.24}$$

$$S_1 = I\,p\cos(2\psi)\cos(2\chi) \tag{1.25}$$

$$S_2 = I\,p\sin(2\psi)\cos(2\chi) \tag{1.26}$$

$$S_3 = I\,p\cos(2\chi) \tag{1.27}$$

1.3.7 – Second Harmonic Generation

Second harmonic generation (SHG) is a nonlinear optical process by which two photons of equal wavelength combine together to create a single photon of twice the energy[52,53]. It was first reported in 1961 by Franken et al. shortly after the invention of the laser[54]. They observed a faint spot at 347 nm after shining a 694 nm ruby laser beam through a quartz crystal. SHG has subsequently been studied and developed into a tool which has been used for various methods of analysis[55,56] and spectroscopy[57,58].

1.3.8 – Mechanism

SHG requires high intensity, polarised light in order to be observed. This is most easily achieved with the use of a mode locked laser. SHG is only seen in media which have a lack of a centre of inversion within their symmetry. A high degree of molecular order is also required to see a strong SHG signal, so crystals which lack a centre of symmetry in their unit cells are most commonly used. Both organic and inorganic crystals are used to generate SH signals, organic crystals have typically stronger susceptibilities, however have lower damage thresholds than commonly used inorganic crystals, such as β-barium borate (BBO)[59].

The second harmonic is generated as the light passes through the crystal. As the two photons pass through the unit cell, they are absorbed, oscillating the electric field of the crystal. This elevates it to a virtual energy level shown below in Figure *6*. The energy is then immediately reemitted as a single photon of twice the energy, and thus half the wavelength.

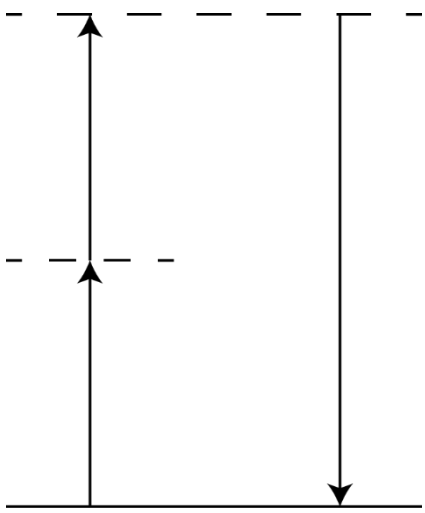

Figure 6 – Mechanism of SHG showing virtual energy levels

Nonlinear optical processes can be described as the following Taylor expansion[53].

$$P(t) = \epsilon_0(\chi^{(1)}E + \chi^{(2)}E^2 + \chi^{(3)}E^3 + \cdots) \quad \textbf{(1.28)}$$

Where P(t) is the polarisation density, ε_0 is the susceptibility of free space, $\chi^{(n)}$ is the nth order susceptibility coefficient and E is the electric field intensity. Each term in this equation represents the nth order processes which can occur. At low intensities of light, first order processes dominate, because $\chi^{(1)}$ is much larger than $\chi^{(2)}$ onwards. Since SHG is a second order process, it can be described as the second term in this equation.

$$P(t) = \epsilon_0\chi^{(2)}E^2 \quad \textbf{(1.29)}$$

From this it can be seen that the strength of the SH signal increases quadratically with respect to the intensity of the light source. It is also dependent on the second order susceptibility coefficient of the medium. This must be nonzero for SHG to occur. For nonlinear processes, the even order nonlinear susceptibilities are nonzero for media without a centre of inversion, while odd order nonlinear susceptibilities are nonzero in media with a centre of inversion[60]. The generation of the second harmonic can be found through the value of E^2, shown below.

$$E = E^0 \cos(\omega t)\, e \quad \textbf{(1.30)}$$

Where E^0 and e are the magnitude of E and a unit vector showing the direction of the light and cos(ωt) describes the frequency of the light. Substituting this definition into equation 1.29 gives the following expression for the second order term.

$$P_i(2\omega) = \varepsilon_0 \sum_{jk} x_{ijk}^{(2)} [\frac{E_j^0 E_k^0}{2}(1 + \cos(2\omega t))] \quad \textbf{(1.31)}$$

Where P_i is the magnitude of the polarisation induced in the electric field along j and k where i, j and k are perpendicular axes. It can be seen that this term produces a wave oscillating at twice the frequency to the original beam, at $2\omega t$.

1.3.9 – Phase Matching

Chromatic dispersion changes the phase velocity of light of differing wavelengths through a medium. This can become an issue with SHG, because as the light passes through the medium, the light and its second harmonic can get out of phase with one another, causing destructive interference for the second harmonic. As a result, the second harmonic is only seen at the small region at the interface where the destructive interference is not seen. Media which do not have this effect, and thus the light stays in phase can produce much stronger SH signals[60,61].

Chapter 2 – p-Nitrophenol Literature Review

p-Nitrophenol (PNP) is a simple aromatic compound which is widely used in the chemical industry as a precursor to many compounds, including paracetamol, as well as being used in the biological industry as a reagent in enzyme assays. It has been targeted as a compound to be used in non-linear optics to form new complexes with strong non-linear properties, and its surface activity has been studied through surface second harmonic generation. Due to its wide use in industry along with the potential health and environmental problems it can cause, much research has also been done into methods of adsorption and the catalytic breakdown of PNP. Additionally some of the stranger properties of PNP have also been noted, such as the photoreactivity under UV light of the α polymorph.

2.1 – Chemical Structure

Much of PNP's chemistry is dependent on the balance between its two forms in solution, phenol and phenolate. This position on this equilibrium is determined by the pH of the solution, with the phenol preferred at acidic pHs, and the phenolate at basic pHs.

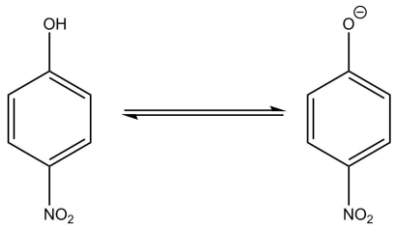

Figure 7 – Acid/base equilibrium for PNP

The phenol and phenolate each absorb light at different wavelengths. The phenol absorbs at 320 nm, while the phenolate has an absorption at 410 nm. This causes the neutral and basic solutions of PNP to have a yellow colour, while acidic solutions are clear since its only absorption is outside of the visible spectrum. The two spectra for acidic and basic solutions are shown in Figure *9*. In organic solvents, these absorptions are shifted due to the different chemical environment. In heptane for example, the phenol peak shifts downwards from 320 nm to 280 nm.

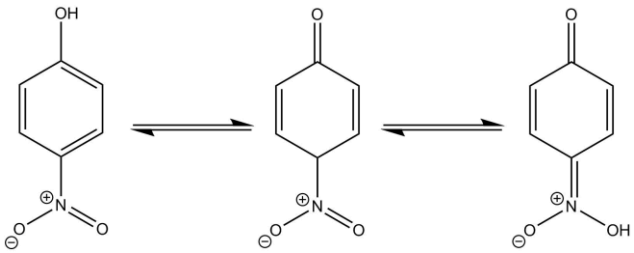

Figure 8 – Tautomeric forms of PNP

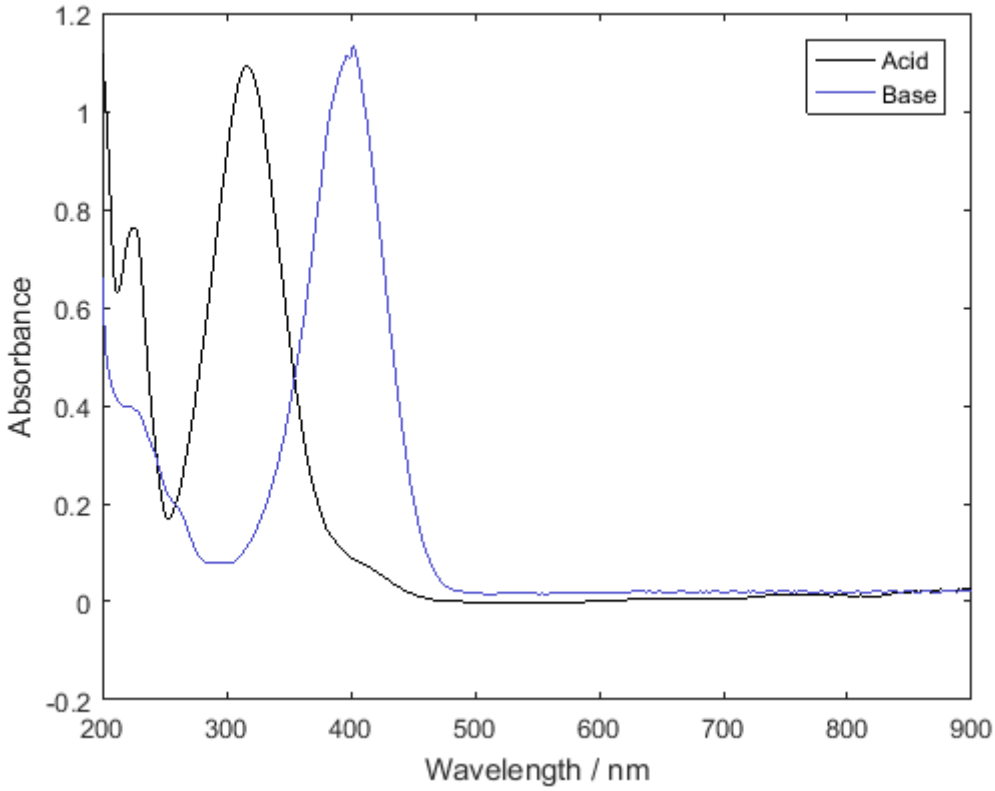

Figure 9 – UV/Vis spectrum two PNP solutions in acidic and basic conditions.

2.2 – Crystal Structure

PNP has two crystal structures, the alpha form crystallises from organic solvents such as diethyl ether[62], while the beta form is crystallised from water[63]. Some crystallographic information for the two polymorphs are shown below in Table 1. Under gentle heating the beta polymorph of PNP transforms into the alpha form.

Properties	**Alpha form**	**Beta form**
Space Group	P21/c	P21/n
a	11.660	15.403
b	8.78	11.117
c	6.098	3.785
Alpha	90°	90°
Beta	107.54°	107.06°
Gamma	90°	90°
CCDC Reference	NITPOL01	NITPOL02

Table 1 – Crystal properties of PNP polymorphs

PNP can also be crystallised as a salt when refluxed with a base, with sodium hydroxide giving the crystal sodium 4-nitrophenolate 4-nitrophenol dihydrate[64,65]. This complex was first noted by Hadzi et al. in 1962[64] during a study of the "Infrared spectra of, and hydrogen bonding in, some adducts of phenols and their phenoxides and other oxygen bases". In this study it was crystallised, along with the similar salt, potassium 4-nitrophenolate 4-nitrophenol dihydrate (made using KOH rather than NaOH) in order to study the difference between inter and intramolecular hydrogen bonds through IR spectroscopy. Various other PNP salts were also formed in this study, including salts with trimethylamine oxide and potassium acetate. The crystal structure of the sodium salt was first measured in 1994 by Minemoto et al.[66] Further studies of sodium 4-nitrophenolate 4-nitrophenol dihydrate have subsequently been performed in recent years in an attempt to create nonlinear optical (NLO) organic crystals by Selvakumar et al.[67]

PNP has often been targeted as a component in NLO materials. Due to its highly polarisable structure, it has great potential for materials attempting to achieve strong SH signal. It can be seen above in Table 1 however, that both of the polymorphs of PNP are centrosymmetric, so are unable to generate a second harmonic. Therefore, many studies have attempted to form complexes including PNP, to place it in a noncentrosymmetric unit cell where a strong nonlinearity could be observed.

The simplest solution to introduce noncentrosymmetry has already been discussed, converting 50% of the PNP into phenolate. This leads to a unit cell stoichiometry of 1 phenol : 1 phenolate : 2 waters, and breaks the centrosymmetry. Another similar complex was studied by John et al.[68] wherein the water molecules and sodium ion were replaced with dimethyl amino pyridinium ion, giving a complex of dimethyl amino pyridinium 4-nitrophenolate 4-nitrophenol. Both of these complexes have a high nonlinearity, giving an order of magnitude greater SHG signal than potassium dihydrogen phosphate, an NLO reference material.

2.3 – Uses

PNP is a widely used reagent in the chemical industry. PNP is reduced to 4-aminophenol and then acetylated with acetic anhydride to make paracetamol. The largest use of PNP in industry is the manufacture of fungicides, pesticides and dyes, while PNP itself has been used as a fungicide. Two such examples are shown in Figure *10*, 4-phenetidine, a dye and parathion ethyl, an insecticide.

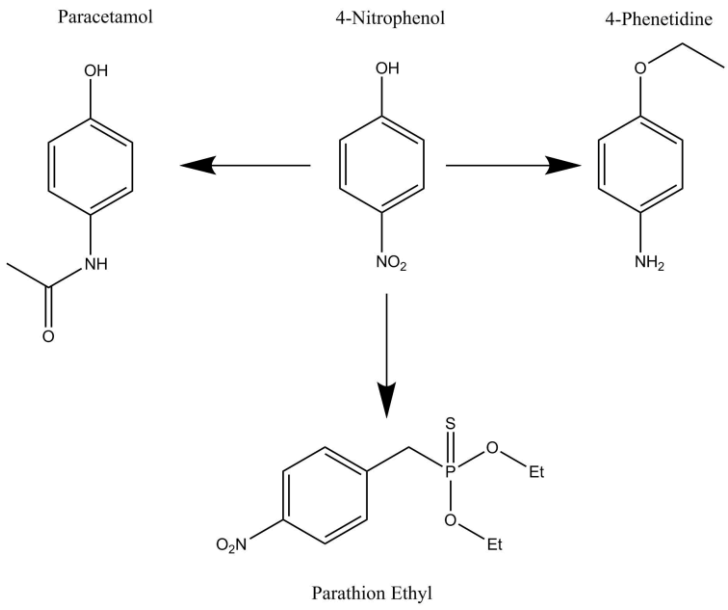

Figure 10 – PNP and three of its derivatives.

The changing absorbances of the phenol and phenolate also allow PNP to be used as an indicator. Above neutral pHs, PNP solutions gain a yellow colour due to the presence of phenolate. p-Nitrophenylphosphate is frequently used in biology for enzyme assays. Liberation of the phosphate by the active enzyme leaves the phenolate in solution, giving a distinctive yellow colour.

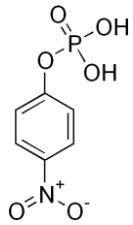

Figure 11 –p-Nitrophenylphosphate

2.4 – Surface Second Harmonic Generation

PNP was first noted for its SSHG abilities in 1987 by Bhattacharyya et al.[69]. In this study they watched the progress of a chemical reaction by the SSH signal generated by PNP. The reaction in question was the equilibrium between phenol and phenolate, shown above in Figure 7, as the pH changed. At this point, SSHG was a new, developing technique, only a couple of years old[70–73], so this simple reaction was studied to see the sensitivity at the surface to changes in the bulk. The SSH signal was measured from pH 2 to 13, as the equilibrium shifted from the protonated phenol, to the unprotonated phenolate. The strongest SSH signals were seen for pH 4 and below, approximately 80 times the value of that of water. At strongly alkaline pHs, the signal decreased to that of water, suggesting that the phenolate is not surface active, only the phenol. They estimate that the ratio of phenolate to phenol at the interface to be around 1:50-100 molecules. They also note the apparent

difference in concentrations at the interface in the bulk around neutral pHs. PNP has a pKa of 7.15, so the neutral point for the phenol/phenolate equilibrium exists at pH 7.15, indicating that 50% of the PNP in solution would be in the phenol form. This differs to the SSH signal, where the point of 50% SSH signal from the maximum, indicating 50% of the possible phenol concentration, is at pH 7.9, suggesting that the neutral phenol form is at a greater concentration at the surface than would otherwise be expected.

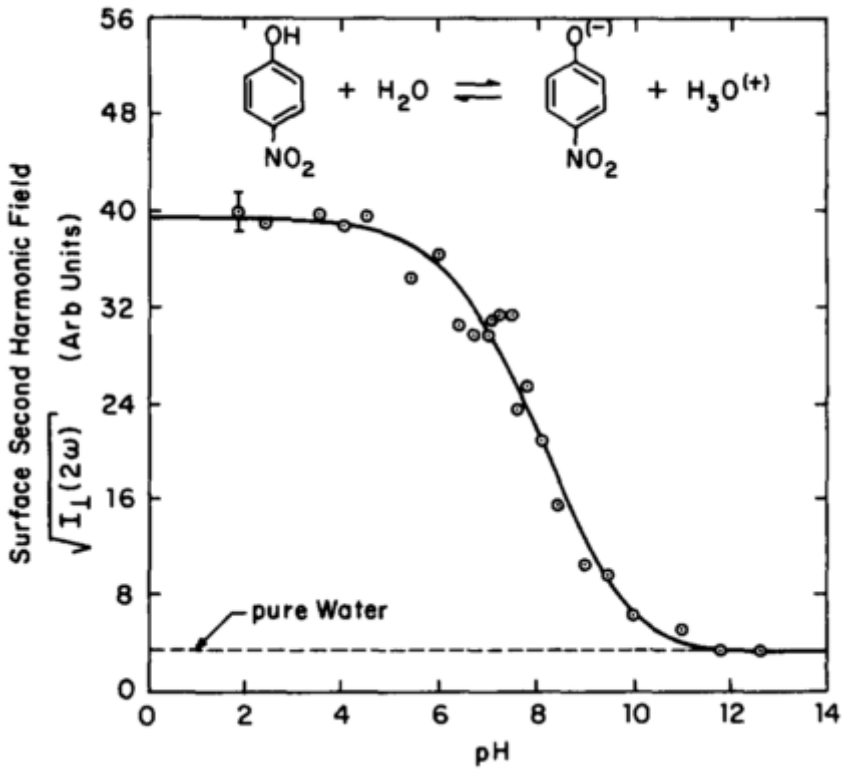

Figure 12 – Second Harmonic Intensity vs PNP solution pH. Reproduced from citation[69].

The next year, the same group published a second study of the SSH properties of a liquid jet[74]. This study focussed on the SSH signal from solutions of PNP as they flowed in a jet. The measurement of the SSH signal from the jet was measured as a function of time, and it was found that the signal increased over the first 25 ms, with the signal also increasing for higher concentrations of PNP. The time was measured by moving the spot further from the nozzle used to generate the jet, with the time being calculated using the flow speed of the solution, and the distance from the nozzle. This signal was fitted to a time dependent Langmuir model, where the rate of growth is limited by the number of free sites available to adsorb, giving a rate constant of adsorption of 4.4×10^4 s^{-1} and a rate constant of desorption of 6 s^{-1}. This indicates that the PNP is stable at the surface, and is comparatively unlikely to desorb into the bulk after it reaches the surface. This is due to the

hydrophobic aromatic ring which prefers the surface environment. It is also helped by the hydrophilic hydroxyl group which points downwards into the bulk[75].

Further measurements of the SSH signal of PNP at the glass/water interface gave a lower signal than the air/water interface. The strength of this signal also obeyed a Langmuir model with respect to concentration. This lower signal is caused by the more hydrophilic surface of glass, giving the PNP at the glass/water interface less hydrophobic stabilisation, and thus a lower PNP surface concentration. The SSH signal obtained for the concentration of PNP at the glass/water interface was found to be the starting values of the measurements of the jet detailed above, indicating that the SSH signal increase measured from the jet is representing the surface concentration of PNP increasing from the value for the glass/water interface to that of the air/water interface. The enthalpy of adsorption at the interface was calculated as -5.1 kcal/mol and -3.4 kcal/mol for the air/water and glass/water interfaces respectively.

Further work was also done on the effects of different compounds on PNP at the air/water interface. Work by Bhattacharyya's group in the mid-nineties looked at the effect of first urea and a surfactant[76], and then guanidinium chloride, lithium perchlorate and lithium chloride[77]. All of these compounds are SSH inactive. The addition of urea to an aqueous PNP solution was found the drastically reduce the SSH signal, with the urea molecules acting to stabilise the PNP in solution, a bridge between the hydrophobic PNP and water. This results in a lower concentration of PNP at the interface. The chosen surfactant, cetyltrimethylammonium bromide (CTAB) has the opposite effect. Low concentrations of CTAB cause a 10 fold increase in the SSH signal. The presence of surfactant has the opposite effect to that of urea, acting at the surface to stabilise PNP molecules, and so increasing the concentration at the interface.

Addition of $LiClO_4$ and GdmCl cause a decrease in the SSH signal, similarly to urea, however it was found that the addition of LiCl cased an increase in the signal, with 5 M LiCl approximately doubling the signal strength of a 25 mM PNP solution. Rather than the signal increase seen for CTAB, where the PNP was stabilised at the surface, addition of LiCl caused the PNP to have reduced stability in aqueous solution so subsequently a higher surface concentration was seen.

Similarly to above, the effect of penta- and hexadecanoic acids on the PNP SSH signal[78] were studied. These fatty acids were again chosen because they do not generate a SSH signal however are surface active and have distinct surface pressure curves upon compression. As the surface concentration of both acids increases, the SSH signal from PNP increases gradually, then sharply drops near the maximum acid concentration. Curiously however the results for the two experiments have extremely similar SSH signals, yet very different surface pressure data. This was due to the different

parts of the monolayer being probed by each technique. The compression measurement was sensitive to the interactions between the hydrophobic fatty acid tails as they were compressed into a smaller area. The PNP however seems to instead be located with the acidic head groups of the acid, at the water surface. Because of this, the SSH signal was insensitive to the changes in the tail groups upon compression, and so no difference is seen between penta- and hexadecanoic acid.

PNP's SSH activity was applied to the study of tri-n-butyl phosphate (TBP) at the water/dodecane interface[79]. TBP is used as a complexing agent to separate metals in aqueous solutions into the organic phase and surface tension measurements indicate that TBP is present at the water/dodecane interface[80]. The SSH signal from PNP was collected at varying concentration of PNP in water, and TBP in dodecane, and so their interaction at the interface was measured. At low concentrations of PNP, an increasing concentration of TBP caused higher SSH signal. High concentrations of TBP however caused a large drop in the SSH signal. This is attributed to complexation between the PNP and TBP, breaking the weak orientational order of the PNP which is required for SSHG.

2.5 – Surface Activity

In addition to the SSHG work detailed above, PNP's surface activity was studied by Paluch and Filek in 1980[9]. This work details the effect of para substituted phenols on the surface tension of water with concentration. Of the p-phenols tested, PNP had the smallest change in surface tension, to approximately 60 mN/m at the maximum concentration, 100 mM. The data was fitted to a Volmer isotherm and the free energy, enthalpy and entropy of adsorption were calculated as -2.51, -2.00 and 1.74 kcal/mol at 303 K.

2.6 – Thermal Instability

The β polymorph of PNP, grown from water is thermally unstable[81]. Coppens and Schmidt note the fact in their original paper detailing the crystallographic information of the polymorph[63], that under gentle heating, the crystal undergoes a phase transition to the α form. This was investigated further by Wojcik et al.[82] by single crystal X ray diffraction and differential scanning calorimetry (DSC). They found that during hot stage microscopy, the heating required to convert the β polymorph to the α was variable, from 331 K to 366 K. This was attributed to varying crystal quality. This carried over to DSC, where the curves had the same general endothermic peak around this temperature, but were otherwise inconsistent.

They performed SCXRD experiments over the temperature range 233 K – 393 K for both polymorphs of PNP. They measured the thermal expansion from heating and related this to the molecular

libration and vibration of PNP. The α polymorph shows a greater libration while torsional vibrations in the nitro group are dampened compared to the β polymorph. This leads to the transformation from β to α upon heating whereby the crystal expands and as the nitro groups move into a more energetically favourable position, the transformation becomes permanent, so it does not revert upon cooling.

2.7 – Photostability

In 1859, Fritsche[83] undertook a study "of the action of the products of the action of nitric acid on phenol". This reaction produces a mixture of 2-nitrophenol and 4-nitrophenol. These two compounds were separated and crystallised and, amongst other discoveries, it was found that the PNP crystals slowly turned pinkish/red over time when exposed to light. It was later found that only the α polymorph, grown from organic solvents such as diethyl ether undergo this change, and only when exposed to UV light[62].

The mechanism of this photochemical colour change has been of interest ever since. In 1998 and 1999 Kulkarni et al. published two studies regarding charge density studies of PNP[84,85]. Charge density studies are high resolution single crystal X ray diffraction experiments which, while being very time intensive to collect, give excellent detail on the location of charges through the unit cell. The 1998 paper saw charge density studies of both the α and β polymorphs, while the 1999 paper saw the same technique applied to a UV irradiated crystal of the α polymorph. In the first study the differences in the intramolecular features of the two polymorphs are noted. In the β form of PNP, the only atom which has a significant displacement from the plane of the benzene ring is one of the oxygens attached to the nitro group (0.22 Å from the plane), while in the α modification the hydrogen atom of the OH group has a larger displacement (0.32 Å), while the nitro group is effectively planar. The C-C-O bond angles within the two polymorphs also differ, 5.5° in the α form, and 6.24° in the β form. This is in agreement with the papers published previously by Coppens and Schmidt[62,63].

They also note several intermolecular differences between the two polymorphs. Firstly, the angle between the nonparallel PNP molecules differs between the polymorphs, 74.73° for the α form, and 29.26° for the β form. Additionally, the α polymorph has a larger number of hydrogen bonds than the β, 9 compared to 6. Further analysis of the hydrogen bonds shows that the strongest H bond is present in both polymorphs, between the nitro group and the hydroxyl group of adjacent PNP molecules, however the nature of the bonds are different. In the β form, the hydrogen bonding occurs between one oxygen of the nitro group, and the hydroxyl hydrogen, while the other nitro

oxygen hydrogen bonds to a phenyl hydrogen. In the α form however, the hydroxyl hydrogen is closer to the nitro group and so the whole nitro group is involved in the hydrogen bonding.

Finally they note a few differences in the density of charges on atoms between the two polymorphs. The β form shows a higher density of negative charges around the benzene ring, and in the C-N and C-O bonds, while the α polymorph displays a higher charge density within the hydroxyl and nitro groups.

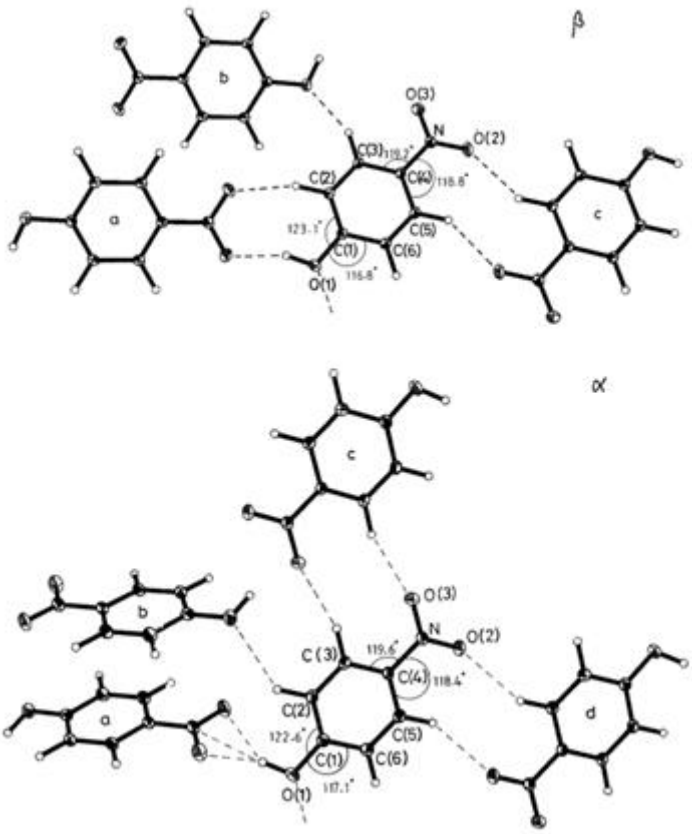

Figure 13 – Intermolecular bonding of PNP polymorphs, β polymorph top, α polymorph bottom. Reproduced from citation[86].

The 1999 paper discusses the results of the charge density study of the irradiated form of α PNP and then compares it to the previous results. These comparisons found that the structure was very similar to that of before irradiation, but the intramolecular charge density resembles the β form more closely, with a transfer of charge from the nitro and hydroxyl groups onto the benzene ring. The unit cell of the irradiated form appeared the same as that of the α form, though the angle between the nonparallel PNP molecules changed subtly from 74.73° in the α form, to 74.58°. The hydrogen bonding network appeared unchanged between the α and irradiated forms, though there are small displacements in the positions of the nitro and hydroxyl groups. Charge density analysis shows that the bonding in the benzene ring of the irradiated form retained its aromaticity and while

there are many small changes between the structures, they are largely marginal. The most notable change regards the density along the hydroxyl bond, which is lower, and closer to the oxygen in the irradiated form, resembling the β form more closely.

Antherton et al. also performed a SCXRD study of irradiated PNP in 1990[87] and was referenced in the previous papers. They found significantly different results, however this can most likely be explained by their source of irradiation. Their results show the formation of a cyclopentadienyl radical, a much greater structural change that what was subsequently seen by Kulkarni. Rather than the gentle irradiation by sunlight which was used in other studies, this work performed irradiation with a ^{60}Co γ source. This is likely the cause of the more extreme changes seen in this work, and while a similar colour change was reported, it is unlikely that this is the same mechanism which was noted by Fritsche and Kulkarni.

From the above studies, it is logical to deduce that the colour change seen during the photochemical reaction of α PNP is related to the hydroxyl hydrogen shifting towards the nitro group. The subtle changes which were observed do not however fully explain this colour change. Such a small shift should not have such a large effect, so this is far from conclusive. It may be useful to compare this reaction to a similar intramolecular reaction which is seen for an isomer of PNP, 2-nitrophenol (ONP).

The photolysis of ONP has been studied as a potential atmospheric source of nitrous acid (HONO)[88–90]. Figure *14* shows the proposed intramolecular reorganisation that allows the photolysis of HONO, and it is easy to see a comparison to the intermolecular H transfer proposed as a mechanism for the colour change seen in PNP.

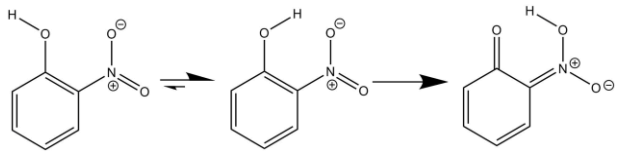

Figure 14 – ONP rearrangement leading to HONO photolysis.

This mechanism is obviously not highly favoured under ordinary conditions, due to the breaking of aromaticity of the benzene ring, but Bejan et al.[88] showed that irradiation of ONP in the gas phase generated HONO, with a linear relationship between the concentration of ONP and HONO.

Grygoryeva et al[90] make comparisons between the clustering of ONP, PNP and phenol using velocity map imaging (VMI), mass spectrometry and computational modelling. In the VMI experiments, the O-H bonds were photodissociated and the kinetic energy of the resulting H^+ ion was measured using VMI. The subsequently formed clusters were then positively ionised and measured using mass

spectrometry. These values were then compared to those calculated for dimers and trimers of the respective compound. It was found that for dimers of ONP and PNP, pi stacking led to a more stable configuration than H bonding, however for PNP, the addition of a third molecule greatly increased the stability of the H bonding system over that of the pi stacking system. This was not true for ONP.

Overall, it is likely that an H transfer mechanism is responsible for PNP's colour change on irradiation, however the evidence is not yet conclusive. The main difference between the α and β polymorphs of PNP is their H bonding, so this is likely to be the cause of the α polymorph's photosensitivity. The charge density studies show that the change caused by the irradiation is very subtle with regards to the electronic structure, with the largest observable difference being the charge density along the hydroxyl bond shifting closer to the oxygen, suggesting a change in the position of the hydrogen.

2.8 – Pollutant Studies

Due to the large scale usage of PNP in the chemical industry as well as its use in agricultural fields, much work has been done on understanding the environmental effects of PNP, and many methods have been developed to remove it from the environment. A complete review of these methods and their merits is beyond the scope of this review, so a selection have been chosen to look at the many avenues of research which have, and in many cases still are being undertaken.

The source of PNP in the environment has been studied extensively. It has been noted as a product of the breakdown of the insecticide parathion[91] shown earlier in Figure *10*. Additionally, nitrophenols have been found in the atmosphere from car exhaust fumes[92]. As well as identifying the sources of PNP in the environment, many different, novel methods for its removal and breakdown have been studied. Photochemical breakdown of PNP has been achieved by multiple methods, Chen et al. report degradation of PNP using a TiO_2 suspension[93], while Zhang et al. instead have used a different UV/H_2O_2 mechanism to oxidise the PNP[94]. Further studies have used techniques such as sonolysis[95] (high powered ultrasonic vibration), and electrochemical methods to breakdown PNP fully[96]. In their reviews of different methods of adsorbance for pollutants, Bhatnagar and Minocha report several methods which have been studied for PNP[97,98], including activated carbon, from different environmentally friendly sources and fly ash. This is a small section of the work which has been done to understand the sources and effects of PNP in the environment, and the work being done to capture and remove it safely.

Chapter 3 – Experimental Techniques

3.1 – Second Harmonic Imaging Microscopy

3.1.1 – Laser

The laser used in this experiment was a wavelength tuneable 2 W Ti:Sapphire laser with 140 fs pulse, 76 MHz repetition rate and a wavelength range of 700-900 nm. This was powered by a VERDI, 10 W 532 nm seed laser. The output light from the laser was vertically polarised in a 1 mm radius spot.

3.1.2 – Optical Path

The optical path is shown below in Figure *15* and Figure *16*. Figure *15* shows the signal path from the output of the laser through to the microscope, while Figure *16* shows the interior of the microscope and the path to the detector. The intensity of the laser was controlled using a Fresnel rhomb and linear polariser. The polariser was set to transmit horizontally polarised light, in order to achieve complete reflection from the dichroic mirror, and the Fresnel rhomb could be rotated to change the polarisation of the beam, and thus the transmission through the polariser. This was important for working with various organic crystals which could be damaged by too high intensities of light, additionally it was useful to decrease the intensity of the signal on the detector when it was too strong.

The beam size could be altered by changing the length of the telescope. This was done to minimise the spot size in the microscope objective to get maximum intensity.

Alignment was performed using the two first mirrors and the irises labelled 6 and 9 on Figure *15* to ensure the beam was straight through the telescope. The alignment of the beam into the microscope was checked using the camera image of the sample. The beam must be located centrally on the camera image, and as the focus of the microscope changed, the spot should stay in the same space, indicating that the beam was moving straight.

Inside the microscope, a dichroic mirror was used to separate the SH signal from the incident 800 nm light. Dichroic mirrors are reflective at certain wavelengths and transmissive to others, in this case reflective to 800 nm and transmissive to 400 nm. The dichroic operated most effectively with vertically polarised light, so the earlier beam path was engineered to deliver that polarisation. The laser outputted vertically polarised light, however the periscope rotated this by 90° due to the change in direction. Therefore the polariser used for controlling the intensity was set to transmit

horizontally polarised light, and the rhomb was used to rotate the light so as the light was rotated in the periscope it returned to vertical polarisation.

The light then passed through the sample, off a mirror and through the sample again, in the same place. The SH signal is then transmitted through the dichroic, while the 800 nm light is reflected back down the experiment where it is absorbed by the faraday isolator. The light then passes through a 400 nm filter, which absorbs any 800 nm light which passes through the dichroic. The light is then split to either the camera or the detector.

A pinhole and another 400 nm filter were placed in the path to the detector to eliminate any light reaching the detector which was not the SH generated in the sample. An ND filter was also used to decrease the intensity of the light on the detector where necessary.

3.1.3 – Detection

A fW detector was used to collect the signal from the experiment. The detector output a voltage from 0-7 V DC signal depending on the signal intensity on the detector. A C mount Dinolite camera was also used to image the experiment.

3.1.4 – Piezoelectric Stage

In certain experiments, a Nanonics piezoelectric stage was used to move the sample to allow imaging. This stage had a range of 100 µm and was typically used to image a 40 µm square with 1 µm resolution.

3.1.5 – Data Acquisition

The detector connects to a lock in amplifier which amplifies the signal as well as removing noise by way of a chopper. The output is a DC signal between 0 and 10 V. The chopper is a rotating blade at the start of the laser path. As the chopper rotates, it blocks the beam and transmits it at regular intervals. The chopper also outputs a signal of the same frequency which is sent to the lock in amplifier. Since all laser light is blocked when the chopper is in the way, any other signal must not be the SH signal, and must therefore be unwanted noise. Therefore by Fourier transforming the signal at the frequency of the chopper blade rotation over several cycles, any signal which is not passing through the chopper, and thus the desired laser signal is removed. The lock in amplifier then sends a DC signal between 0-10 V to either a National Instruments DAQPAD 6020e or the Nanonics signal acquisition box. Both of these convert the signal from analogue to digital and send it to a computer where the data is saved. The Nanonics system was used in tandem with the piezoelectric motor, while the DAQPAD was used when the sample was not being moved, over longer experiments. The

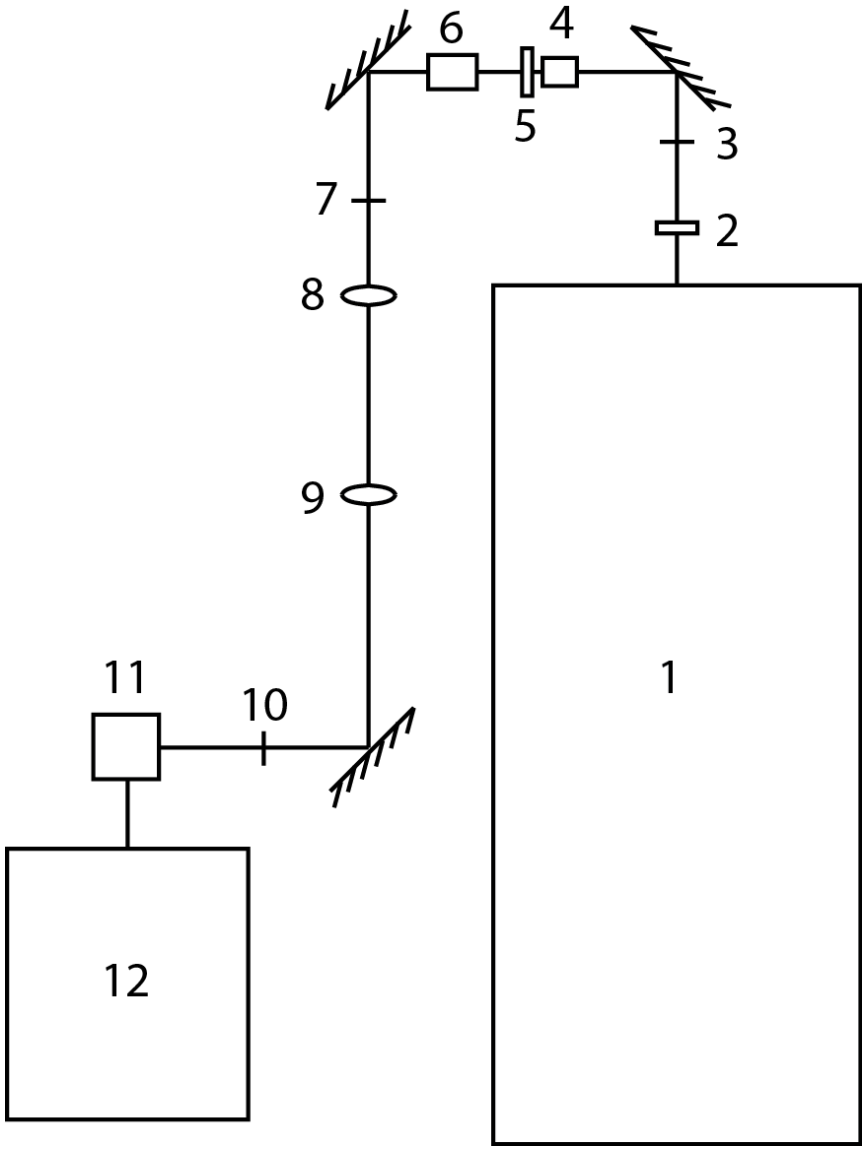

Figure 15 – Laser table schematic – 1, laser, 2, interlock, 3, chopper, 4, Fresnel rhomb, 5, linear polariser, 6, faraday isolator, 7, iris, 8, front telescope lens, 9, rear telescope lens, 10, iris, 11, periscope, 12, microscope

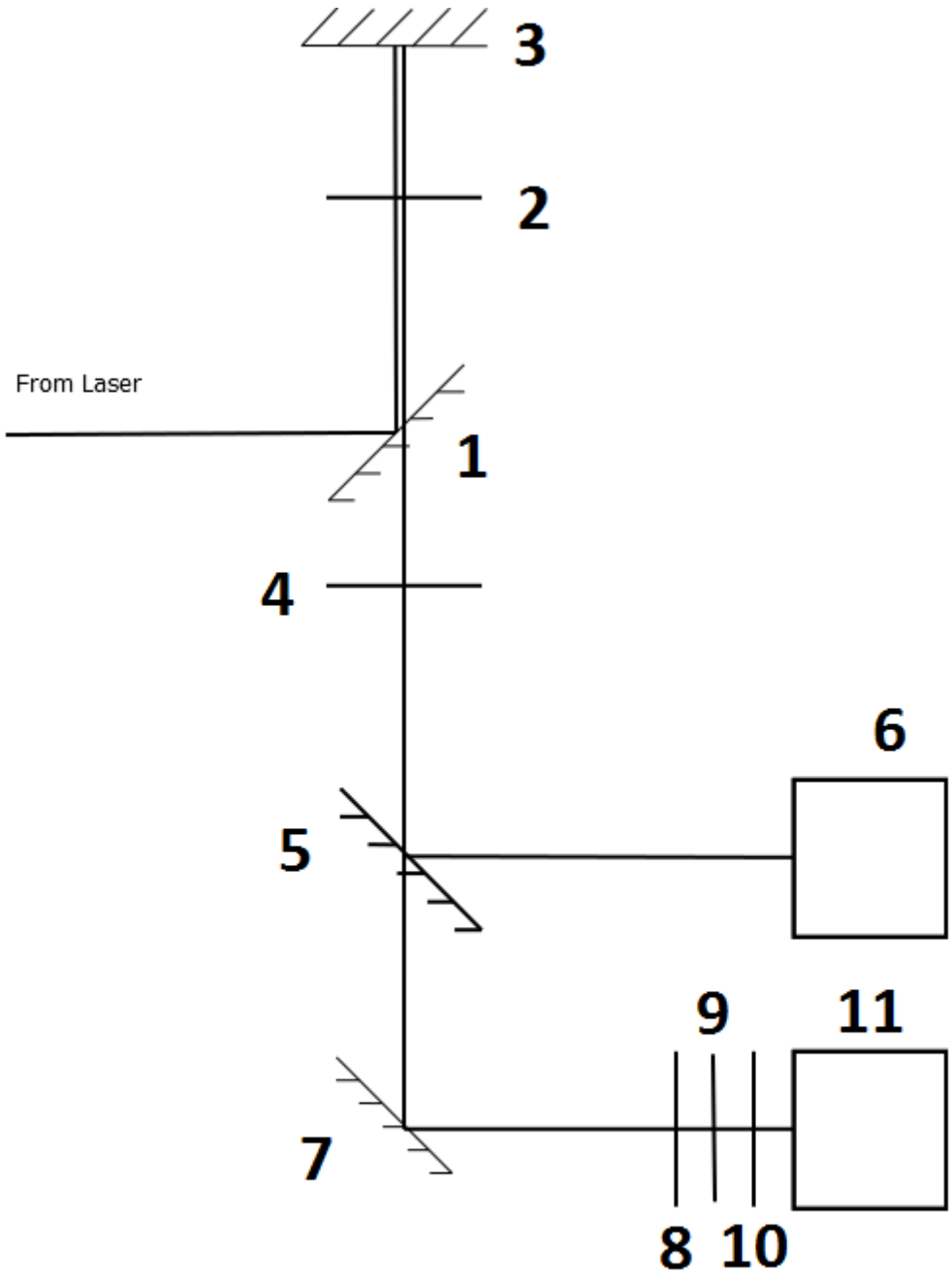

Figure 16 – Microscope schematic representing object 12 in Figure 15, where 1, dichroic mirror, 2, sample, 3, mirror with backlight, 4, 400 nm filter, 5, rotatable optic for either 100% of light to camera, 100% of light to detector or 50/50 split, 6, optical camera, 7, mirror, 8, optional ND filter, 9, 400 nm filter, 10, pinhole, 11, fW detector.

Nanonics software was used to generate an image of the mapped area, and the DAQPAD signal was processed in MATLAB as follows.

Within MATLAB, the legacy data acquisition toolbox was used to trigger and collect the data from the DAQPAD. The DAQPAD was capable of collecting very accurate data at very high speeds, up to thousands of points per second, however had a time lag between triggering an acquisition and its response of approximately 1.7 s. Therefore when the DAQPAD was used for data collection, it was preferable to collect a single acquisition with many points rather than many short triggers. When multiple triggers were used, it was important to collect the time of the trigger so that they could be accurately attached together with respect to time after the experiment was finished.

3.1.6 – Noise Removal

There were two sources of unwanted signal in this experiment, first is any remaining 800 nm light which had not been reflected or absorbed, or from any other light sources in the room, such as the ceiling lights or the microscope backlight. In order to test that only the SH signal was reaching the detector, the laser power was varied, and the SH signal through a BBO crystal was measured. This relationship is shown in Figure *17* and shows that the signal output by the lock in is quadratic with respect to the laser power and therefore only consists of the SH signal

An experimental example is also shown in Figure *18*. It can be seen that outside of the region of the image where the crystal is located, no signal can be seen in the amplitude. The noise level in this region is approximately 0.01- 0.02 V, which is negligible compared to the sample's signal. The lock in phase is also shown for this image. In it, anywhere that the SH signal is recorded, the phase is constant since this matches up with the frequency of the chopper. Outside of this area, the phase is random noise since the random is not of the same frequency as the chopper.

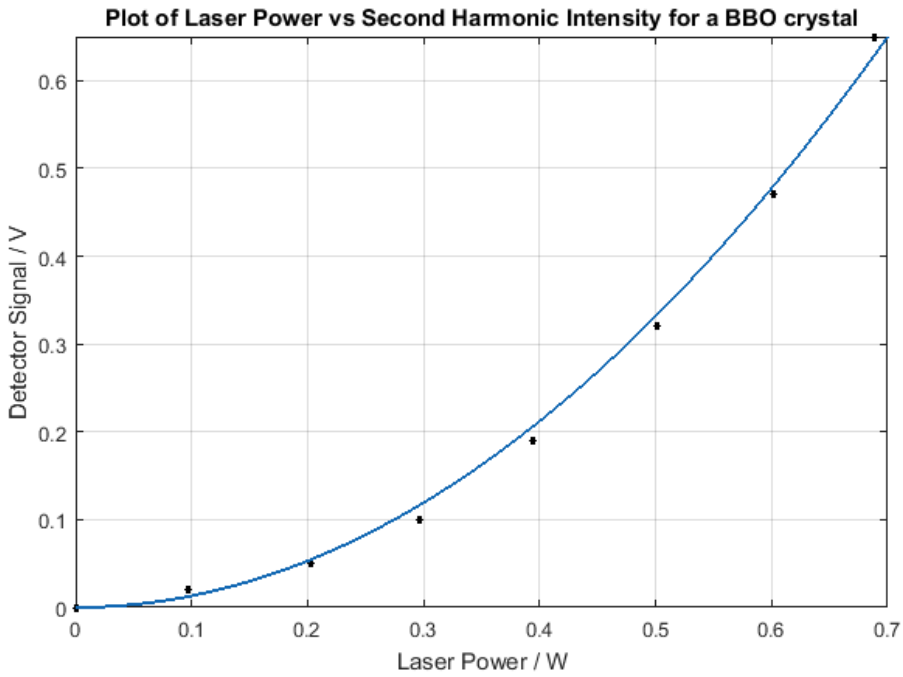

Figure 17 – Quadratic relationship between laser power and SH signal

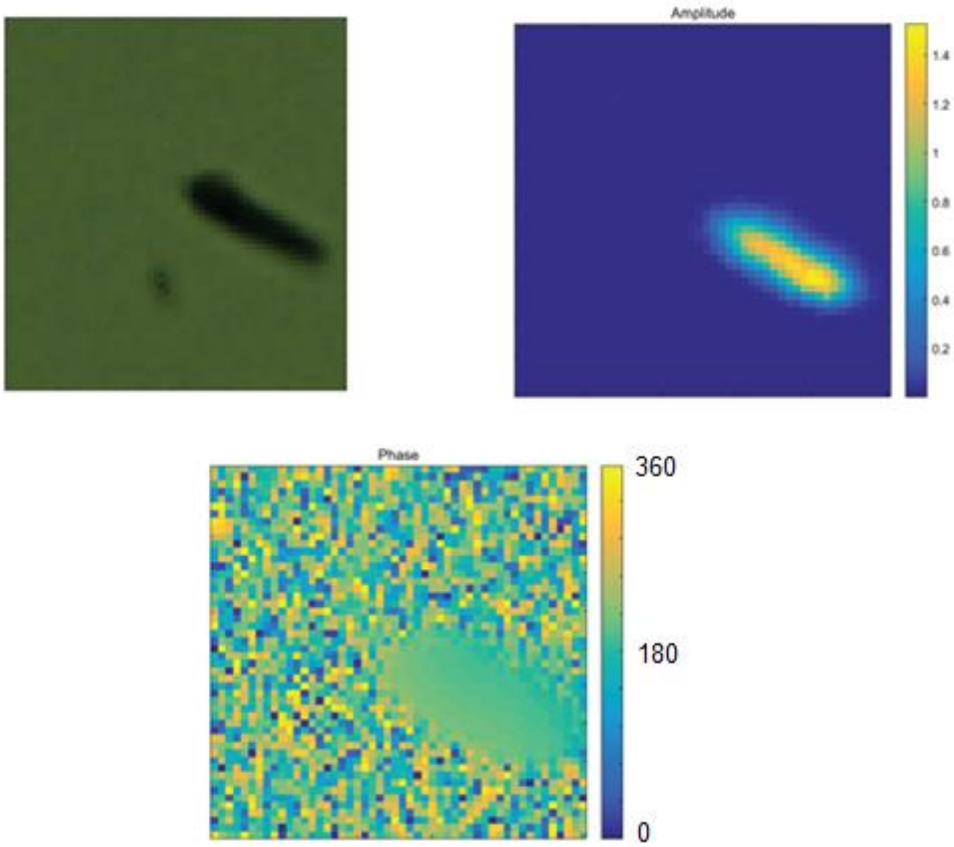

Figure 18 – 40 µm images of Methylbenzylaminonitropyridine (MBANP) Melt on glass slide. Top left, Camera image; top right, amplitude; bottom, phase. See Chapter 5 for further details

3.2 – Langmuir Blodgettry

Langmuir Blodgett (LB) troughs measure surface pressure. LB troughs operate by measuring the capillary force pulling down on a Wilhelmy plate by the liquid surface. This force is caused by the surface tension; the larger the surface tension, the stronger the capillary force felt by the plate. This force is measured by an electrobalance which sends the reading to a computer. This computer also controls the barrier movement. The surface can be compressed or expanded by moving this barrier backwards and forwards. The troughs themselves, as well as the barriers were all made from polyfluorotetraethylene (PTFE) to ensure that they had minimal chemical interaction with the solution being studied. LB troughs typically also have dipping mechanisms used to deposit monolayers on surfaces, however this technique was not used in this project.

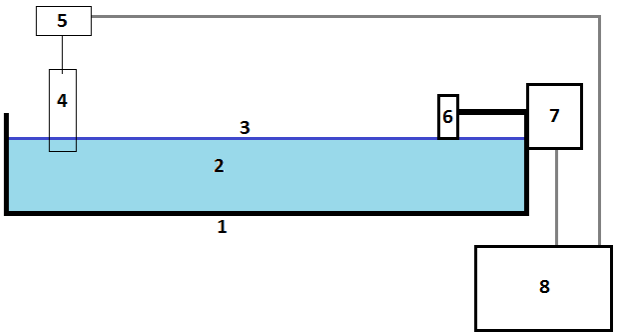

Figure 19 – LB Trough schematic: 1 - LB trough, 2 - liquid subphase, 3 - monolayer, 4 - Wilhelmy plate, 5 - Electrobalance, 6 - Barrier, 7 - Barrier Controller, 8 - Computer.

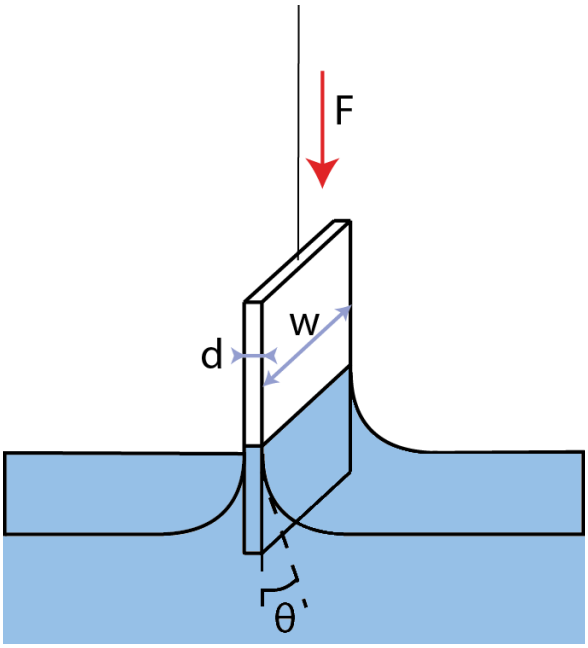

Figure 20 – Representation of a Wilhelmy Plate.

Langmuir Blodgett troughs determine the surface pressure change by the change of force on the electrobalance using the following equation.

$$\gamma = \frac{F}{l\cos(\theta)} \quad \textbf{(3.1)}$$

Where γ is the surface tension, F is the capillary force on the plate, l is the wetted length and θ is the contact angle. The contact angle is assumed to be 0 since infinite wetting is assumed. L is calculated as the length of the contact between the plate and liquid, so is the sum of twice the thickness and width of the plate (l = 2d + 2w). The surface pressure can therefore be determined from the relative change in force on the balance.

3.2.1 – Wilhelmy Plates

Wilhelmy plates were prepared by the following method. 1.5 cm long strips of filter paper were cut from a roll 8 mm in width, as squarely as possible. These plates had a small hole poked through in the centre of the 8 mm side, close to the end. The plates were then soaked in chloroform for 30 minutes to remove any organic contamination. They were then removed from the chloroform and left to dry for two minutes, making sure that the plates stayed clean. Finally the plates were left to soak overnight in the solvent to be used in the experiment. Deionised water was used as the solvent for all experiments in this project. This was done to ensure that the mass of the plate did not change during the experiment. If the plates were dry when used, the solvent would wick up the plate during the experiment. As the mass of the plate increased from the water, it would cause a greater downward force, causing an apparent increase in surface pressure which would not be real. This is avoided by pre-soaking the plates before use.

It should be noted that it is also possible for the PNP dissolved in the water to wick up the Wilhelmy plate through the course of the experiment. However at the concentrations which experiments were conducted in this work, and considering the length of time the experiments were run for, this did not have a noticeable impact on the data collected.

3.2.2 – Langmuir Blodgett Experimental

Langmuir Blodgett experiments were performed in two different troughs in this work. For most experiments, a small trough, of volume approximately 10 cm^3 was used. One set of experiments was performed using a larger, 1.3 L NIMA trough. All the experiments in both troughs made use of the pressure sensor from the NIMA trough system. These experiments were performed in a temperature controlled laboratory held at 22°C.

Experiments in the small trough were performed as follows. Firstly, the trough was cleaned, if this had not already been done. To do this, the trough was repeatedly filled with water until the yellow colour from the PNP could not be seen in the solution. Acetone was then used to moisten lintless paper and this was used to wipe down the inside of the trough. Finally, the same was done with lintless paper moistened with isopropyl alcohol. The trough was then left to dry before it was used.

To set up the experiment, the Wilhelmy plate was suspended from the electrobalance above the expected height of the solution. The solution was then prepared by either sonicating or vigorous stirring and added to the trough quickly and the plate was lowered into the solution. The cover was placed over the top of the trough, and then the surface pressure value was zeroed. Readings were then started to take the surface pressure every 0.1 s until the command was given to stop recording.

Experiments in the NIMA trough were performed in a similar manner, however used a much larger volume. The cleaning was performed in the same manner as the small trough and the plate was suspended. The 1.3 L solution was prepared in advance, and then stirred as vigorously as possible. The solution was carefully added to the trough and the plate was lowered into the solution. As with the small trough, the cover was lowered over the trough, and the surface pressure was then zeroed. At this point, the method deviates further from that of the small trough. The pre-programming capability of the software was used to set up experiments. The barrier was controllable by the computer, so during the course of the experiment, the trough was set to compress and expand at set speeds, designated in cm^2/s, and to wait at a specific surface area. Elasticity measurements were also performed by compressing and expanding around a specific surface pressure. This will be discussed in more depth later.

3.2.3 – Experimental Sensitivity to Environment

The experimental setup was found to be very sensitive to a variety of environmental factors. The experiment was adjusted in the following manner to account for these issues. The Wilhelmy plate was easily disturbed by air movement. Many potential issues with this were avoided since the experiment was undertaken in a clean room with still air, however spikes in the data caused by air movement could be seen if the experiment was approached at anything more than a slow walking pace. This problem was only seen in the experiments performed in the small trough, the large trough was protected by a plastic cover. Therefore a cover for the small trough was 3D printed. This protected the Wilhelmy plate from these spikes and was used as described in the above experimental section.

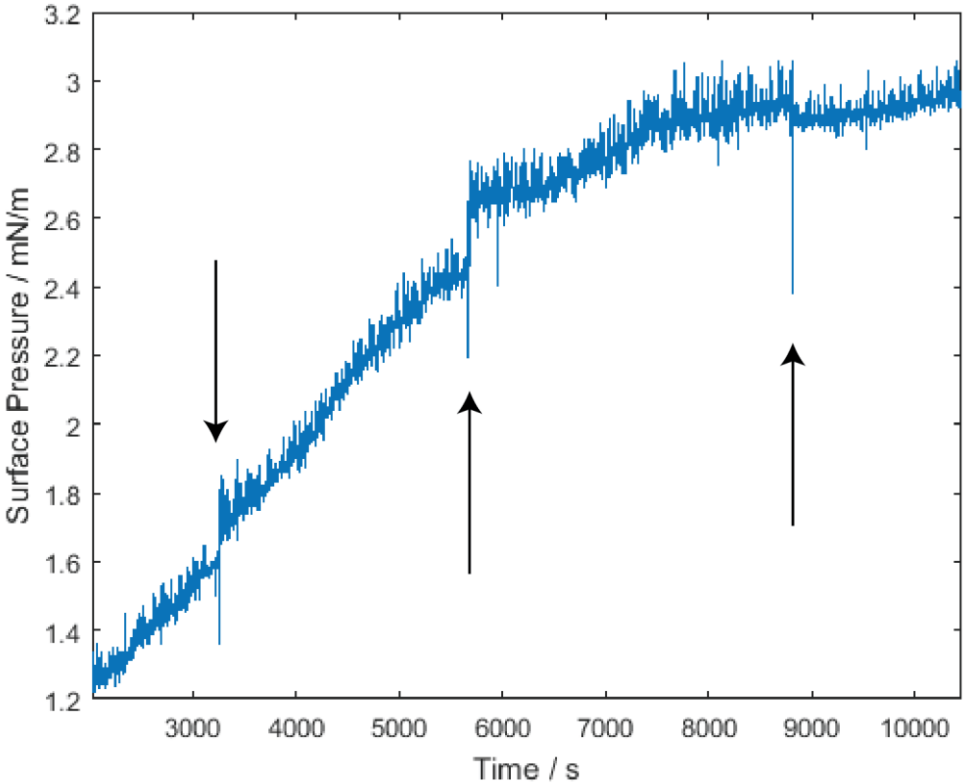

Figure 21 – Surface Pressure spikes caused by air movement highlighted by arrows.

Additionally, in longer experiments in the small trough, fluctuations were seen in the data over a time scale of tens of minutes. These were caused by changes in temperature in the lab causing small changes to the surface tension. These were not seen in the experiments with the larger trough, likely because of the much larger volume of water being less susceptible to temperature change. The final environmental factor noted to have a significant effect during experiments was evaporation. Due to the small volume of the small trough, small amounts of evaporation could have an impact on the concentration of the sample. Taking this into account, along with the effect of temperature fluctuations, experiments in the small trough were only run over moderate time scales, <3 hrs to ensure that these effects did not dominate.

3.2.4 – Compression

The small and large troughs had different methods of compression. Both had a PTFE barrier which could be compressed and expanded to change the surface area of the experiment. The barrier in the small trough was powered by a hand crank, and while it was suitable for rough experiments, it did not allow for fine control. The NIMA trough instead had a motorised barrier capable of compressing at a varying speed in cm^2/s.

3.3 – Tensiometry

In order to get absolute values for surface tension, tensiometry was also performed on PNP solutions of varying concentrations. A Kibron Ez-Pi Plus tensiometer was used to collect this data.

3.3.1 – Tensiometer Experimental

The tensiometer used in this work used a platinum wire, roughed to give infinite wetting. During the course of an experiment, the wire was slowly lowered into the sample. Upon making contact with the sample, detected by the change in force on the electrobalance, the wire continued downwards a short distance, ensuring that the tip of the wire was properly submerged. The movement of the wire was then reversed, and the force on the electrobalance was measured until the upwards force was great enough to break the wire free from the surface tension. This force was recorded and gave a reading of the surface tension. Between experiments, the platinum wire was cleaned by heating with a butane torch until it glowed. Calibration was performed regularly with deionised water to ensure that the readings remained accurate. This calibration involved measuring the surface tension of water, finding the offset between the experimental value and the known value of 72.4 mN/m and applying this offset. This was done automatically by the tensiometer.

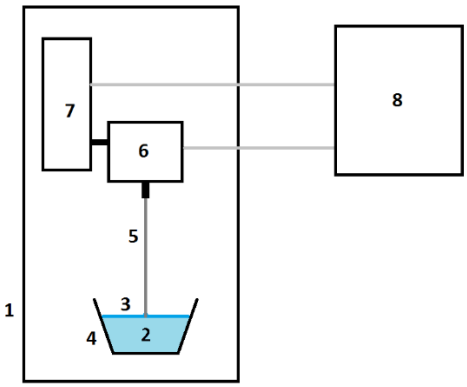

Figure 22 – Tensiometer Schematic. 1, Tensiometer Enclosure, 2, liquid subplase, 3 monolayer, 4, sample holder, 5, platinum wire, 6, electrobalance, 7, height control, 8, computer.

3.3.2 – Volume Sensitivity

Experiments in the tensiometer showed that it was sensitive to the volume of the sample. Readings below show surface tension readings for water as the volume of the sample was changed in 0.5 cm^3 increments.

Volume (ml)	Surface Tension (mN/m)			
4.0	74.24	73.95	73.91	73.83
3.5	70.59	70.89	71.02	71.08
3.0	69.44	69.46	69.45	69.42

Table 2 – Varying volume of water to test variability in surface tension

It can be seen that there is a variation of 5 mN/m purely by changing the volume by 1 ml. It was therefore important to have as consistent a volume as possible. The surface tension values are also most consistent while using a volume of 3 ml, so this was used for all readings.

3.4 – Ellipsometry

3.4.1 – Theory

Ellipsometry is a technique used to determine the complex reflectance ratio of thin films. This takes the form of two values, Ψ and Δ, shown below in equation 3.2. This can then be used to characterise the films optical properties, the refractive index, n, and the extinction coefficient, k, as well as the thickness of the layers through ellipsometric modelling. Ellipsometry is suitable for films of a thickness of up to 10 µm down to that of a few angstroms.

$$\rho = \frac{r_p}{r_s} = \tan(\Psi)e^{i\Delta} \qquad \textbf{(3.2)}$$

In the above equation, ρ is the complex reflection ratio, r_p and r_s are the amplitudes of the p and s components after reflection respectively, normalised to their incident value, where the p is parallel to the plane of incidence. This reflection can also be expressed as a complex number, as shown on the right side of equation 3.2. In this form, Ψ is the normalised ratio of p polarised light over s polarised light, and Δ is the phase difference. In ellipsometry, these values are calculated from the Stokes parameters of the incident and reflected light. Since this relies on the ratio of light between the incident and reflected beams, rather than the absolute values, this makes ellipsometry a powerful technique which is easily reproduceable.

From values of Ψ and Δ, the refractive indices (n), and the extinction coefficients (k) of the surface layers can then be calculated through ellipsometric modelling. This modelling consists of building a multi-layered system of known thicknesses and materials and calculating the value of n and k which would give the experimental values of Ψ and Δ. A simple ellipsometric model may include three layers, with air at the top, represented by void, then the sample, and then the substrate, such as silicon oxide. The void and substrate will have a full set of optical parameters, however the modelling of the sample allows for a level of unknown information which will be predicted from the

experimental data. In cases with a single layered sample, this should give a good agreement with the expected values for n, k and thickness, if they are known. A pitfall of ellipsometric modelling however, is trying to match the literature data too perfectly, this can lead to overly complex models, with many layers being built, which do not necessarily reflect reality.

3.4.2 – Experimental Procedure

A schematic for the ellipsometer used in this project, a Horiba Uvisel 2, is shown below in Figure *23*.

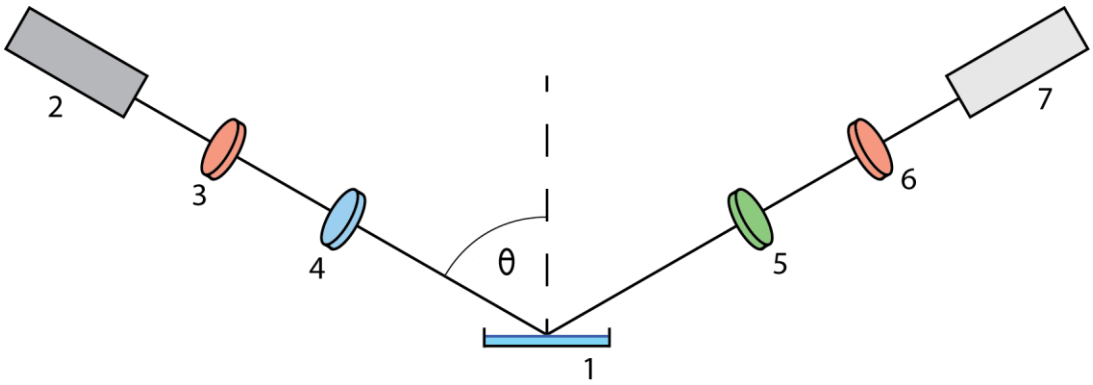

Figure 23 - Ellipsometer Schematic: 1 - Sample, 2 - Xenon Lamp, 3 - Monochromator, 4 - Polariser, 5 - Photoelastic Modulator, 6 - Analyser, 7 - Detector, θ is the angle of incidence.

A Xenon lamp is used in this ellipsometer as the light source. This generates unpolarised light over a wide wavelength range (190 – 2100 nm). The light is then monochromated, and linearly polarised at 45° between the s and p polarisations. During reflection by the sample, the light becomes elliptically polarised. This elliptically polarised light passes through a photoelastic modulator (PEM) which, in tandem with the subsequent analyser, another polariser, controls the polarisation of light which reaches the detector, in order to get the intensities of the p and s polarised light independently. The PEM is a quartz rod which exhibits birefringence according to its strain. The amount of strain is controlled by a piezoelectric transducer. By changing birefringence, the PEM acts as a waveplate. This then alters whether the p or s components of the incident light pass through the analyser, so they can be measured independently on the detector. A full ellipsometry experiment takes this procedure, and varies either the wavelength of the light, or the angle of incidence, or both. This builds up a spectrum which can be used for modelling.

3.4.3 – Alignment

For ellipsometry of solid samples, the Uvisel 2 ellipsometer used in this work has tilt functionality built into the sample stage. This allows the sample to be slightly rotated relative to the beam to ensure that it is perfectly perpendicular to the incident plane. This is important because deviation

from this alignment will affect the alignment into the detector, as well as the effective angle of incidence of the beam.

It is easy to see however, that changing the tilt of the stage will have no effect on the surface of a liquid sample, so in order to change the alignment between the beam and sample, the beam must be adjusted. In this case, this was performed by adjusting the height of the feet of the ellipsometer until the spot was visible using the ordinary tilt camera. This ensures that the beam is aligned azimuthally with the sample.

Additionally, due to the high precision of the angles of the arms of the ellipsometer which are required for the experiments which have been performed in this work, it is important to understand the accuracy of the angle reading from the ellipsometer. The ellipsometer does not measure the absolute value of the angle the arms are at, rather calculating it from the angle it is at before translation, and adding or subtracting the change. This is an acceptable method, assuming that the arms move the correct amount. It was found that when changing the angle by moderate to large amounts, >2°, there was an error of <0.1° which could occur in either direction. This effect was cumulative, and could cause the measured angle to drift slightly away from the actual value. This was measured using the Brewster angle of glass as a reference, and some data is shown below in Figure *24*. It can be seen that the data is consistent, but shifts on the x axis, showing the imprecision between angle measurements. It should also be noted that the Brewster angle of BK7 glass at this wavelength, 514.5 nm, is 56.66°. The Brewster angle measured in these experiments is approximately 55.8°, indicating that there is also an inaccuracy in the angle, in this case, approximately 0.85°. For experiments far from the Brewster angle of the sample, this inaccuracy is small enough that it does not need to be considered. For experiments around the Brewster angle, it is trivial to apply an offset to account for this inaccuracy, after comparing the difference between the expected and experimental values of the Brewster angle for both glass and the sample, to ensure they are the same. For experiments where the exact Brewster angle of the sample is unknown, by applying the offset calculated from that of glass, the approximate value of the Brewster angle can be found, though this cannot be stated with certainty to an accuracy ±0.1°.

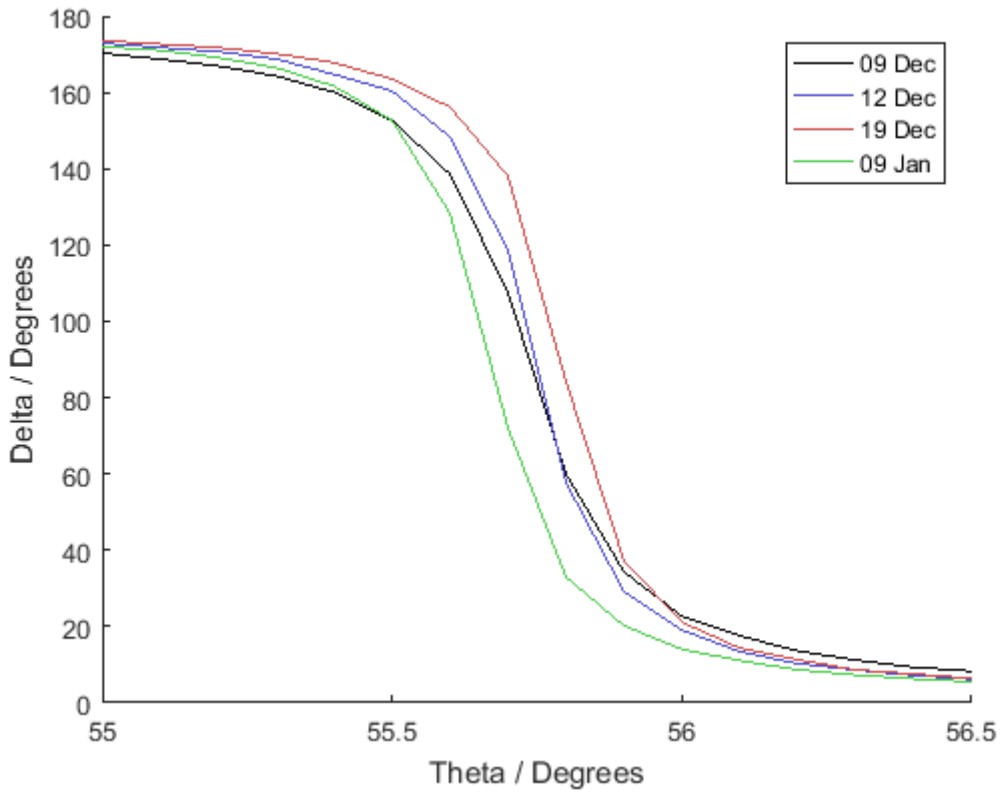

Figure 24 – Angle reference data collected over one month for Brewster angle of glass.

3.4.4 – Psi and Delta

Figure *25* shows the difference in Ψ and Δ for water and a 30 mM PNP solution at 70° AOI. At this angle of incidence, far from the Brewster angle, Δ is consistent around 360 while Ψ varies more. Since Δ is the phase difference between the s and p polarised light, it is measured in degrees. As a result, the data points above 700 nm which have approximately Δ = 0.5° represents a minimal amount of noise since 0° = 360°.

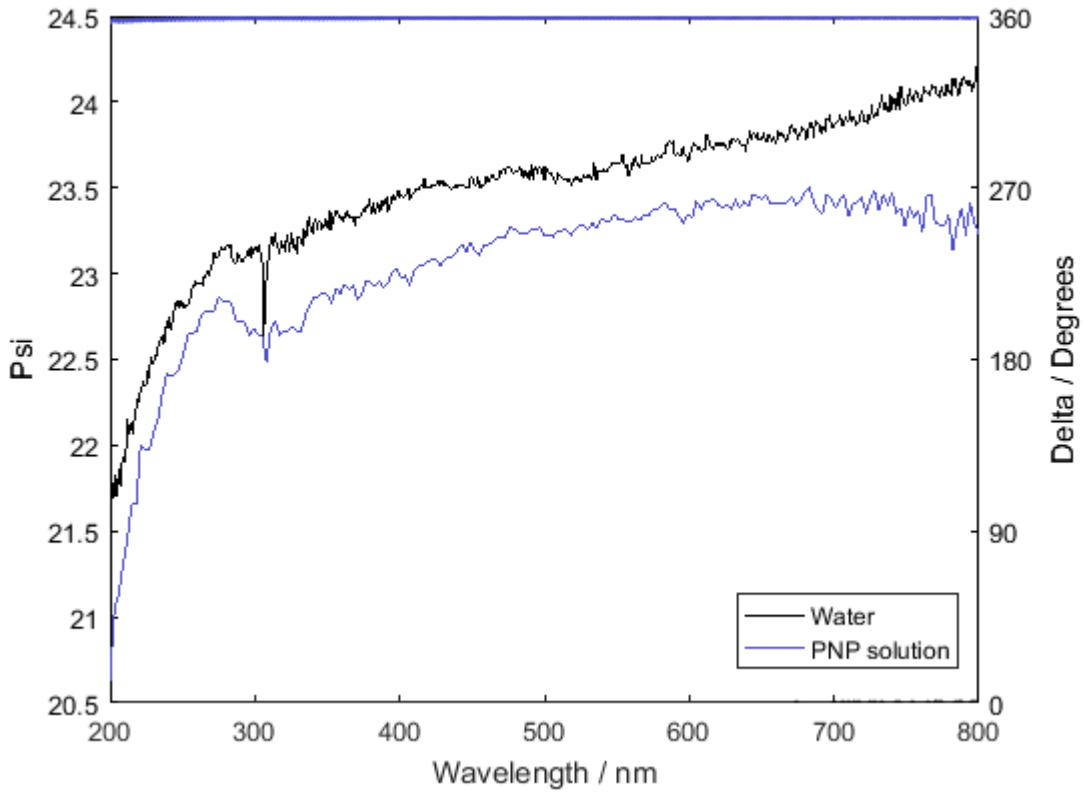

Figure 25 – Comparison of Ψ and Δ data at 70° AOI for water and 30 mM PNP solution. Ψ is plotted as a solid line, Δ as scatter plot.

3.4.5 – Liquid Ellipsometry

Ellipsometry is typically used to characterise the optical properties of solid samples. Ellipsometry of liquids is possible, but has its own challenges to overcome. Signals are usually very weak from liquids in ellipsometry, this makes noise an issue when collecting data. Liquid surfaces also move during the course of experiments, unlike solid samples, capillary waves disrupt the surface of the liquid, making it more challenging to collect high quality data. This makes the solid/liquid interface the easiest liquid interface to probe with ellipsometry, since there would be no capillary waves. However, due to the different chemical environments, the air/liquid interface would be very different to the solid/liquid interface for a given liquid. Glass for example is hydrophilic compared to the air, which would have a profound impact on the air/water and glass/water interface.

As discussed in section 1.1.4, air/liquid interfaces have different refractive index than the bulk liquid, whether it is higher or lower than the bulk depends on the liquid in question. This means that ellipsometry is sensitive to the surface layer of liquids and can determine their optical properties, rather than those of the bulk.

3.4.6 – Anti-Vibration control

An additional consideration to be made when running experiments on liquid samples are the problems caused by vibrations. Vibrations lead to movement of the liquid surface which will disrupt the alignment of the beam into the detector, as well as potentially changing the surface structure of the sample. Three steps have been taken to minimise surface movement. Firstly the ellipsometer was mounted on a gas damped table. This acted to soften any vibration from outside the table. This alone did not remove all vibrations, because due to the moving parts in the ellipsometer, as it operated, this also caused vibrations, therefore liquid samples were mounted on a two layer system of rubber and polystyrene to absorb these vibrations. In tandem these methods worked to reduce the problems caused by vibration to a useable level.

Air currents can also cause movement at the surface, so in addition to the anti-vibration techniques used for liquid samples, the sample was contained in a box where necessary to further isolate it from the environment. This box had holes in the walls to allow the beam to pass through unaffected, so as not to effect the experiment. This was found to have a lesser effect on improving the data than the anti-vibration techniques due to the fairly still conditions within the lab.

3.5 – Single Crystal X Ray Diffraction

Single Crystal X Ray Diffraction (SCXRD) is a common technique used to elucidate the position and orientation of molecules within crystals. This is possible by measuring the elastic scattering of X rays through the crystal due to Bragg diffraction. Bragg diffraction causes reflections to be observed when the path length of X ray through the crystal as it is diffracted is an integer multiple of the wavelength of the X ray. This causes constructive interference between the reflections of different layers, and therefore intense spots can be seen in the resulting diffraction pattern. The location of these spots is determined by Bragg's law, shown in equation 3.3, where n is any integer, λ is the wavelength of the X ray beam, d is the separation of the layers in the crystal and θ is the angle of incidence.

$$n\lambda = 2d\sin(\theta) \quad \textbf{(3.3)}$$

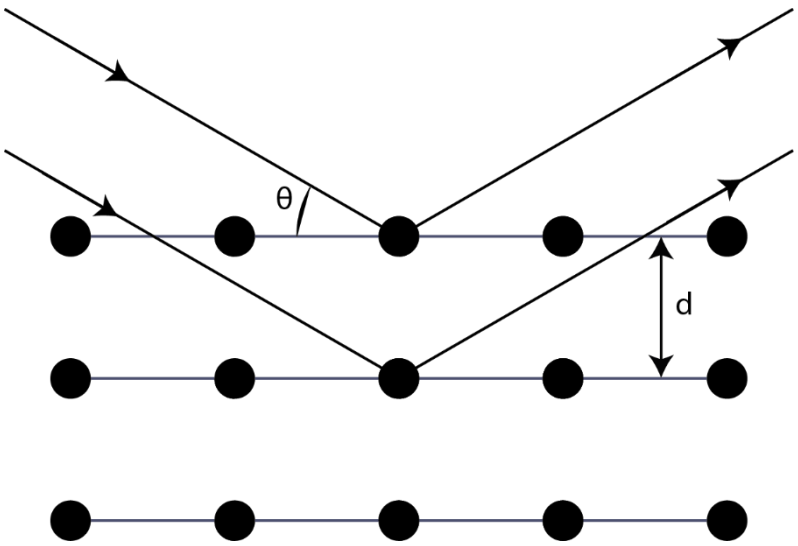

Figure 26 – X ray diffraction.

Non-Bragg diffraction is observed in SCXRD experiments from any diffraction which is not caused by the mechanism shown above. Non-Bragg scattering is commonly seen as a line between two Bragg peaks.

Single crystal x ray diffractometers operate by mounting the sample crystal on a goniometer whereby it can be freely rotated through an arc while the X ray beam diffracts through it, creating a series of diffraction patterns which can be reconstructed into the chemical structure of the crystal. Each spot in the diffraction pattern is the reflection of one Miller plane in the crystal structure, so the rotation of the crystal through the course of the experiment can cover many different indices. The intensity of the peaks seen in SCXRD is determined by the size and quality of the crystal. Defects in the crystal structure lead to less constructive interference, and so weaker reflections, while smaller crystals have fewer planes, and so fewer reflections.

Chapter 4 - Crystal Growth Studies

This chapter aims to study crystallisation through multiple techniques. Initial crystallisation and hot stage microscopy tests were performed to create samples for later experiments in this chapter and chapter 5 as well as to test Methylbenzylaminonitropyridine (MBANP) for any unknown polymorphs which had not been noted previously in the literature.

Secondly, as noted in chapter 2, PNP undergoes a photochemical change when the α polymorph is exposed to UV light. Past literature work has suggested that the colour change which is observed is caused by the shift of the phenolic hydrogen, but the evidence is not conclusive. In order to investigate this further, an experiment was planned to attempt to gain a fully irradiated sample of PNP and to recrystallize it in order to gain good quality crystals which could be tested by X ray diffraction. From this it would be possible to shed further light onto the chemical change which causes the dramatic colour change of the irradiated PNP crystal and to better understand the mechanism of this change.

Finally this chapter aims to study the relationship between Bragg and non-Bragg scattering in single crystal X ray diffraction by subliming a urea crystal to decrease its size as multiple SCXRD experiments are run. Typical SCXRD experiments observe strong Bragg scattering, however at small crystal sizes and for crystals with complex molecules, such as proteins, non-Bragg scattering is much more apparent. This experiment aims to use urea as a simple test to observe how the change in size of the crystal affects the levels of Bragg vs non-Bragg scattering.

4.1 – Crystal Sample Growth

To create samples for later SHIM experiments and x ray sublimation experiments, various NLO active crystals were grown by slow growth method and through Hot Stage Microscopy (HSM). A variety of samples were grown, all of which have been noted in the literature for their NLO properties. Table *3* shows a list of the compounds used, and the solvents that crystals were grown from.

Compound	**Solvents**	**Melt**
Urea[99]	Water	Yes
Methyl p-Hydroxybenzoate (MHB)[100]	Acetone, Diethyl Ether, Methanol	Yes
4-nitro-4 -methyl benzylidene aniline (NMBA)[101,102]	Acetone, Ethyl Acetate	Yes
4-(N,N-Dimethylamino)-3-acetamidonitro Benzene (DAN)[103–105]	Acetone, Methanol	Yes

L-Phenylalanine[106,107]	Water, Ethanol, Methanol	No
L-Tryptophan[106]	Water	No

Table 3 – Samples grown for SHIM by slow crystal growth.

In addition to this, a more in depth study was undertaken on Methylbenzylaminonitropyridine (MBANP) to search for additional polymorphs which had not been previously noted. The following solvents and combinations of solvents were tested: acetone, ethanol, methanol, toluene, acetone/ethanol, acetone/methanol, acetone/toluene, acetone/water, methanol/ethanol, and methanol/toluene. A sample was also prepared via HSM. These samples were tested through powder x ray diffractometry (PXRD) however all of these combinations show the same diffraction pattern, which corresponds to the known polymorph. A selection of these are shown in Figure *27*.

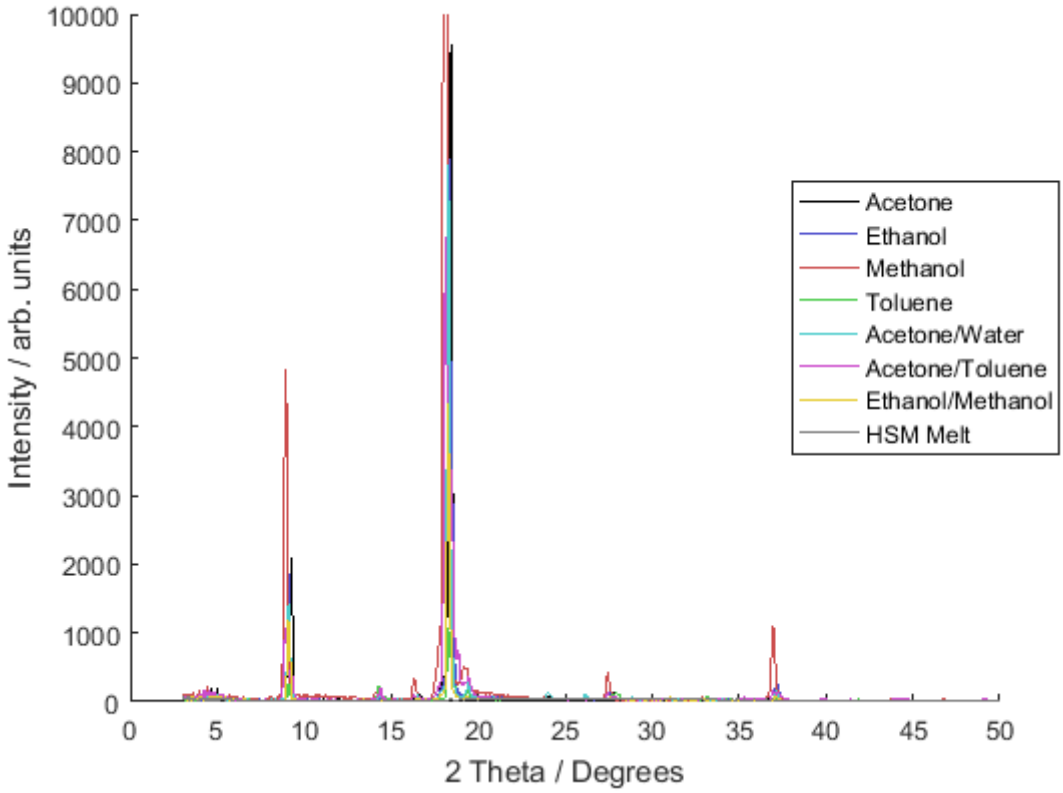

Figure 27 – PXRD spectra of MBANP samples. Due to the much higher intensity of the red data set for methanol, the y axis was limited to 10000 in order to see the other data clearly.

4.2 – PNP Irradiation

Past published work shows a variety of experiments which have attempted to elucidate the structure of the irradiated form of the α polymorph of PNP[63,83–85,87,108]. The most common explanation given is that it is hydrogen transfer from the phenol group to the nitro group. This is explored in more detail in Chapter 2. Past work within the group suggests however that the PNP

crystals used within these experiments were not fully irradiated. These papers report irradiating PNP with UV light until they achieve a dark red/brown colour. Cutting PNP crystals prepared in this manner in half show that the majority of the crystal retains the original pale yellow colour, and only the surface is darkened. This suggests that the initial irradiation makes the outside of the crystal opaque to the UV light, and as such, the inside of the crystal cannot be irradiated under these conditions. SCXRD experiments of these partially irradiated crystals would therefore show the crystal structure of the α polymorph of PNP, because the majority of the crystal has been unchanged by the irradiation.

To circumvent this issue, a sample of PNP was finely ground with a mortar and pestle, and irradiated with a broadband UV lamp. The grinding was repeated daily for 5 days until the red colour persisted after grinding, rather than fading towards the original pale yellow colour, indicating that the entirety of the PNP had been converted to the irradiated state.

In order to get a sample for SCXRD, this powder was then recrystallized in three different solvents, water, acetone and diethyl ether. When dissolved in all three solvents, a red/orange solution was obtained, though the redness quickly disappeared in water, and the solution turned to the yellow colour typical of PNP solutions. The red/orange colour stayed in both the acetone and diethyl ether solutions, though better crystals were formed from the ether solution. These observations support the theory that the irradiation causes an intermolecular hydrogen transfer. When dissolved in water, the structure was free to convert back to the more stable phenol and phenolate structures in solution, while in organic solvents, the new structure was kept.

SCXRD of the irradiated crystals grown in ether showed curious results. Four crystals were tested from this sample, all thin plates. Two of these crystals had a unit cell equal to that of the α polymorph of PNP, and the other two had a unit cell equal to that of the β polymorph. These experiments were performed in two pairs, three weeks apart. Each pair of experiments had one crystal of each unit cell. The distribution of the electronic charge within the crystal suggests that the molecules of the irradiated PNP crystal closely resemble that of PNP in all four cases. These experiments did not have the same resolution of the charge density studies performed by Kulkarni, so it is not possible to see the exact locations of the hydrogens in the structure to confirm whether the hydrogen transfer mechanism is correct for the irradiation of PNP.

This is different to the previously published results wherein there was a change in the location of the charge within the crystal, however the unit cell remained that of the α polymorph. Nonirradiated PNP crystallised from diethyl ether grows in the α form, so it is unclear what caused the growth of the β polymorph, which ordinarily only grows from water. In order to gain a better understanding of

the crystal structure of this form of irradiated PNP, it would be beneficial to run higher resolution SCXRD experiments similar to those performed by Kulkarni. This could help to show the location of the hydrogen which is theorised to have transferred to the nitro group and to see how both polymorphs are intermolecularly bonded compared to the known α and β polymorphs of PNP.

4.3 – Single Crystal X Ray Diffraction Sublimation Experiment

An experiment was undertaken to watch the change in intensity of the Bragg reflections of a crystal as it decreased in size to study the effect of size on Bragg vs non Bragg reflections. Urea was selected as the sample, because the most common crystal form of urea, grown from water, is capable of sublimation. Sublimation was advantageous compared to melting because as the crystal sublimes, it would not be coated in a liquid layer, which could interfere with the experiment, rather it would disperse as a gas. Under HSM conditions, urea sublimed slowly around 105 °C, before melting at 130 °C, however under the conditions used in this experiment, and in order to achieve sublimation over the course of hours, a lower temperature of 70 °C was used in order to see slow sublimation.

The N_2 cryo stream was used as the source of heat in this experiment. Ordinarily this is used to cool samples down to low temperatures in order to reduce the amount of molecular movement, and thus increase the quality of the diffraction patterns. Instead, this gas stream was heated to 70 °C and used to heat the sample. This has the side effect of decreasing the quality of the data collected, however it was found that the data was still useable at this temperature, and the alternative method of subliming the crystal for a set time and then cooling it to take a set of images would have taken much longer to complete, with a minimal increase in quality. As a result of operating at high temperature, the crystal had to be glued onto the goniometer rather than being frozen on with oil.

Figure *28* shows the crystal glued to the tip of the goniometer before and after the experiment, from front and side perspectives. The initial dimensions of the crystal were 0.26 mm by 0.35 mm by 0.09 mm. Eight sets of images were then taken over 5 hours. Each experiment took approximately 30 minutes to run, and then 5 minutes were taken to measure the crystal dimensions and reset the experiment.

Figure 28 – Urea crystal used in SCXRD sublimation experiment glued to goniometer tip. Top left, front view before experiment, bottom left, side view before experiment, top right, front view after experiment, bottom right, side view after experiment.

Figure *30* shows a diffraction pattern taken in the first collection of the experiment. The highlighted spot was selected and the volume of the spot was calculated from the sum of the intensities for each data set. This was then compared to the crystal thickness which was measured from the optical images of the crystal which is shown in Figure *31*. This spot was selected because it was near enough to the centre that it did not disappear in the later experiments, but was far enough out that it was not affected by the higher levels of noise which can be seen at the centre of Figure *30* caused by inelastic scattering of the x ray beam.

Figure *31* shows the decreasing intensity of the x ray scattering with decreasing crystal thickness. This projects that the peak will disappear at a thickness of 0.04 mm. Due to the presence of the glue used to stick the crystal in place however, it was not possible to accurately measure the thickness of the crystal beyond this point.

Non-Bragg diffraction can be seen between the Bragg peaks in Figure *29*, and weakly in Figure *30*. This is not to be confused with the smeared Bragg peaks which can be seen in Figure *29* due to the stacking faults in the crystal leading to unit cells being offset across the crystal. Comparatively to the change in intensity of the Bragg peaks, the Non-Bragg diffraction can be seen to persist more in the outer regions of the diffraction pattern in Figure *30*, after the crystal has been sublimed for several hours.

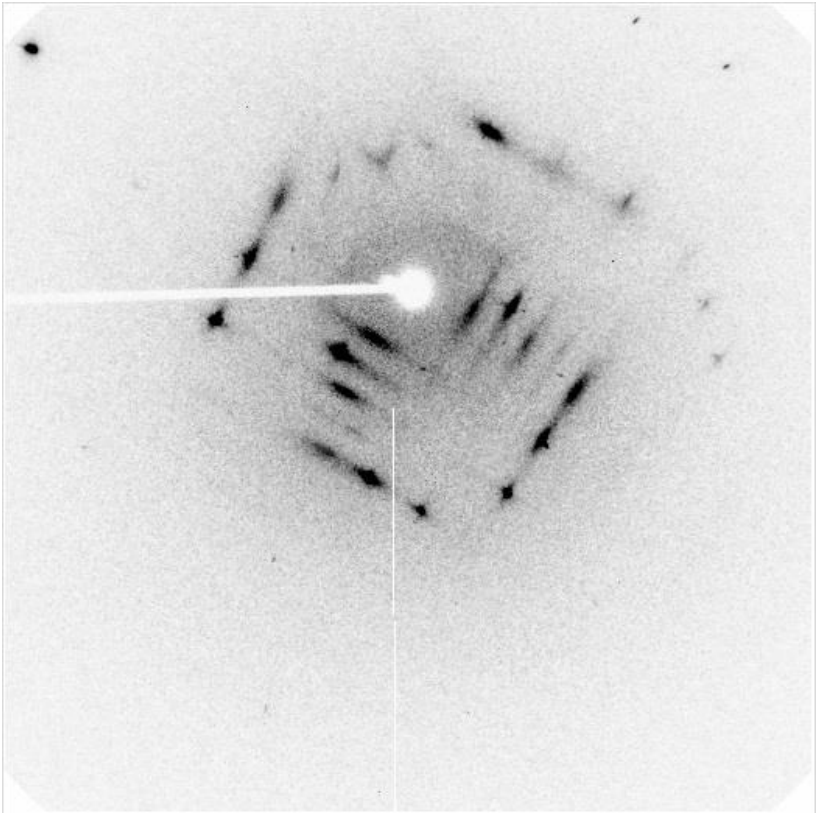

Figure 29 – SCXRD pattern from experiment 1 showing Bragg and non-Bragg diffraction.

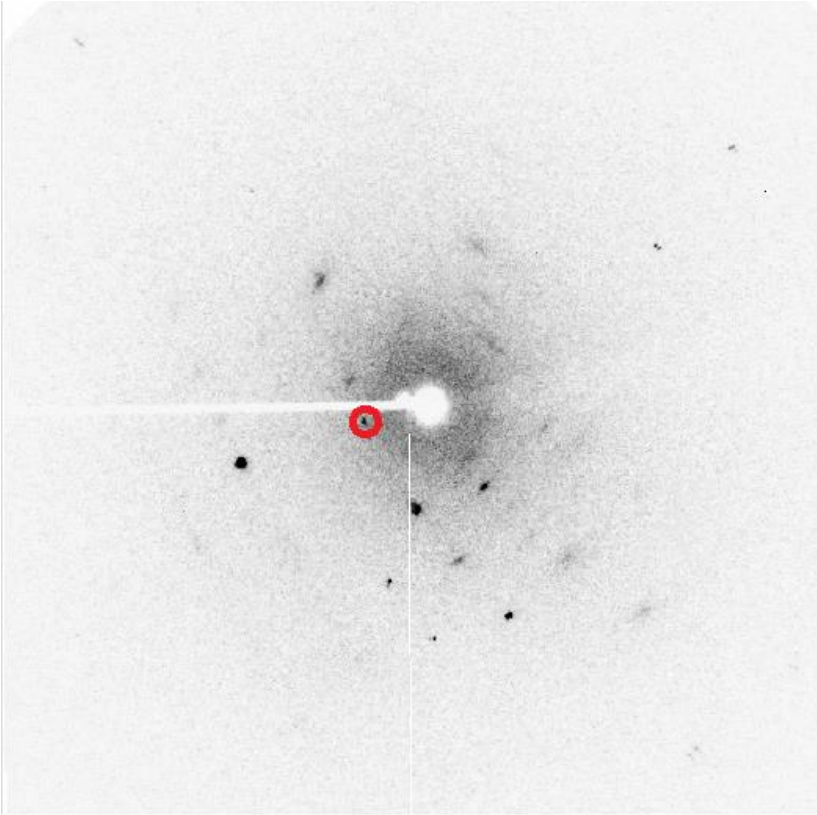

Figure 30 – SCXRD pattern from experiment 8 with analysed spot highlighted. Fewer Bragg peaks are still visible, with weak non-Bragg diffraction in between them.

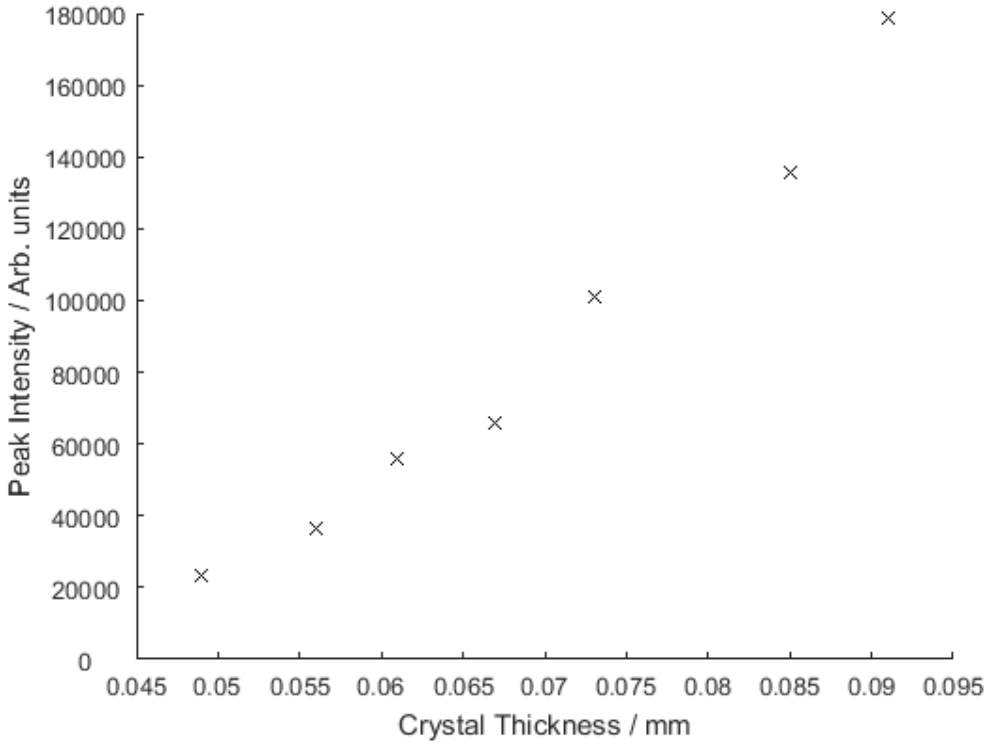

Figure 31 – Crystal thickness vs Peak intensity over eight experiments.

4.4 – Conclusions and Further Work

Initial crystallisation experiments created the samples which were needed for further experiments in this chapter and chapter 5, however the search for new polymorphs of MBANP was unsuccessful. The solvents and solvent mixtures used in this work all created the known polymorph of MBANP which is noted in the literature.

Fully irradiated PNP samples were created, beyond the levels of irradiation which have been noted in the past literature, through grinding and repeated irradiation. This sample was then recrystallized and analysed by SCXRD to give unit cells of the same size and shape as the α and β unit cells of PNP. This different to past literature reports which maintained the unit cell of the α polymorph. Compared to the literature experiments, the SCXRD results are much lower resolution, and do not give as much information regarding the exact atomic positions, due to the shorter collection time for the data, but they show that the irradiated form persists through dissolution in organic aprotic solvents and show the irradiated compound is stable in a structure similar to both PNP polymorphs. This supports the assertion that the structural change caused by irradiation is a fairly minor difference, such as the shift of the phenolic hydrogen, though it cannot confirm this hypothesis.

A novel method was developed to achieve sublimation of a crystal during SCXRD experiments. The ideal conditions for a urea crystal were found, to allow sublimation over the course of several hours. This allowed the collection of multiple data sets of the same crystal as it sublimed, showing the change in intensities of the Bragg and non-Bragg diffraction. Some simple analysis of the change in intensity of the Bragg diffraction was performed however due to constraints with the software used to model the changes in the crystal at small sizes, this work was not pursued further. As a result, the initial aim of this work to investigate the intensity of the non-Bragg diffraction of these experiments was not achieved.

Further to this work, it would be beneficial to run higher resolution SCXRD experiments on the irradiated PNP crystals in order to gain a better understanding of their structure. Charge density studies of these crystals may provide more insight into the differences in structure between the α and β polymorphs of PNP, the partially irradiated PNP crystals previously studied, and the fully irradiated PNP samples created by this work. Additionally, it may be fruitful to test the reactivity of this irradiated PNP since it is stable in organic solvents. Since the proposed mechanism for the change involves a hydrogen shifting between the functional groups of the PNP molecule, it is logical to assume that this will affect how it would react chemically, though care would have to be taken with the reactions chosen in order to make sure that they do not introduce H^+ ions into solution to allow the conversion back to PNP.

Further investigation of the non-Bragg diffraction would require analysis of the diffraction patterns collected in these experiments. Calculations of the intensity of the non-Bragg diffraction would require the removal of both the Bragg peaks and background noise. This would give an estimate of the level of non-Bragg diffraction which is seen in each experiment.

Chapter 5 – Second Harmonic Imaging Microscopy

Understanding the quality and growth of crystals is an important aspect of crystallography. In order to study these properties, a second harmonic imaging microscope was built for this work, as detailed in Chapter 3. The aim of the work performed in this chapter was to image crystals at a µm scale using their second harmonic properties. To this effect, a selection of NLO active crystals were grown, which were discussed in section 4.1 of this work. These compounds were chosen due to the intense SH signals which they were capable of generating because of their noncentrosymmetry. Initial experiments were performed to optimise the scanning microscopy experiment, to ensure that the experiment had maximum sensitivity to the SH signal produced and to gain the highest possible resolution for the images by attaining the tightest focus of the beam in the sample. Further experiments were planned to use this scanning microscope and the narrow depth of field capable of generating the second harmonic to map slices through a crystal to build a 3D map of the crystal.

In tandem with this, a second experiment was designed using the microscope to watch crystallisation. In this experiment, a single point was observed over the course of an hour as a sample crystallised. The intensity of the second harmonic was measured with time as the crystal grew. After developing a method to reliably observe the second harmonic from a growing crystal, further experiments were planned to widen the focus of the beam in order to produce an image of the second harmonic signal which could be measured, instead of a single spot. This posed a challenge with keeping the required intensity of light in order to produce the second harmonic, but could give greater insight into the relationship between a growing crystal and its second harmonic signal.

5.1 – Amplitude Data

Figure *32* shows images taken of a DAN crystal grown for this work. They each show a 40 µm square area. The left hand images show the seconds of the camera pictures which were imaged in these experiments, while the amplitudes of the SH signals are shown on the right. The top and bottom pairs of images show sections of the same crystal. The amplitudes of the SH signal in Figure *32* vary around 2-3 V, with the exception of 10 V around the edge of the crystal in the top image.

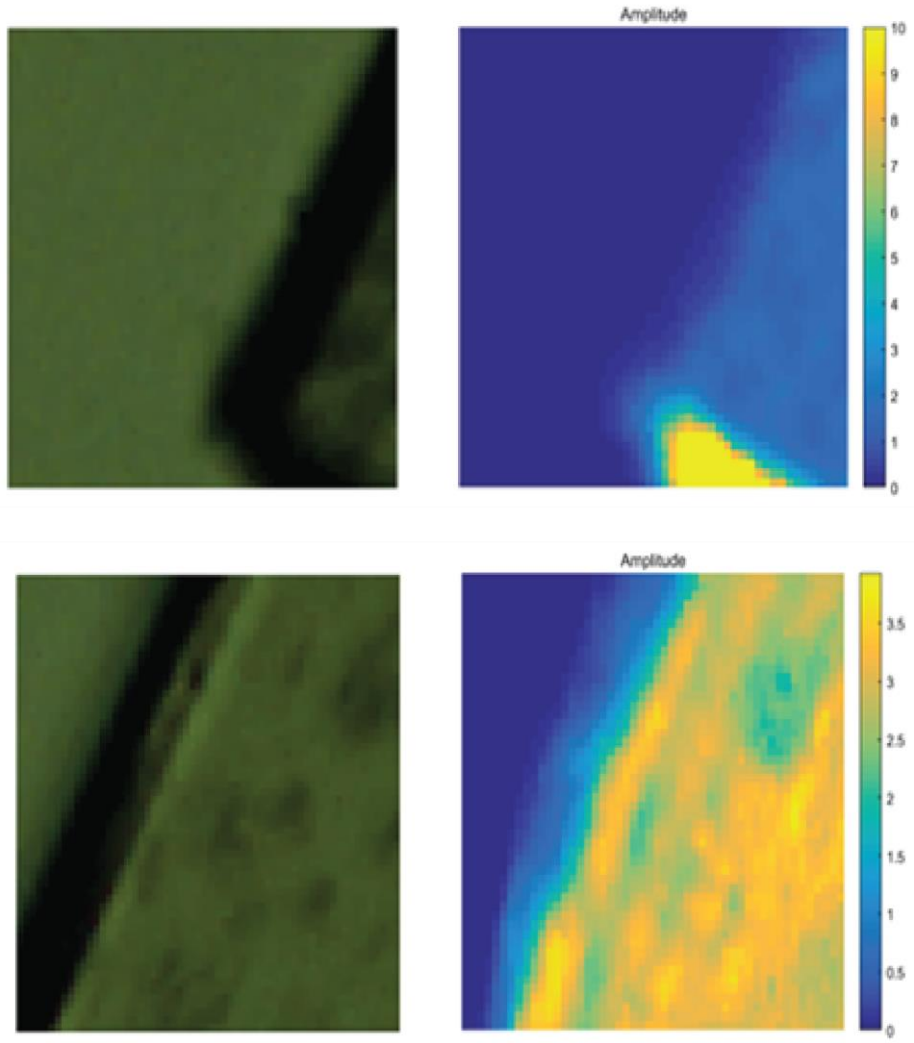

Figure 32 – SHIM image of different sections of a DAN crystal. Left images are optical camera images, right images are amplitudes of the SH signal from the lock in amplifier. Top images show the corner of the crystal. Bottom images show the edge of the crystal.

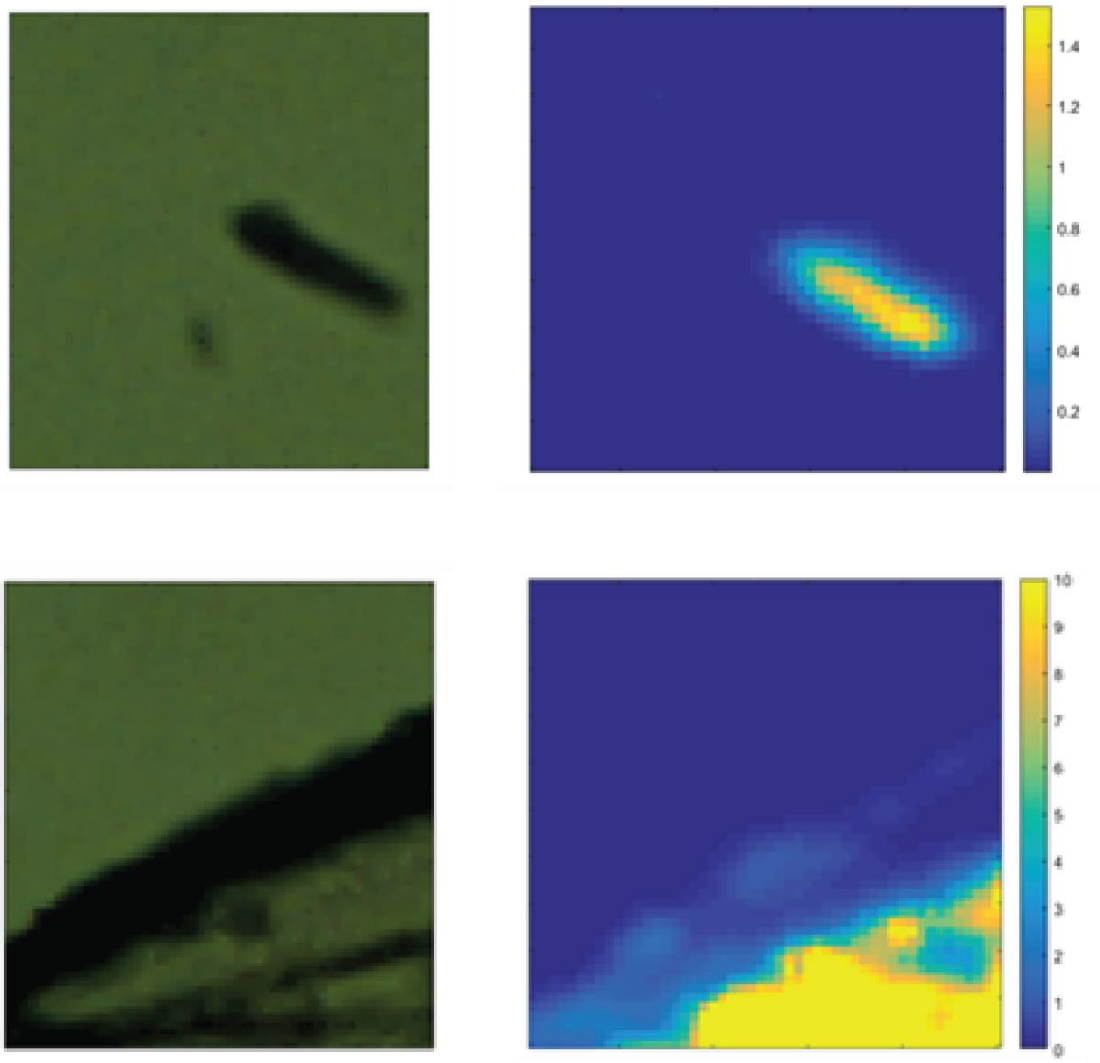

Figure 33 – Two SHIM images: MBANP melt (top) and MBANP crystal edge (bottom). Left images are optical camera images, right images are amplitudes of the SH signal from the lock in amplifier.

Figure *33* shows two further images taken of two MBANP crystals. The top image shows a small crystal a few microns wide, which clearly shows with an SH intensity of over 1.4 V. The lower half of the image shows part of a larger MBANP crystal. In the bottom right of the image, an area of much lower SH signal can be seen compared to the surrounding area which matches with the flaw in the crystal which can be seen in the optical image.

5.1.1 – Amplitude Variance

In addition to the images shown above, Figure *34* shows regions within crystals with variable intensity of SH signal. The top half of Figure *34* in particular shows regions of strong SH signal (7 V), while most of the crystal is generating a much weaker signal (4 V). This matches features in the

optical image of the crystal with the higher intensity SH signal corresponding to the darker patches of the crystal.

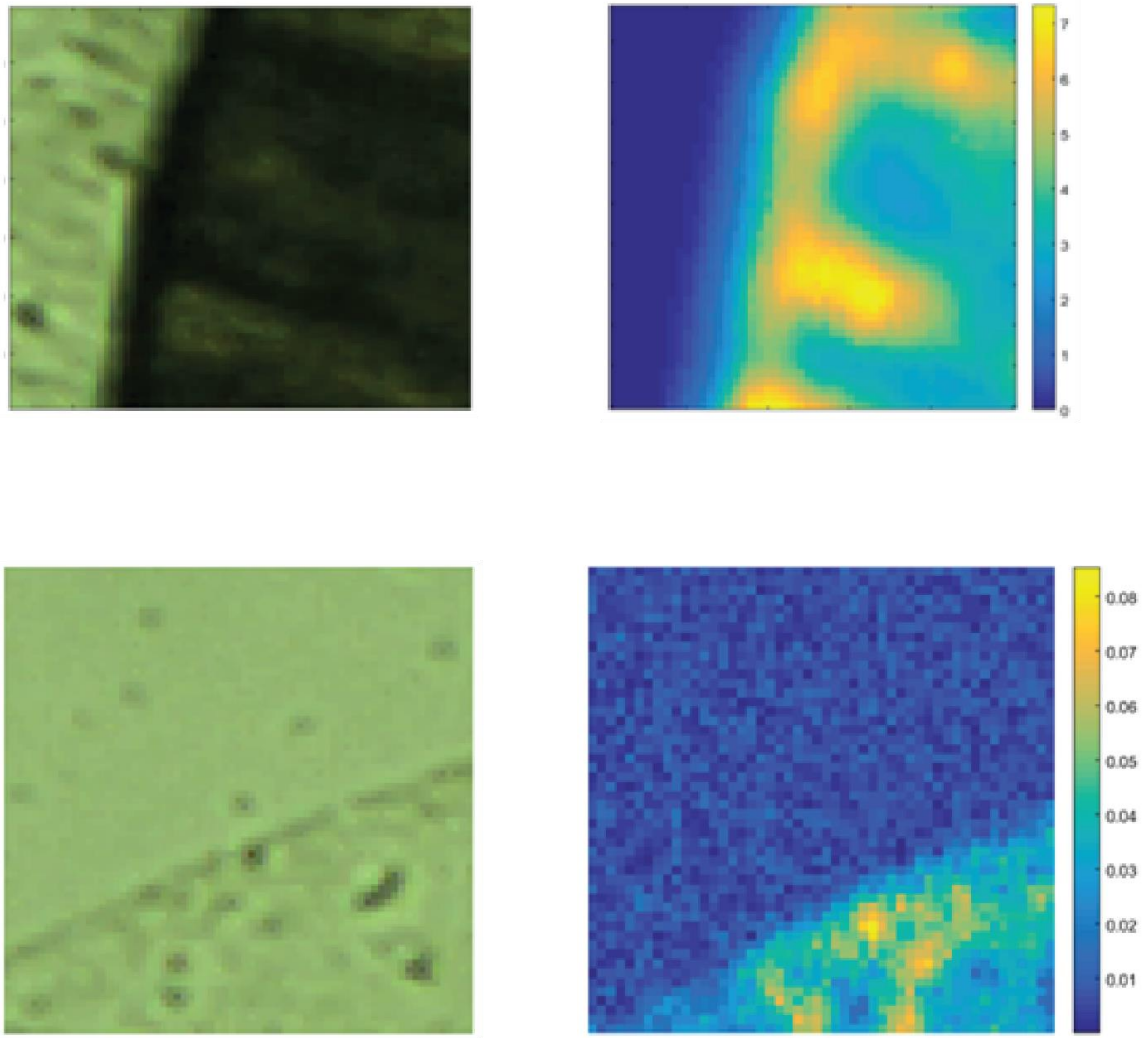

Figure 34 – SHIM images of two samples: the edge of a DAN melt crystal (top) and the edge of a thin DAN melt (bottom). Left images are optical camera images, right images are amplitudes of the SH signal from the lock in amplifier.

5.1.3 – Low Intensity Images

Several experiments were performed on samples which were much thinner than the millimetre sized crystals used above. The bottom half of Figure *34* shows the edge of a DAN crystal prepared by HSM. The sample was a crystalline film on the surface of a glass slide. Even within these thin, weakly generating samples, the SH signal can clearly be seen in the amplitude, and areas within the crystal which generate stronger intensities of SH light.

5.2 – Crystallisation Experiment

Since the experiment described above was capable of observing SH signals from weakly generating, thin samples, a further experiment was developed in order to try to observe nucleation and the early

stages of crystal growth, over the period of an hour. Instead of imaging an area with the Nanonics piezoelectric stage, a single point was imaged since this meant the sample was not disturbed by movement, and it gave a continuous reading of data for a single point. The data was collected as detailed in section 3.1. A small volume of liquid of between 5-50 µl was used in these experiments since only the initial crystallisation process was important rather than the longer term crystal growth. Urea was selected to be grown because it is simple, safe, and has a high solubility in water, making it easy to work with. The solution was held upon a small silicon plate with a 100 µm square hole to allow the solution to be suspended over an open area. The plane of focus of the microscope was placed at the bottom edge of the solution within the hole of the plate because it was found that this was the most likely place to observe early crystal growth. Only the amplitude of the SH signal was measured in these experiments, and not the phase, since the prior experiments have shown that the only signal detected is the SH signal, so the phase is not required to verify it.

Figure *35* shows a screenshot of a crystallization experiment taken from the video “Crystallising 1.mp4”. The SH signal starts increasing after approximately 1000 s, starting with a single peak of 0.45 V and then gradually increasing with time. Troughs can be seen in the signal, notably at 2000 s. These troughs could be caused by the laser damaging the crystal over time. Examples of this are shown in Figure *36* and in the video “Crystallising 2.mp4”. As the crystal continued to grow, the SH signal would continue to increase after the damage occurred.

The initial spike at 1000 s appears shortly after initial crystallisation. It is probable that this spike in intensity is caused by a small crystallite floating through the beam since it generated much more intensely than the subsequent 500 s. “Crystallisation 3.mp4” shows an experiment wherein the initial crystallisation stage was missed and instead the crystal grew over the laser spot in the latter stages of the experiment. This was an issue during this experiment, since it was not known where crystallisation would start in the sample and so it was easy to miss the early stages.

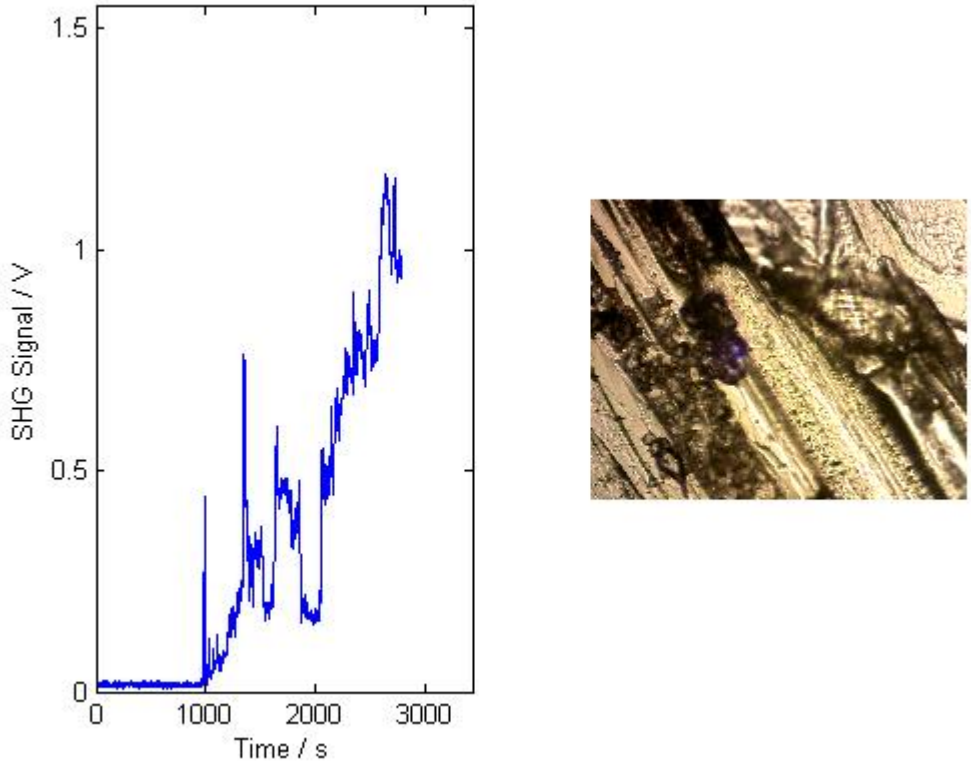

Figure 35 – Recrystallisation of urea. SH spot can be seen in image centre left as a purple spot.

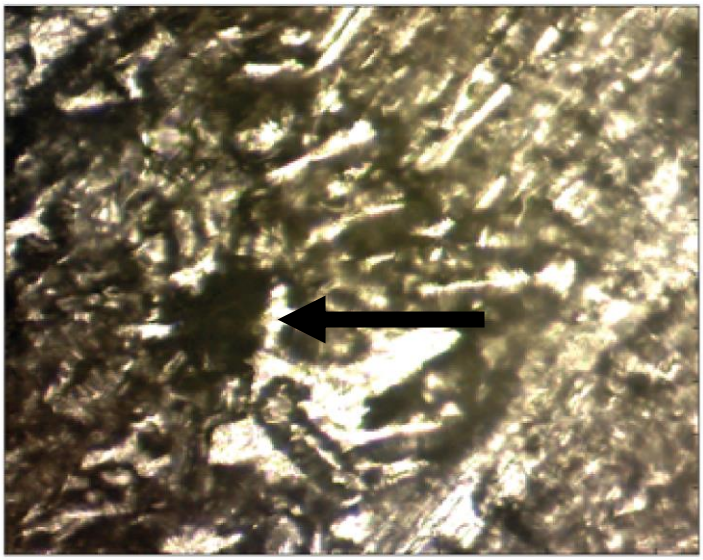

Figure 36 – Laser Burn on crystal in centre left of image highlighted by an arrow.

5.3 - Equipment Malfunction

Unfortunately after performing these experiments, the MIRA laser was no longer able to sustain stable modelocking for long enough time periods to continue these experiments. This was caused by the degradation of the laser diodes which had passed their expected lifetime. As a result it was not possible to continue these second harmonic microscopy experiments.

5.4 – Conclusions and Further Work

In the work performed for this chapter, a second harmonic imaging microscope was successfully built and tested. This microscope has a similar resolution to other second harmonic microscope systems such as SONICC[109]sonson, able to observe crystals that are <5 µm in size and image crystals that are 10 µm across or larger.

A new crystallisation experiment was built and refined to watch the second harmonic signal of a growing crystal. This experiment showed promising results with the observation of intense second harmonic signals at the start of crystal growth, likely caused by the presence of small crystallites in solution.

To continue these experiments to further fulfil the aims of this project, it would be useful to continue both experiments which were performed in this chapter. Continued second harmonic imaging microscopy experiments could be undertaken to test the depth of field in the microscope and to use this to build 3D maps of the imaged crystals. This could allow greater insight into the presence of defects within the crystals and could be paired with other techniques such as single crystal X ray diffraction in order to study these defects in greater detail.

The next stage of the crystallisation experiment was planned to loosen the focus of the laser spot to image a broader area of the crystallisation experiment rather than measuring a single spot. This would require a high intensity of light because increasing the radius of the spot by 2, quarters the intensity across the area, however if successful would allow further insight into the early stages of crystal growth through measuring second harmonic.

Chapter 6 – p-Nitrophenol Study

This work was performed at Cranfield University working with Dr Matthew Partridge of the engineering photonics group. Data has also been included of past unpublished data from KTH, Stockholm of surface tension data of PNP in water at varying concentrations and temperatures.

6.1 – Small Langmuir Blodgett Trough Work

6.1.1 – 15 mM Data

Initial LB experiments found an increase in surface pressure with time for PNP solutions. Figure *37* shows data for a 15 mM solution. This experiment was repeated for varying concentrations, however there were some issues found with repeatability. These have been discussed earlier in section 3.2.3, and encompass environmental factors as well as additional conditions of the sample which needed to be controlled including temperature and preformed structure.

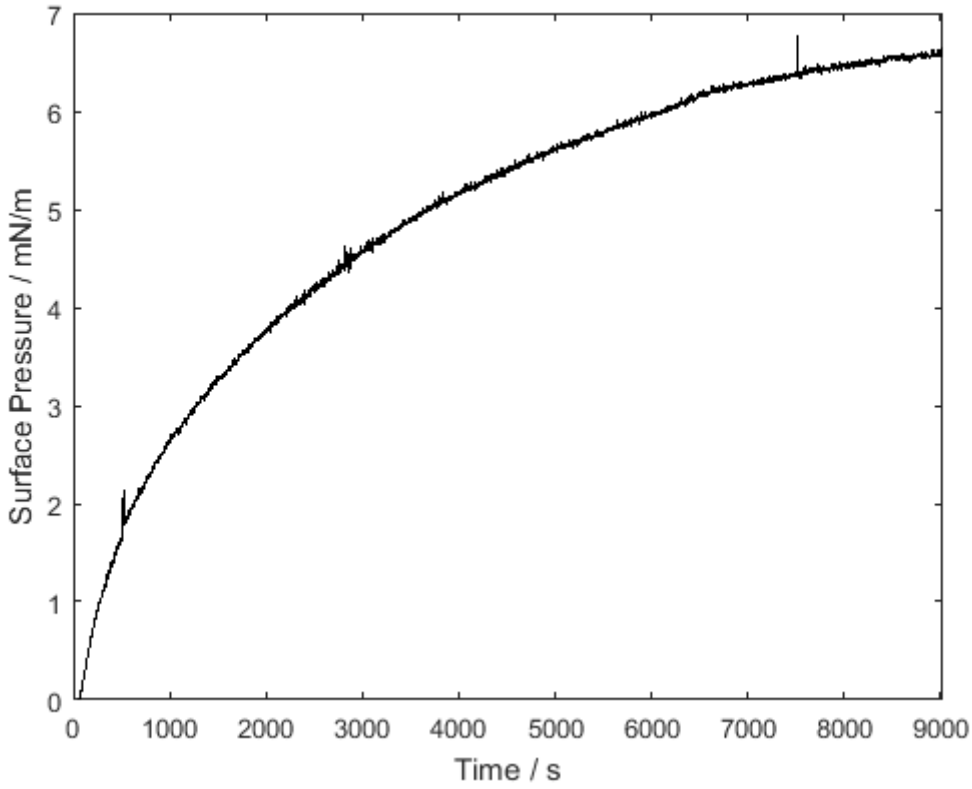

Figure 37 – Surface pressure change for a 15 mM PNP solution over 2.5 hours.

6.1.2 – Short and Long time scale growth

The surface pressure data can be split into two sections, first is an exponential-like curve which gives way to a linear trend. This can be seen more clearly below in Figure *38*. Figure *39* shows the surface

pressure data for three different 15 mM solutions. It can be seen that for a given concentration of PNP, the linear growth rate is the same.

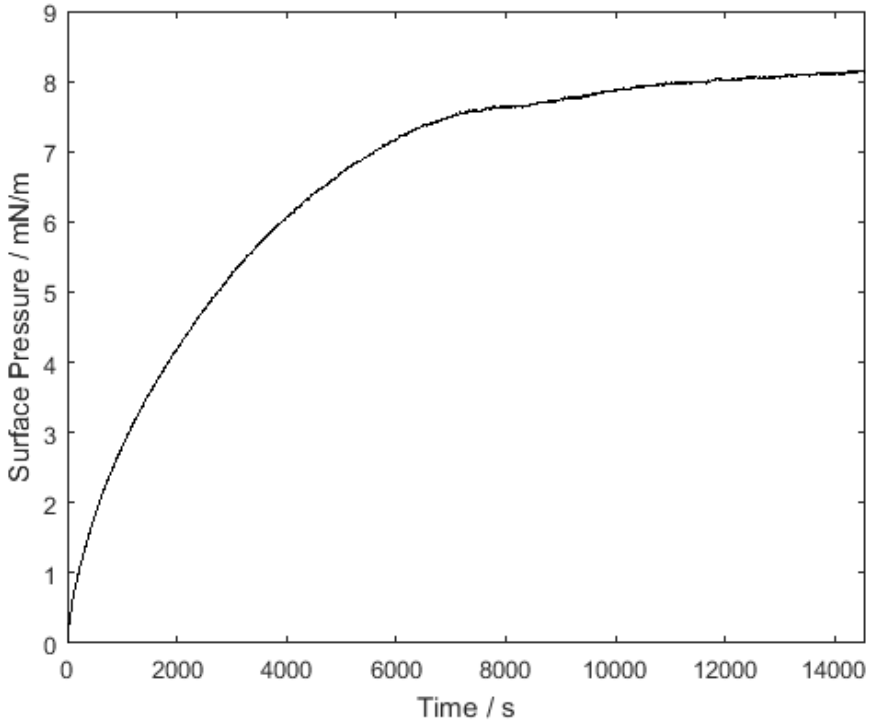

Figure 38 – Surface pressure data for a 70 mM PNP solution which has been sonicated. From 0 to 8000 s, the exponential-like curve is seen, giving way to a linear surface pressure increase after this.

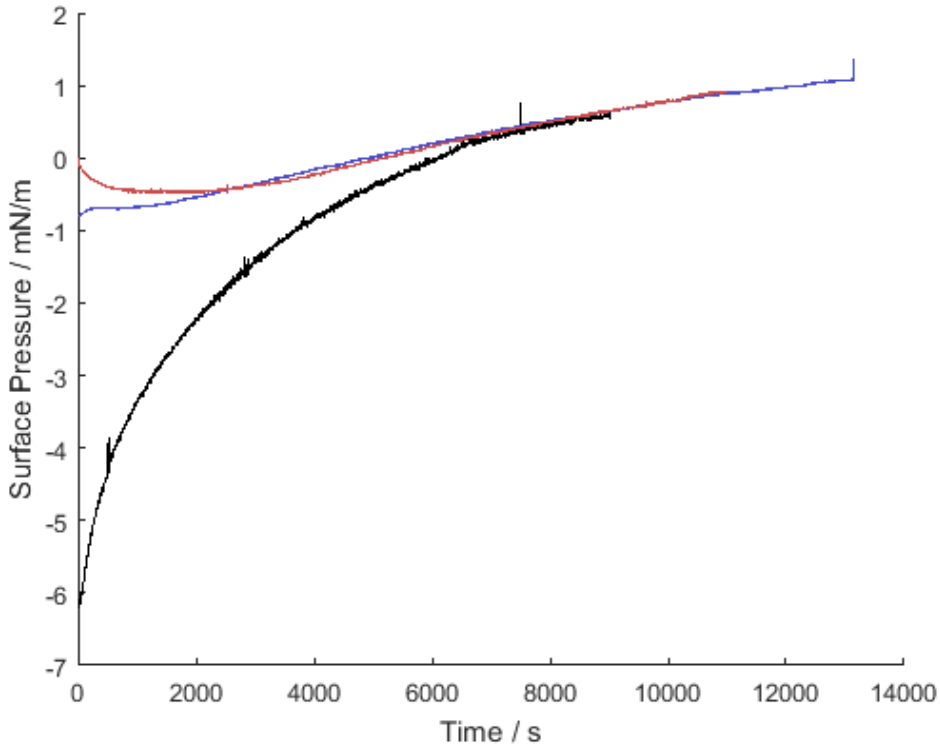

Figure 39 – Three surface pressure data sets trending towards the same growth rate for 15 mM PNP solutions. Black shows the same data as in Figure 37, while the red and blue curves show data sets where the exponential-like growth was not observed due to a preformed structure at the surface before the start of the experiment. The red data set shows an initial decrease in surface pressure due to the solution cooling slightly at the start of the experiment.

6.2 – NIMA Trough Experiments

In order to perform area isotherms on the PNP surface layer, experiments were performed with a NIMA trough with powered barriers. Most of the experimental work was performed over the course of 8 hours and is shown below in Figure *40*. Three area isotherms were collected over the course of the experiment, T0 at the start, T1 after 4.5 hours and T2 after 6 hours. Elasticity measurements were also taken at 5 mN/m and 10 mN/m. At the end of the experiment, the trough was left compressed for 12 hours to equilibrate. The surface pressure values were not reset between different experiments, so the values are all comparable.

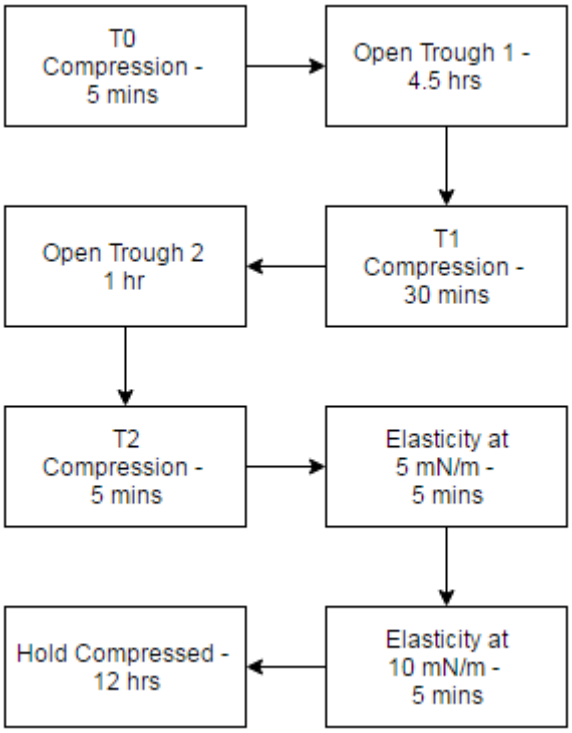

Figure 40 – Flow chart of experimental work for NIMA trough

6.2.1 – Sample Preparation

2.7139 g PNP dissolved in 1.3 L deionised water to make 15 mM solution. The solution was left overnight to fully dissolve. Before use, the solution was stirred as vigorously as possible to break up any structure that may have formed at the surface.

6.2.2 – Open trough

Initial measurements of the surface pressure are shown in Figure *41*. The exponential step cannot be seen in this data, and the rate matches with the linear growth step seen in other experiments, indicating that the surface excess of PNP was already in place immediately after being poured into the trough. This is likely to be due to because of inadequate mixing, due to the large volume of the solution. This growth rate was seen over the course of 6 hours as the experiment progressed, suggesting that this process at the surface is a slow process to complete. The gradient of this line is equal to those shown in Figure *39*, as would be expected for solutions of the same concentration.

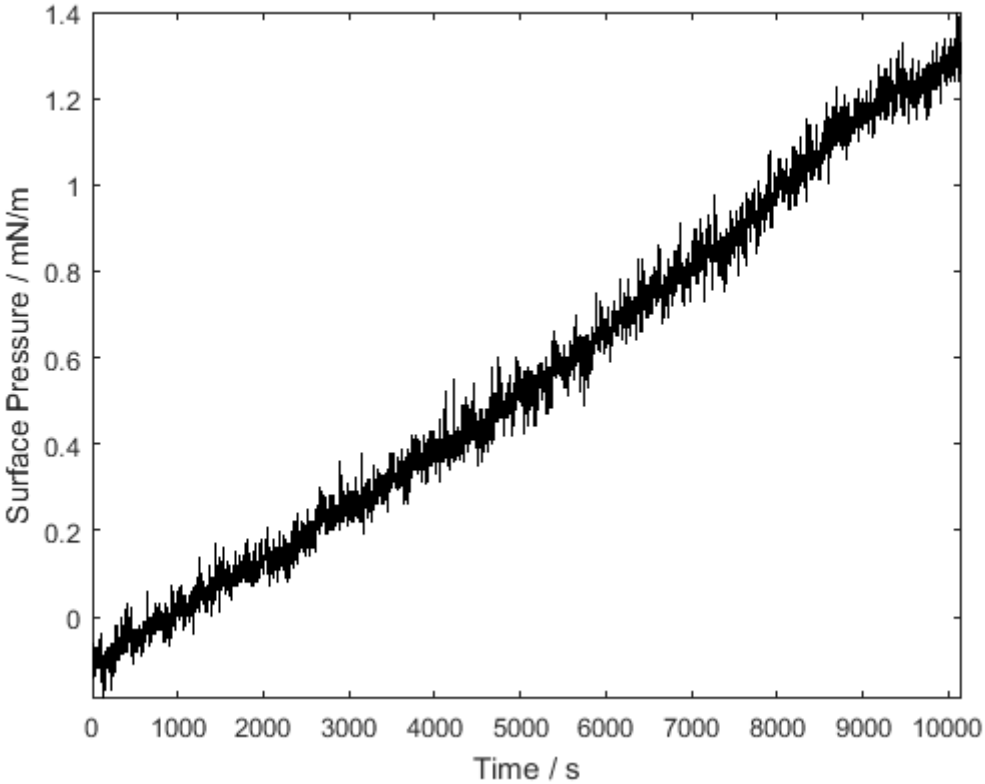

Figure 41 – Surface Pressure data for open trough. The surface pressure is increasing at the same rate as the other 15 mM solutions shown in Figure 39.

6.2.3 – Area Isotherms

Throughout the course of this experiment, three area isotherms were performed. These show the change in compressibility of the surface as the layer nucleates and reorders, as driven by the change in surface pressure. T0 was performed immediately as the isotherm was added to the trough, T1 was performed after four hours, and T2 was performed after six hours. These isotherms consisted of a compression and expansion at a rate of 0.8 cm^2 per second. Due to a software glitch, the barrier did not expand after the compression of the T1 isotherm leading to the layer starting to equilibrate back into the bulk because the surface concentration of PNP was too high. This will be discussed further in section 6.2.4. The isotherms are shown below in Figure *42*.

Two things can be initially seen from these isotherms. First is that at the T0 isotherm, a minimal surface pressure change was seen. This indicates that the initial layer which forms only weakly held at the surface. As the layer is compressed, if the PNP were more strongly bound at the surface; by an enthalpy gain from either its position at the surface, or favourable interactions with other surrounding molecules in the monolayer; a large surface pressure increase would have been seen, as in the T1 and T2 isotherms. Therefore the nucleation and subsequent reorganisation which was seen after the T0 isotherm is responsible for the compressibility of the monolayer. This is consistent with

the findings of Paluch et al.[9], which calculated the enthalpy of adsorption at the surface for PNP was low, however they only observed the initial exponential step and not the further linear step, due to their method of surface tension measurement.

The second observation is the length of time required for the monolayer to fully grow. The T2 isotherm has a higher surface pressure when fully compressed than the T1, indicating that the layer had continued to grow after the T1 isotherm was taken. Therefore after the initial diffusion step, the monolayer took approximately six hours to fully grow, though this must take into account the regrowth that would have occurred after the equilibration which occurred after the T1 isotherm.

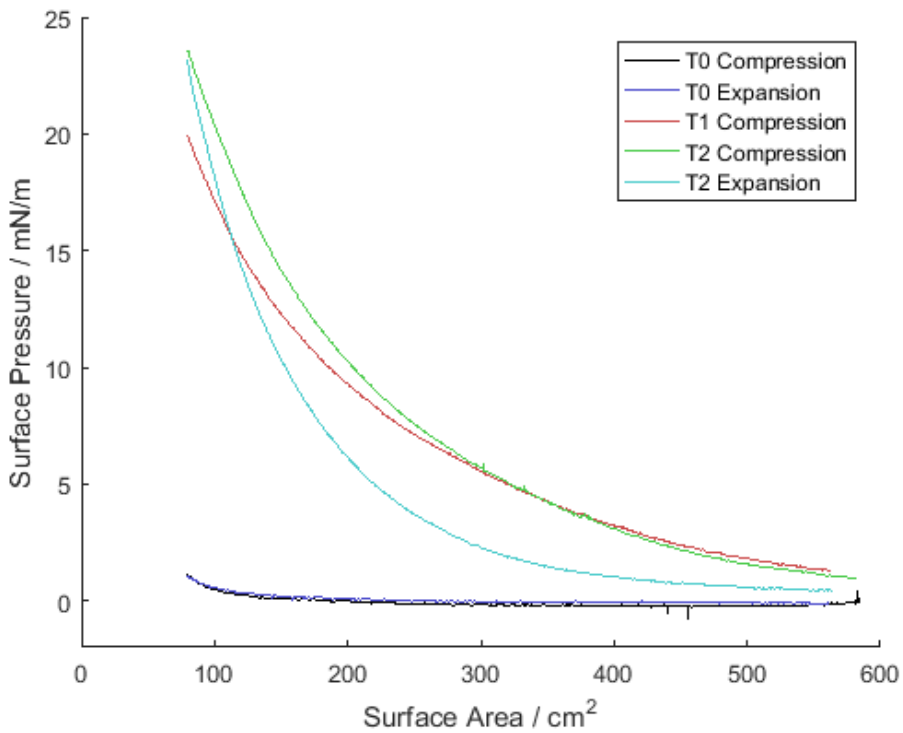

Figure 42 – Area isotherms for 15 mM PNP solution. The black and blue curves show the compression and expansion immediately after being placed in the trough, showing no surface pressure increase. The red curve shows a compression after 4 hours where the expansion did not correctly execute. The green and cyan curves show the compression after 6 hours equilibration in the trough, with the maximum surface pressure change.

6.2.4 – T1 and T3 Isotherm Equilibration

Figure *43* and Figure *44* show the equilibration of the layer after two compressions to 80 cm^2. Figure *43* is the T1 isotherm which shows the compression over the first 10 minutes and then the equilibration over 30 minutes. Figure *44* shows the equilibration of the solution for 12 hours after compression. Both of these data sets show a maximum surface pressure of 20 mN/m, which is much higher than otherwise seen in either trough. This high surface pressure value then equilibrates down

to a lower value, approximately 14 and 12 mN/m respectively. This indicates that the layer which is present upon compression is of a higher concentration than is energetically favourable. The decrease in surface pressure indicates PNP returning to the bulk from the surface layer. Despite the drop in surface pressure, the surface pressure that the surface is tending towards at the end of these experiments is still higher than was otherwise seen in the trough, aside from immediately after compression, indicating that there may be a more organised surface layer at this point which could only easily be made by compression of an ordered monolayer.

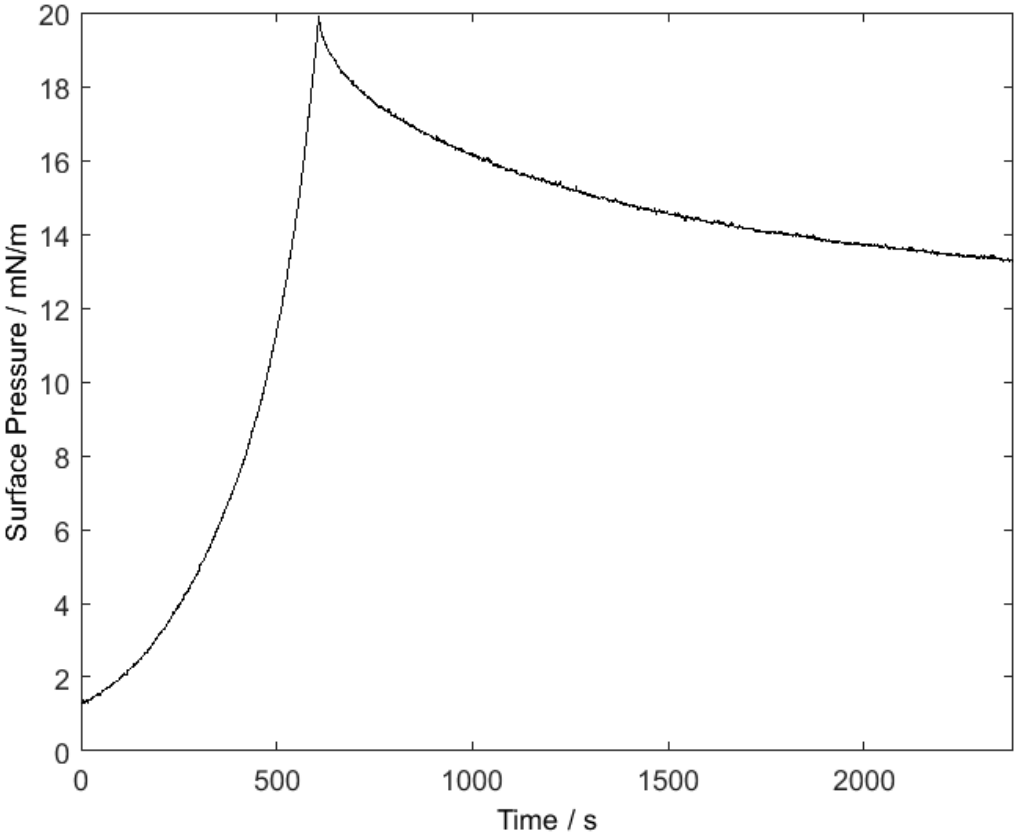

Figure 43 – T1 Compression and subsequent equilibration. This is shown in red in Figure 42. The trough was compressed to 80 cm^2 over the first 600 s shown. Subsequently the expansion did not occur as intended, instead the layer remained compressed, and equilibration of the surface PNP back into the bulk was observed as the surface pressure decreased.

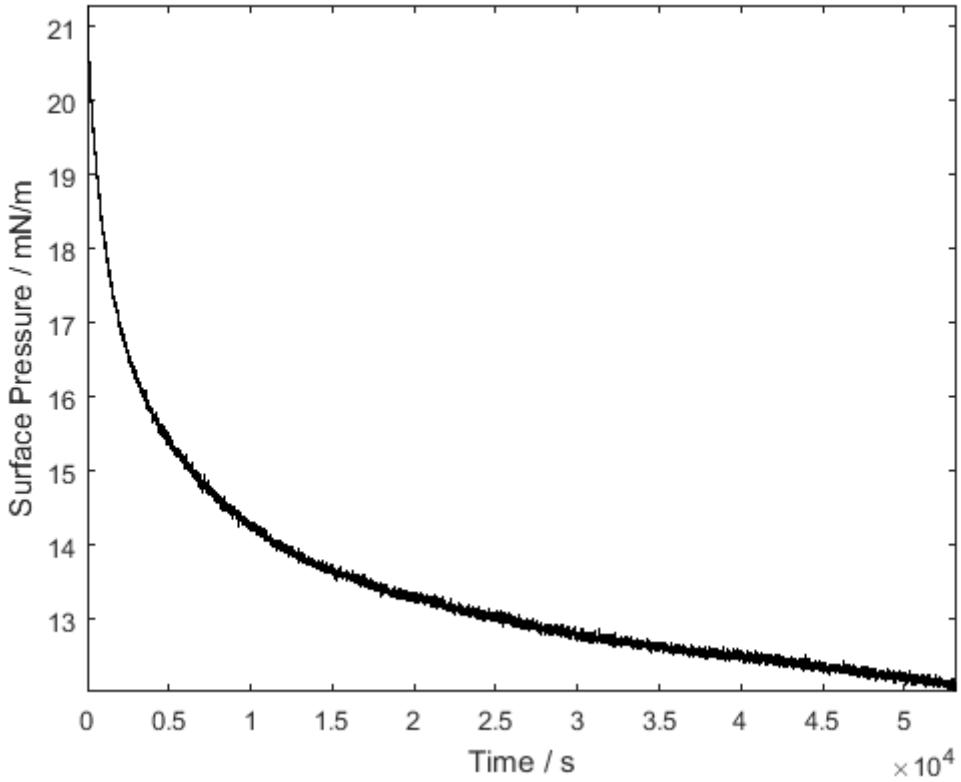

Figure 44 – Surface pressure change over 12 hours of the compressed surface layer. The PNP at the surface is returning to the bulk due to the increased surface concentration after compression.

6.3 – Curve Fitting

6.3.1 – Short Time Scale

In order to better understand the PNP layer which forms at the air/water interface, it is important to fit the data to a model. To this end, the data has been fitted to a time dependent Langmuir model, shown below in equation 6.1, where K' is the rate constant and K_a is the equilibrium constant.

$$\gamma = K'(1 - \exp(-K_a t)) \quad \textbf{(6.1)}$$

Fitting this equation to the data shown in Figure *37* yields the following fit parameters for different time scales shown in Figure *45*. In Figure *45*, for each graph, the experimental data is plotted in blue, the first order Langmuir fit is in red, and the difference between the two is in yellow. Assuming that only the two stages of growth of this layer that were previously discussed, the difference between the experimental and calculated should give the linear growth step.

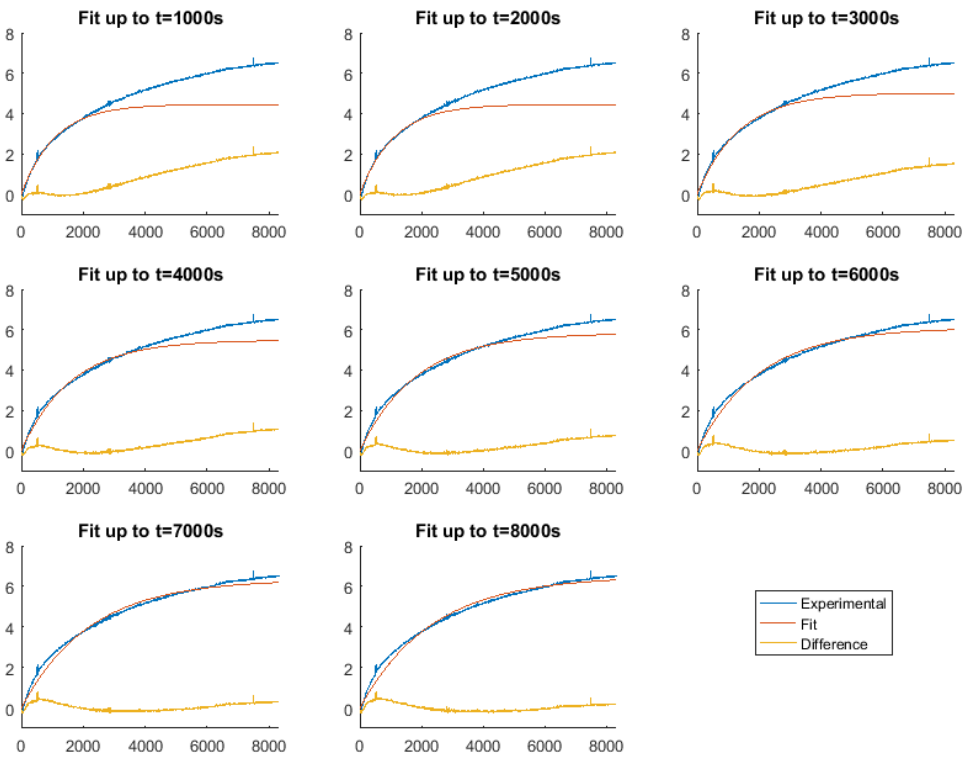

Figure 45 – First order time dependent Langmuir fitting for the 15 mM data shown in Figure 37. Each graph shows the first order Langmuir fit from the start of the experiment through to a different time. The fit is shown in red for each case and the difference between the experimental data and fit is shown in yellow.

Time Fitted (s)	K' (mN/m)	K_a (x 10^{-4} s^{-1})
1000	4.450	9.147
2000	4.445	9.021
3000	5.010	7.305
4000	5.479	6.164
5000	5.823	5.454
6000	6.092	4.956
7000	6.334	4.547
8000	6.495	4.293

Table 4 – Fit parameters for first order time dependent Langmuir

At short time scales, t = 1000, 2000, the fit parameters K' and k_0 are almost identical at 4.45 and 0.0009147 respectively. With longer time for fitting, t = 8000 s, the fit and the data agree well, however applying this fit to longer data sets, considering that it is known that the linear growth continues for several hours shows that only using the first order time dependent Langmuir function does not work on its own.

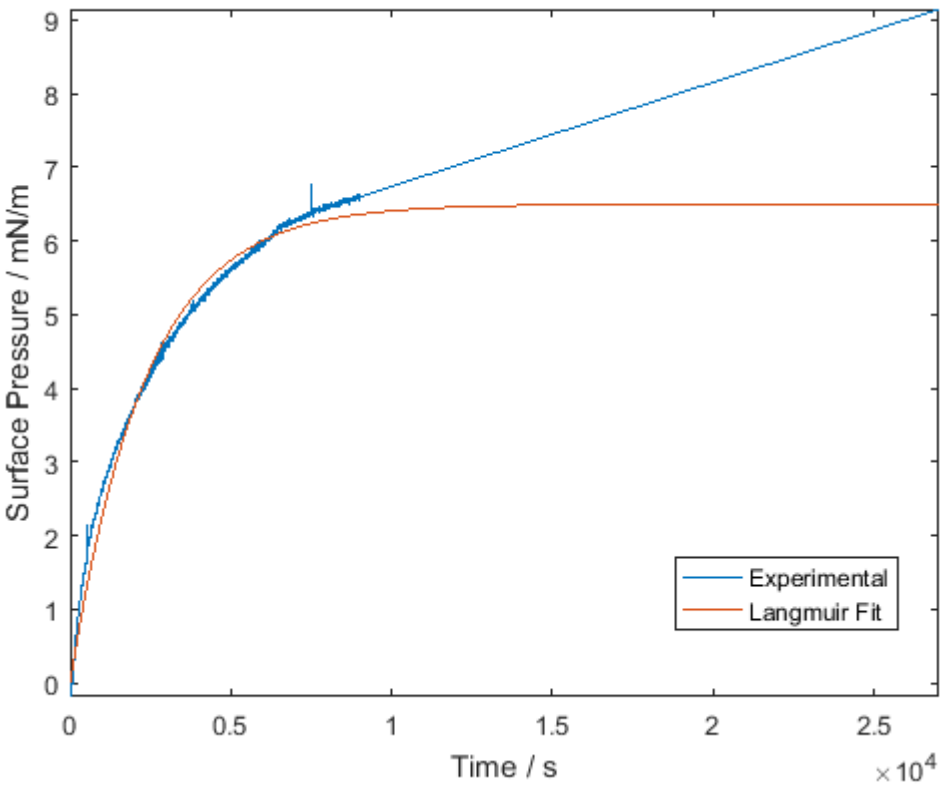

Figure 46 – Deviation between experimental and fit for 15 mM data. Beyond t = 10000 s, the data is generated from the gradient calculated from the data for 15 mM shown in Figure 39 and Figure 41. The first order Langmuir fit does not fit to this long term linear growth, but tends towards 6.5 mN/m.

Taking into account the linear long time scale surface pressure growth, it is possible to build a second model for the surface pressure change. Assuming that the rate of linear growth is dependent on the total surface coverage it can be accounted for using the following statements. The surface coverage can be assumed to be the current surface pressure over the total potential surface pressure change, shown below.

$$\theta = \frac{K'(1 - \exp(-K_a t))}{K'} \quad \textbf{(6.2)}$$

The rate of linear growth will thus be a product of the surface coverage of the solution and the rate constant k_0 of the zero order step, giving the following expression.

$$\gamma = K'(1 - \exp(-K_a t)) + k_0 t(1 - \exp(-K_a t)) \quad \textbf{(6.3)}$$

$$\gamma = (K' + k_0 t) * (1 - \exp(-K_a t)) \quad \textbf{(6.4)}$$

Fitting this to the data, taking into account that the value for k_0 is known from the gradient of past graphs, such as Figure *41* for 15 mM solutions.

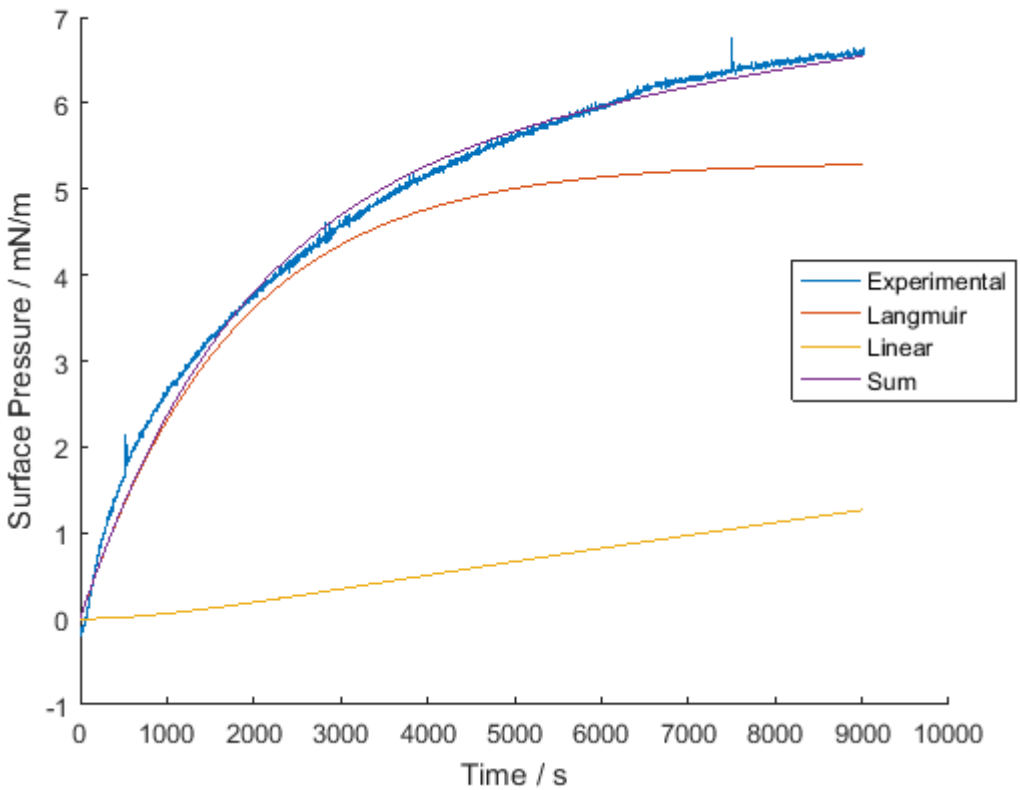

Figure 47 – Combination fit of time dependent Langmuir and zero order with K' = 5.315, k_0 = 0.0001414 and K_a = 0.0005686.

6.3.2 - Nonlinear Long Term Growth

While the long term growth of the layer appears linear, this implies that it will continue indefinitely. This is known to be false, so other fitting terms were applied as were used in past literature of surfactants at the air/water interface[110]. A $t^{1/2}$ fit was applied to the 15 mM data shown in Figure *37* using the following fit. This uses the same first order Langmuir fit to the initial exponential curve, but fits the long term pseudolinear trend to a $t^{1/2}$ dependence. The results of this fit are displayed in Figure *48*. The deviation at long time scales between the calculated linear data and the fit were expected. Since this data is calculated from the gradient of data from other 15 mM solutions, and is linear, at some point the $t^{1/2}$ fit will deviate from this assumed behaviour. This fit has a much smaller Langmuir component, with K' = 3.165 mN/m as opposed to 5.315 mN/m in Figure *47*. This fit is not wholly accurate at long time scales because it tends towards a higher final surface pressure value which is still much too large compared to the experimental values (>40 mN/m). It is possible that a longer recording of the surface pressure would give a more representative data set across the entirety of the growth of the PNP layer which would allow more accurate fitting.

$$\gamma = K'(1 - \exp(-K_a t)) + k_1 t^{1/2}(1 - \exp(-K_a t)) \quad \textbf{(6.5)}$$

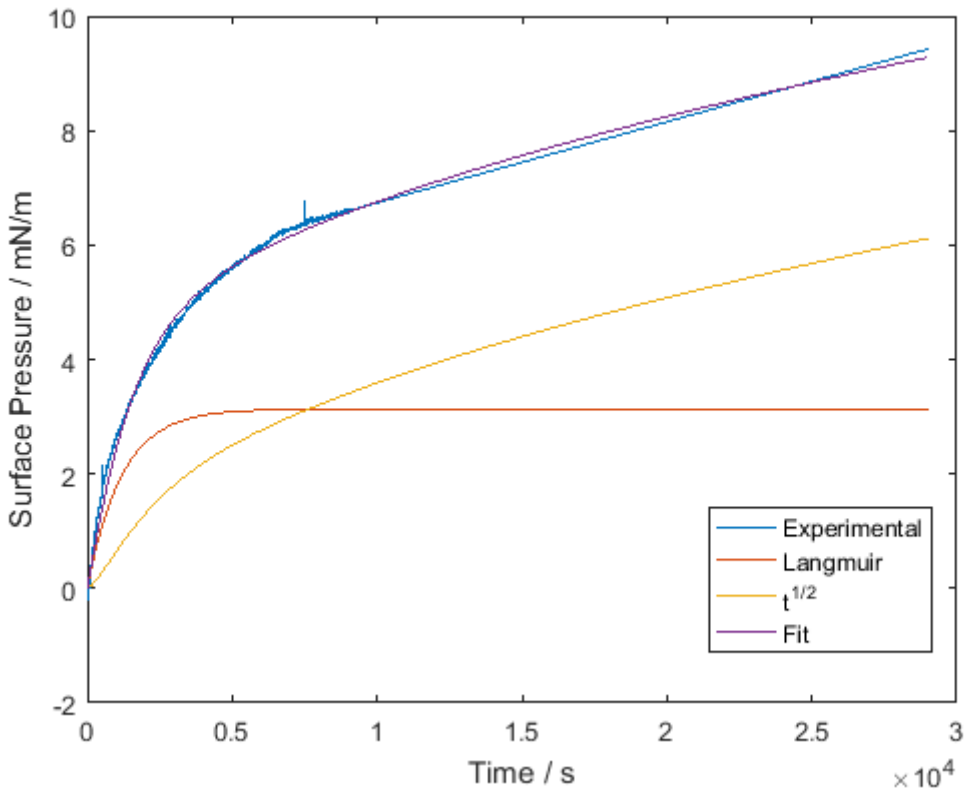

Figure 48 – First order Langmuir and $t^{1/2}$ fit for the surface pressure data shown in Figure 37 with an added linear section calculated from the gradients of the lines shown in Figure 39. K' = 3.165, k_1 = 0.0008325 and K_a = 0.03591.

6.3 – Tensiometry

Tensiometry was used to give absolute values for surface tension as opposed to the surface pressure values which were measured through Langmuir Blodgettry. It was possible to measure many concentrations of PNP due to the low volume of solution which was needed to performed experiments, and the speed that experiments could be run.

6.3.1 – Surface Tension Change by Concentration

Surface tension data was collected for PNP solutions between 2 and 70 mM. Above 60 mM it was increasingly challenging to fully dissolve PNP to get higher concentrations, so the highest concentration used in these experiments was 70 mM, compared to 100 mM used by Paluch et al.[9] All experiments were carried out at the room temperature of the lab, 22°C. Figure *49* contains data from two data sets collected for this work, Cranfield New which were thoroughly stirred before testing, and Cranfield Aged which were not. This figure also contains literature data as well as data collected by researchers at KTH, Stockholm.

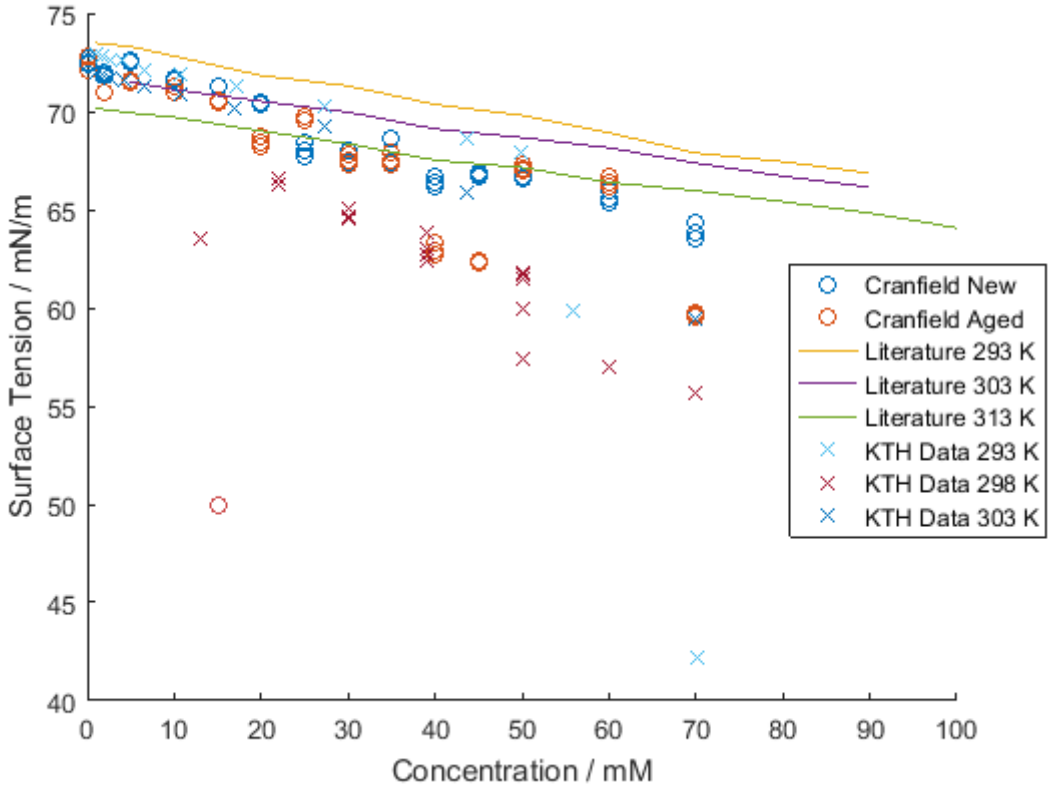

Figure 49 – Combination of surface tension data of PNP from various sources. The three lines represent data collected by Paluch and Filek. The Xs show tensiometry data collected by researchers at KTH and the Os show data collected in this work. Both the KTH data, and data for this work show a greater change in surface tension with respect to concentration than the literature data, and a range of surface tension values can be seen for each concentration.

6.3.2 – PNP Literature Comparison

Comparing the data collected in this project and the literature values available shows some differences. The data collected from this project decreases slightly faster with respect to concentration than the points collected by Paluch and Filek. This is likely because of the method of data collection. In that work, the surface tension was collected by a flowing jet method. This method collected the surface tension over the first second of the surface forming, therefore is likely to be in the time scale which cannot be accessed by tensiometry. It is thus logical that the surface tension values from this method would be higher than those collected by tensiometry since they represent a lower surface concentration.

6.3.3 – Surface Pressure Conversion

Converting the surface tension data shown in Figure *49* into surface pressure for each concentration by taking the difference between each value, and the highest value for the concentration shows the maximum change in surface tension at each concentration.

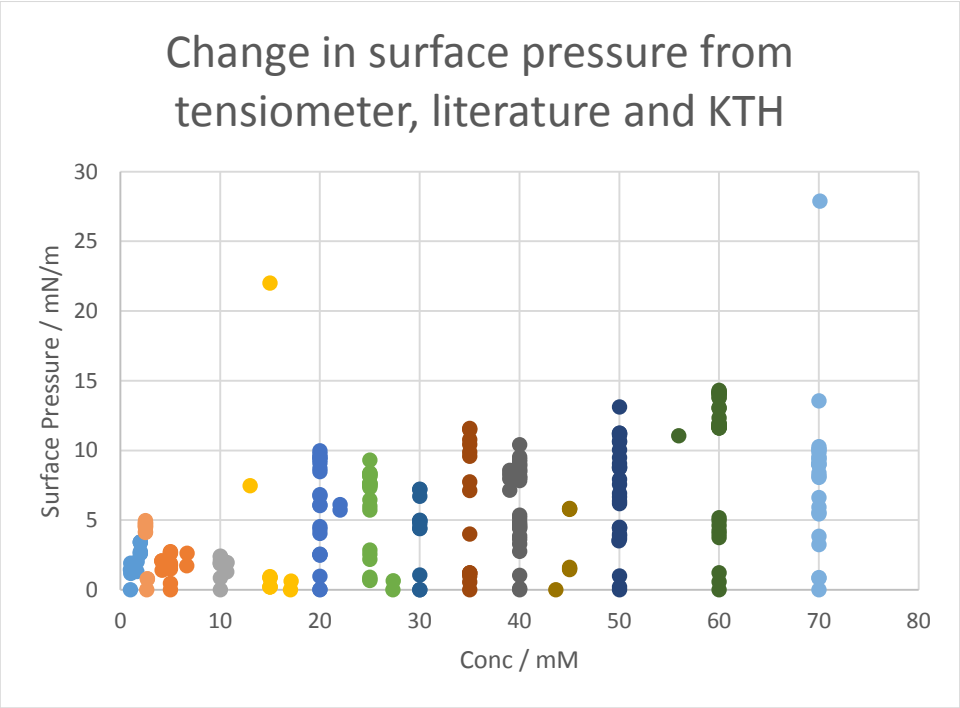

Figure 50 – Surface pressure by concentration for tensiometry calculated from the difference between the highest surface tension value for each concentration, and each other point. The maximum surface pressure seen increases with concentration, though two points with a surface pressure greater than 10 mN/m can be seen for 15 and 70 mM.

Ignoring the two data points of surface pressure greater than 20 mN/m, it can be seen that as the concentration of PNP increases, the maximum surface pressure increases, as expected. This represents a higher equilibrium surface concentration of PNP due to higher bulk concentration. The two data points above 20 mN/m, at 15 and 70 mM correspond to the same surface pressure as was

seen during compression in Langmuir Blodgett experiments. Figure *43* and Figure *44* show the equilibration of the surface layer after compression, tending towards a surface pressure value of 10-12 mN/m. this surface pressure value does not however include the initial time dependent Langmuir growth as depicted in Figure *37*, therefore by adding this surface pressure change of 7 mN/m, the total surface pressure of a 15 mM solution after compression is 17-19 mN/m, a similar value to that shown above.

6.4 – Surface Data Analysis

6.4.1 - Surface Growth Mechanism

Combining the data from literature, the LB trough and from tensiometry gives the following model for the growth of the PNP layer. There are four layers of growth observed, with each subsequent stage decreasing the surface tension by a greater amount with respect to concentration. The first of these steps is the initial surface excess shown by Paluch and Filek. This data shows the highest surface tension value for each concentration. This surface tension drop represents the immediate surface concentration of PNP which forms at the surface. This is shown in red in Figure *51*. Below this is the highest data which was measured in this work by tensiometry, shown below in orange. This is near the start of the Langmuir growth, at the earliest point which is measureable by tensiometry. Below this, in purple is the point at which the Langmuir growth ends, and the linear growth begins. It is worth noting, that it is only beyond this point that the surface layer becomes compressible in an LB trough. The green line shows the lowest values which were observed through tensiometry for a concentration. This level of surface disruption was rare to observe through tensiometry, though seems to be equivalent to a layer which was given time to equilibrate in an LB trough and then compressed, suggesting the highest levels of surface concentration and order at the surface.

Overall this suggests a growth model for the PNP surface layer PNP whereby initially PNP aggregates at the surface according to first order Langmuir kinetics, and then this subsequently undergoes a change which is zero order with respect to time. This is probably a reorganisation of the surface layer which accounts for the very low elasticity of the fully formed layer which was seen in Langmuir Blodgettry. This stops after several hours as the monolayer is fully ordered. At this point it is possible to see a large surface pressure increase upon compression of the monolayer though leaving the layer compressed causes the PNP to move back into the bulk due to the high concentration at the surface.

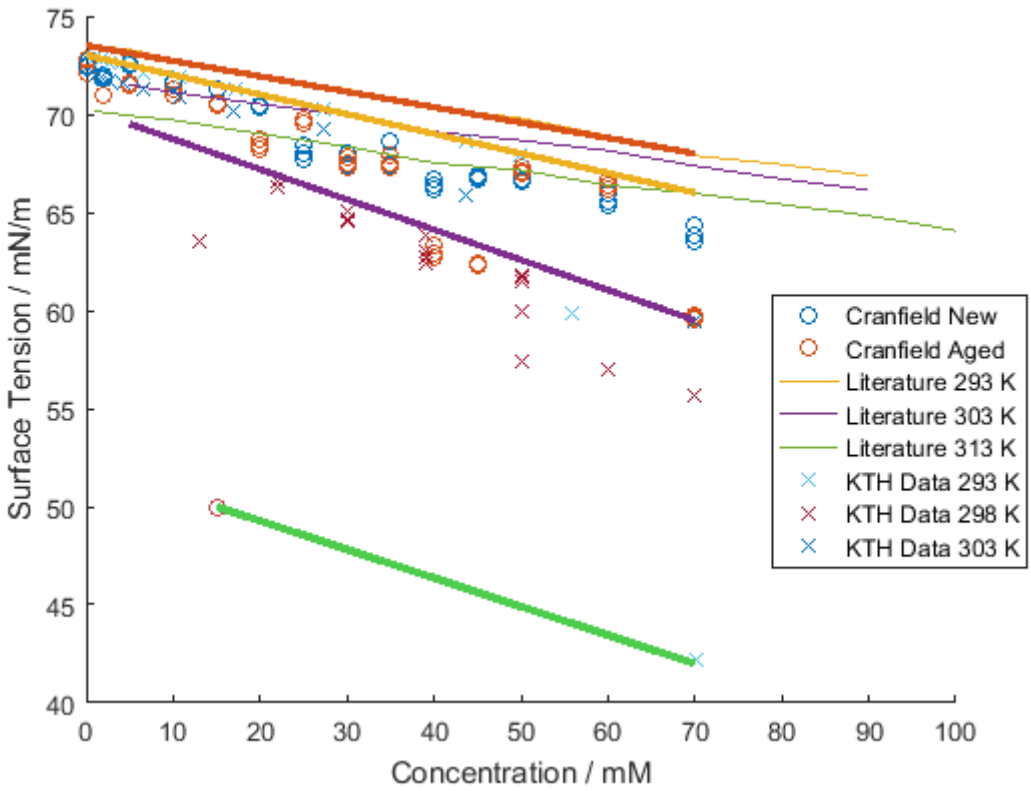

Figure 51 – Some highlighted trends in the surface pressure data as bolder lines in red, orange, purple and green. These represent higher concentrations of PNP at the surface, and greater levels of organisation.

6.4.2 - Micelles and Multilayers

There is no evidence in any of the trough experiments of PNP forming any structures with any surface structure more ordered than a single monolayer. Micelles were also not seen to be forming in the tensiometry experiments. It is understandable that micelles are not forming for PNP, since it is readily soluble in water, it does not need to form aggregates to be energetically supported in the bulk.

6.5 - Conclusions and Further Work

This work set out to study and characterise the surface layer of PNP which forms at the air/water interface through Langmuir Blodgettry and tensiometry. The Langmuir Blodgett experiments which were performed successfully showed the growth of the monolayer over several hours. Through the tensiometry experiments which have also been performed, it can be surmised that the growth seen in the troughs starts with the surface formed as measured by Paluch and Filek, and continues from this point, since it was not found to be possible to measure any surface tension values higher than was reported in their paper for any concentration.

The growth of the layer can be split into two steps, the first, an exponential step which fits to a first order time dependent Langmuir, and the second, a pseudo linear step. The exponential step occurred over approximately one hour, while the linear growth continued for several hours, longer than it was possible to measure in a single experiment. Since it was not possible to measure the full extent of the pseudo linear step, it is not possible to state with any certainty what fit should be applied to it, and while it appears linear over time frame it was measured for, this implies that the surface tension would decrease forever, which it clearly impossible. Further data collection would be useful in this regard, to find the end point of this growth, however extra care would have to be taken to control for factors such as evaporation and temperature change over this long time span.

Additionally, under compression in the trough, it was found that the layer was only compressible after the pseudo linear growth step had begun. Initial area isotherms showed no surface pressure increase on compression, while after several hours, a 20 mN/m surface pressure change was observed upon compression.

The following mechanism has been proposed to account for the growth of the layer. Within the first second of growth, a small surface excess of PNP forms, as measured by Paluch and Filek, this PNP is only weakly bound at the surface. Over the first hour of growth, more PNP moves to the surface, resulting in a surface tension drop of 5-10 mN/m depending on the concentration of PNP. This PNP is still only weakly bound at the surface. From this point, the PNP at the surface undergoes a reorganisation into an ordered structure at the surface. This is seen as the long term pseudo linear surface pressure change. It is only at this stage that the layer becomes compressible due to the PNP being bound more strongly at the interface due to this reorganisation.

In addition to further Langmuir Blodgettry, it would be useful to perform further tensiometry to understand the dependence of concentration on the rate of growth and the maximum drop in surface tension. It would also be worthwhile to conduct a series of simultaneous Langmuir Blodgett and tensiometry experiments on the same solution to confirm the relationship between the growth which was seen in the trough and the different tensiometry values which were measured for each concentration.

Chapter 7 – Air/Solvent Interface Ellipsometry

Ellipsometry is a powerful tool to study thin layers at interfaces. While it is mainly used to characterise thin solid films, some ellipsometry work has been performed on liquids to probe the nature of their surfaces. Early experiments were performed in the 19th century by Jamin and Rayleigh who found that small amounts of p polarised light were reflected at the Brewster angle, compared to the predicted value of 0 from the Fresnel equations[111].

In the 1970s and 1980s, Beaglehole published several papers of the results of more in depth ellipsometric studies of liquid surfaces. An early paper looks at the surface of liquid argon around its triple point and found that its ellipticity matched closely with the theoretical values for a simple liquid[112]. Further work followed with papers looking at other liquids which could be assumed to act as simple liquids, such as carbon tetrachloride[113].

In 1983, Beaglehole discusses the ellipticity of the air/water interface, observing large variations in the recorded values of the ellipticity[111]. This is put down to the difficulty in keeping the interface clean, as well as instrumental issues around performing experiment exactly at the Brewster angle. While there is some variation in the values measured for the ellipticity reported in this paper, they are mostly positive, which indicates a transition of Δ to 0° through the Brewster angle, and this a surface density lower than the bulk.

In 1987, Beaglehole studied an odd phenomenon at the air/water interface, looking at the change in the measured value of the ellipticity when the sample is heated from above and then has the heat source removed[114]. This is attributed to a change in the surface structure of water as the sample returns to equilibrium conditions, however questions remain regarding the effect of dissolved gases on this phenomenon, since it was not observed when these gases were removed.

In 2008, Frey and Greef studied the air/water interface by spectroscopic ellipsometry, along with several other pure solvents[115]. Contrary to past results, they found evidence for a layer of increased density compared to the bulk at the interface. By fixing the angle of incidence just shy of the Brewster angle, and increasing the wavelength, they found that amongst the solvents that they tested, water alone saw a transition of Δ from 180° to 360° through the Brewster angle, which is indicative of a layer with higher density. This is supported by work performed a year later by Stucco and Tauer in 2009 who had similar findings using variable angle spectroscopic ellipsometry[116]. Both of these papers suggest that under certain conditions, water has a layer of higher density than the bulk at the surface, however it is unclear whether this is always true, or what separates these results from past work where this was not found.

The initial work of this chapter aims to perform Brewster angle ellipsometry experiments similar to those performed by Frey and Greef. Since the results from these experiments run counter to previous ellipsometry experiments, it is important to verify that these results can be reliably recorded on the equipment used for this work.

Running parallel to this work, simulations of the water surface were performed, attempting to calculate the values of Ψ and Δ for simulated water surfaces to find a definition of the surface which correlated with the experimental results gained from this work. The simulation package used generated ellipsometry data based on angle of incidence rather than wavelength, as collected by Brewster angle ellipsometry, so variable angle spectroscopic ellipsometry experiments of the air/water interface were planned after the efficacy of Brewster angle ellipsometry was tested on the interface in order to provide data which was easily comparable to the simulated data.

Past ellipsometry work at the air/water interface has focussed only on pure water. As a possible explanation for the differences between the various existing literature data, the final experimental aim of this work was to test how the purity of water effected the measured values of the ellipsometric constants. To this end, four purities of water were tested, from ultrapure through to tap water. The ultrapure water was also tested with the addition of several ionic impurities at millimolar concentrations to study how they effected the values of Δ recorded through the Brewster angle.

7.1 Water Ellipsometry Data

7.1.1 - 70° AOI

Initial experiments aimed to provide a simple test of the efficacy and repeatability of ellipsometry on the air/water interface. A wavelength range of 200-800 nm was chosen, at a 70° angle of incidence to see if deionised water gave good, consistent data, considering the low signal level which was recorded compared to conventional, solid samples. Plots of the Ψ and Δ for four data sets are shown in Figure *52*.

The values for Ψ measured in these experiments was very consistent from 200-400 nm, then diverges slightly over the rest of the spectrum. The spike at approximately 320 nm in the red data set, is caused by the ellipsometer changing between two different optical filters. The data for Δ is consistent through all of the data sets. Since the AOI is beyond the Brewster angle for water (approximately 53° across this wavelength range), the Δ stays at 360°. At higher wavelengths, above 680 nm, there are some data points where 0°<Δ<1°, however since Δ is the phase difference

between the s and p polarised light, it can easily be seen that 0° = 360°. Therefore Δ moving from 359.5° to 0.5° is only a shift of 1°.

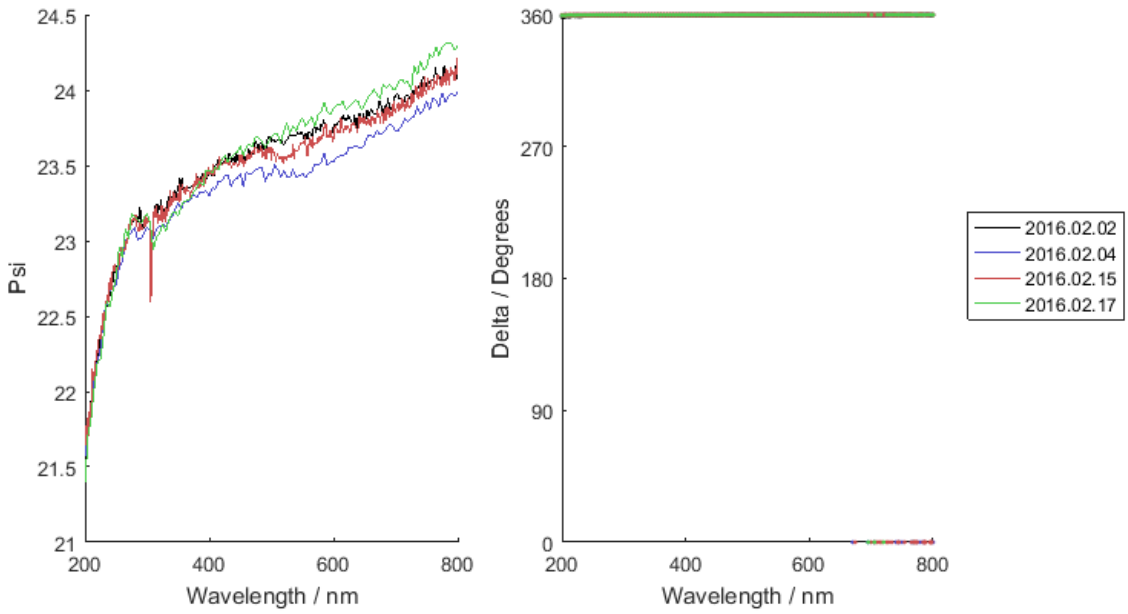

Figure 52 – Four data sets for Ψ (left) and Δ (right) for deionised water at a 70° angle of incidence.

7.1.2 - Brewster Angle Ellipsometry

With the success of the experiment above, the next step was made to use ellipsometry to study the air/solvent interface as the AOI passes through the Brewster angle to gain insight on the density of the air/water interface through the change in Δ. This was initially done in the same method as performed by Greef and Frey in 2008[115]. This was done by setting the ellipsometer at an angle just below the Brewster angle, 52.9° for water at 200 nm, and increasing the wavelength. Since the Brewster angle of a material changes with wavelength due to dispersion, increasing the wavelength to 800 nm allows the transition through the Brewster angle to be seen while keeping the angle of incidence the same. Therefore as the wavelength increases, Ψ passes through a minimum close to 0 and Δ changes from 180° to either 0° or 360° depending on the sample. This can be seen below in Figure *53*.

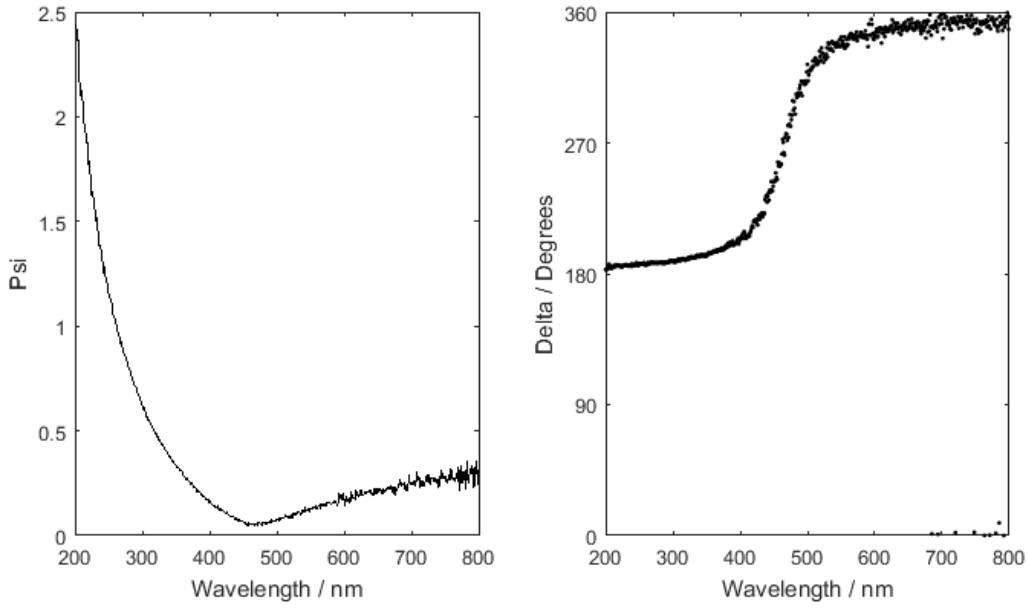

Figure 53 – Ψ (left) and Δ (right) data for Brewster Angle Ellipsometry of deionised water. The angle of incidence was set at 52.9° and the wavelength was varied from 200 to 800 nm.

As expected when passing through the Brewster angle, the values for Ψ pass close to 0, but do not reach it. This happens because Ψ is the ratio between p and s polarised light and while, theoretically the amount of p polarised light reflected at the Brewster angle should be 0. A nonzero value of the extinction coefficient however will cause the some level of reflection of p polarised light at the Brewster angle, so a Ψ of 0 is never practically observed.

As an ellipsometry experiment passes through the Brewster angle, Δ transitions by 180°, usually from 180° to either 0° or 360°. This gives valuable insight into the thickness and density of the surface layer of the sample. The speed and direction of the transition, from 180° to either 0° or 360° can be interpreted to the give a surface density profile of the sample. A change of 180° down to 0 indicates a surface region of lower density than the bulk of the reflecting medium, while a change up to 360° indicates the opposite. An immediate transition indicates that there is no measureable surface layer.

It should also be noted that this experiment is highly sensitive to the angle of incidence. In Figure *54*, multiple data sets have been plotted, with varying angles of incidence. The Brewster angle shifts to a lower wavelength at higher angles, since the experiment starts closer to the Brewster angle for that wavelength.

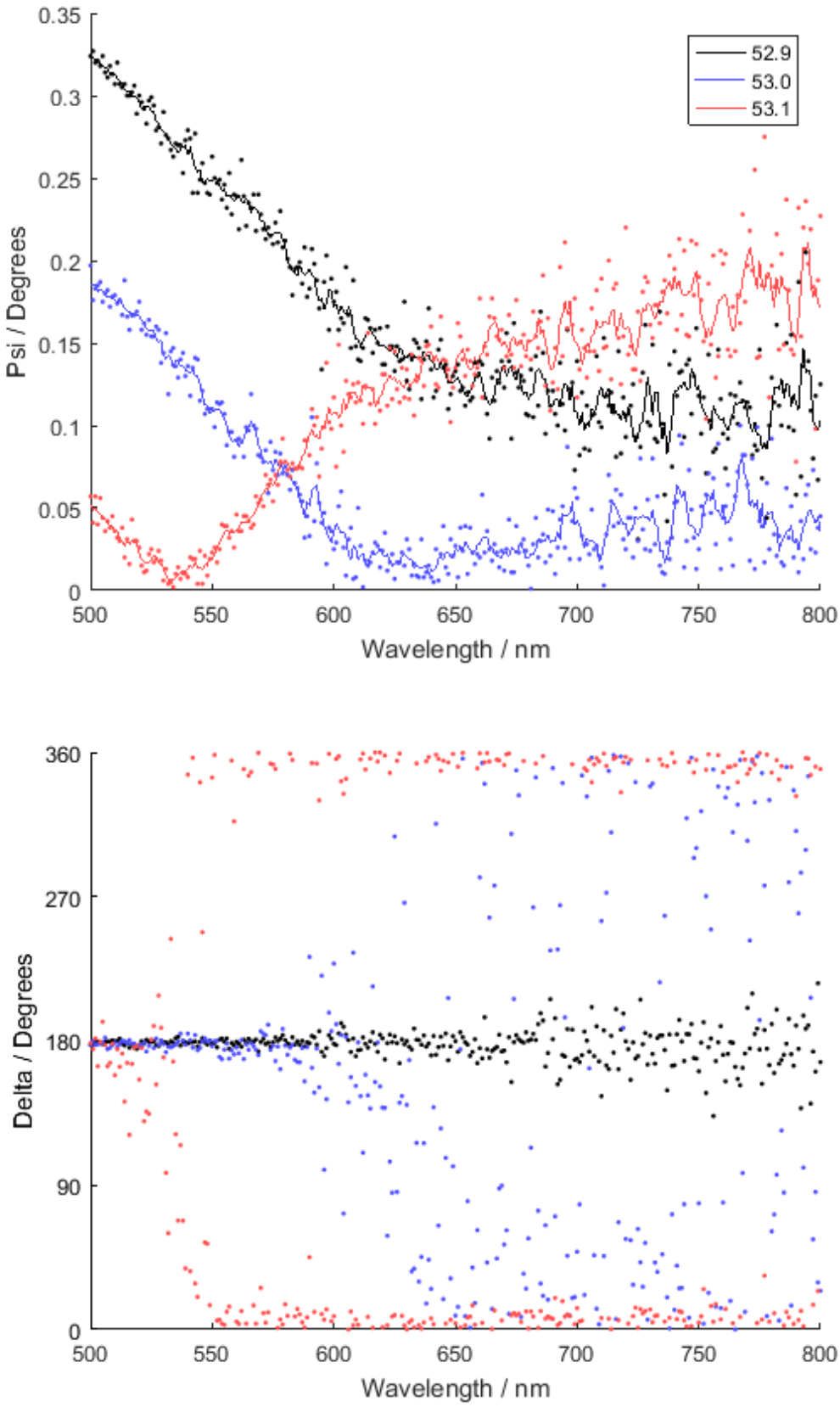

Figure 54 – Ψ (top) and Δ (bottom) data for Brewster Angle Ellipsometry at different angles of incidence for deionised water. Ψ is plotted as a scatter plot for each data set, with a moving average of 5 points plotted as a solid line to highlight the trend. The maximum values of Ψ are less than in Figure 53 due to the proximity to the Brewster angle, but the noise levels within the data are equivalent.

7.1.3 – Change in Δ in Brewster Angle Ellipsometry

It can be beneficial to depict Δ with a polar plot, as shown below in Figure *55*. This shows the change in Δ as the wavelength increase with a more representative axis for Δ. This plot depicts 0° and 360° as the same, which is logical for the phase difference between two light sources, a 360° phase difference represents exactly one wavelength difference, which puts the two sources back in phase. As a result, this plot also shows the noise around 0°/360° much more accurately than a large jump, as shown beyond the Brewster angle in Figure *54*.

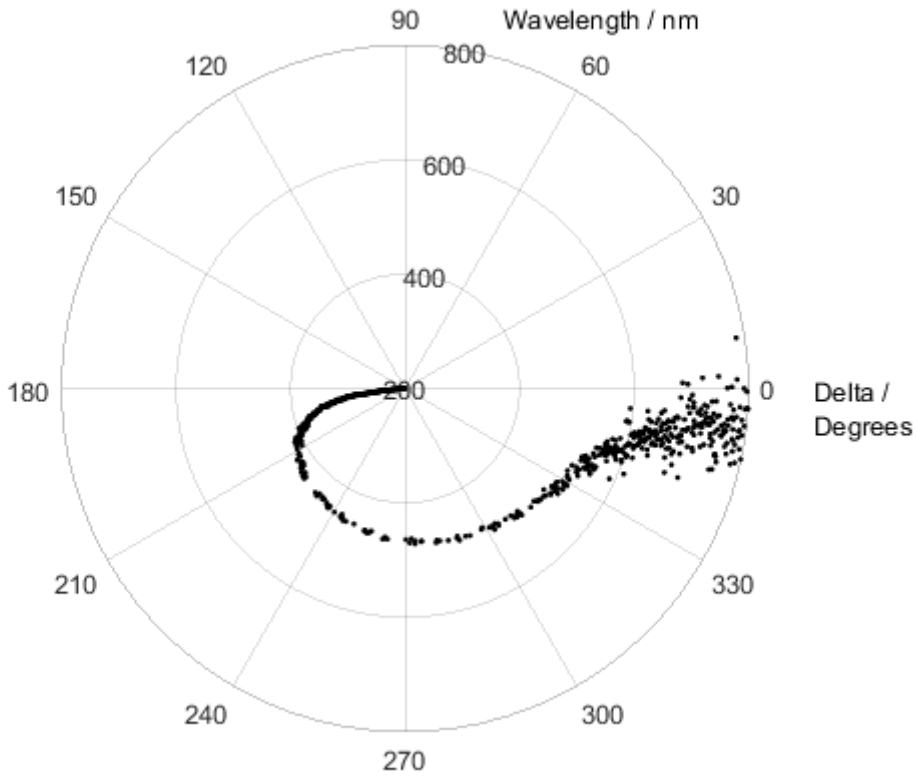

Figure 55 – Polar plot of Δ of water at 52.9° angle of incidence. Wavelength is displayed on the radius of the plot, and Δ is displayed around the edge of the circle. Since Δ is expressed as an angle, it can be seen that 0° = 360°.

As the wavelength increases, and passes through the Brewster angle, Δ goes towards either 0° or 360°, in the case of Figure *55* to 360°, as would be expected for water. As this happens there is a degree of noise within the data, which increases at higher wavelengths. This is likely caused by the low signal strength, along with fluctuations in the sample caused by capillary waves. Water reflects much less light than common, solid ellipsometry samples, and as the experiment moves through the Brewster angle, the signal of the p polarised light almost reaches zero. This could cause some inaccuracy in measuring Δ, the phase difference between the s and p polarised light. Movement at

the surface could also cause fluctuations in Δ, as the surface tilts slightly, it would cause a slight change in the effective angle of incidence of the light, which would change the value of Ψ and Δ measured around the Brewster angle.

7.1.4 – Variance in Delta Data for Water

It is expected that as the wavelength increases, and the experiment passes through the Brewster angle, Δ will transition to either 0° or 360°, as seen in Figure *55*. However, it can be seen in Figure *54* that some data sets appear to show Δ moving in both directions, to 0° and 360°. This is reproduced below in Figure *56* as a polar plot. As will be discussed later, it is not uncommon for data sets to transition down to 0°, and a variety of reasons for this have been found. It is uncommon however to see data where the value for Δ travels in both directions. This is strange because it implies that the 180° phase transition is at the Brewster angle is occurring in both directions to 0° and 360°.

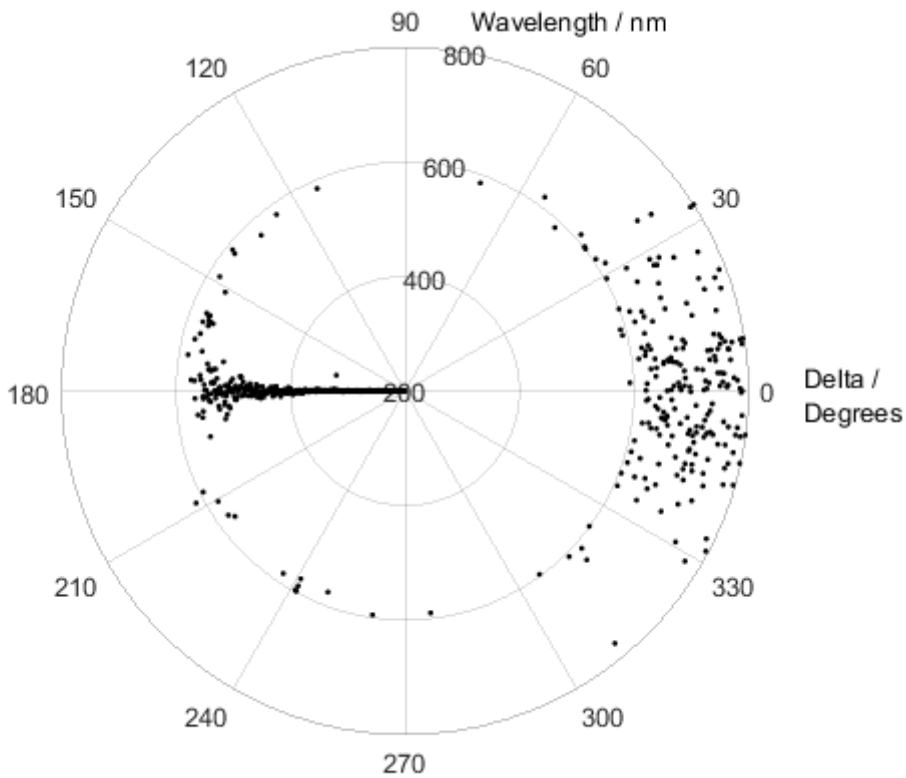

Figure 56 – Δ of deionised water showing a transition to both 0° and 360° at a recorded angle of incidence of 53.1°.

7.1.5 - Variable Angle Spectroscopic Ellipsometry

Varying the wavelength to pass through the Brewster angle has proven a useful tool to study Ψ and Δ, however it is also possible to vary the angle of the experiment instead, and pass through the

Brewster angle by this method to make similar measurements. This has the advantage of being the same measurement which is calculated by the simulations which will be discussed in section 7.5, allowing a more direct comparison than the Brewster angle ellipsometry. Also for this reason, these variable angle experiments have been run at 514.5 nm, which is the wavelength that has been parametrised in the simulation package being used. Further to this, it was found that taking multiple wavelength readings at the same angle did not add significantly to the length of the experiment, but by having multiple data points, issues such as noise were much easier to see within a data set. Therefore, for the experiments discussed hereon in, the wavelength range of 504.5 – 524.5 nm was used at a resolution of 5 nm, giving five data points per angle.

The first variable angle experiment ran over a wide angle range to test the method, 40° - 70°, 1° resolution with deionised water. The data for Ψ and Δ at 514.5 nm is shown in Figure *57*. Ψ passes through 0 and Δ transitions from 180° to 360°, as in the Brewster angle ellipsometry experiments, however the transition is much sharper and there is no noise in the data. This can be attributed to the much lower resolution of this experiment and the greater distance from the Brewster angle for most of this data, giving more intense signals.

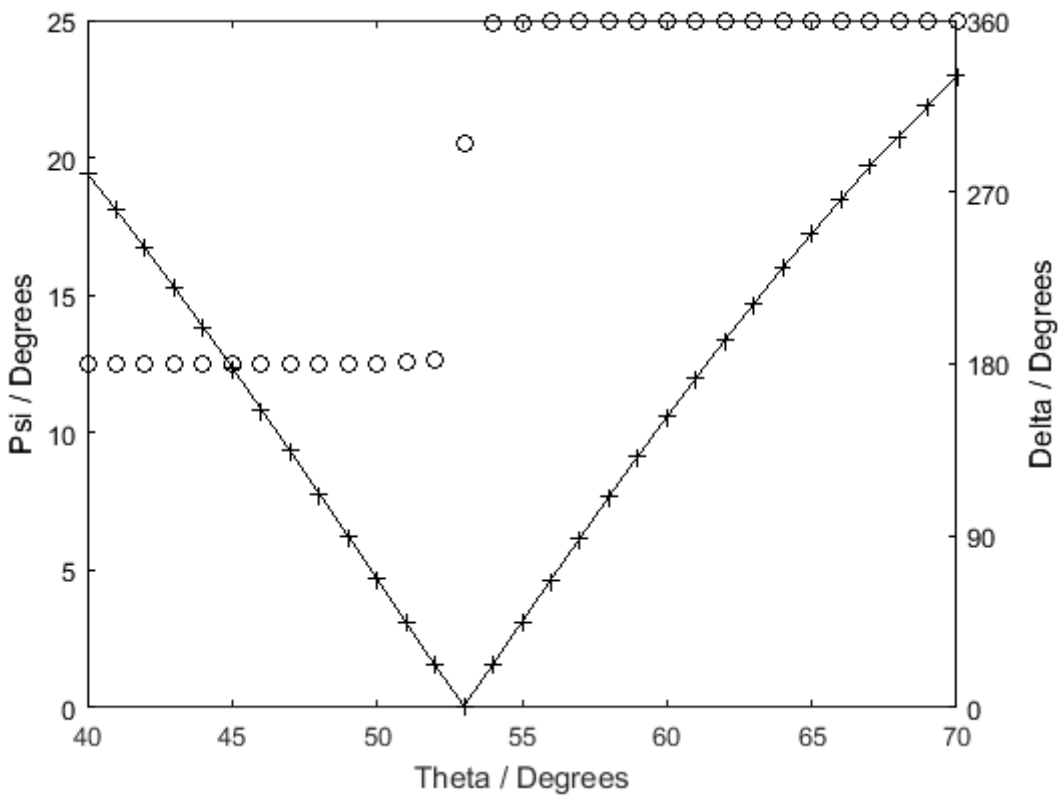

Figure 57 – Variable angle spectroscopic ellipsometry data of deionised water. Ψ is plotted as a solid line with + symbols denoting the data points. Δ points are plotted as circles. The Brewster angle is observed at 53°. Δ transitions from 180° to 360°.

7.1.6 – High Resolution Variable Angle Spectroscopic Ellipsometry

While the data in Figure *57* shows that varying the angle can see the same transition seen in Brewster angle ellipsometry, the resolution must be increased to see any definition in the transition. Subsequent experiments therefore focussed around the Brewster angle, at approximately ±1°. The ellipsometer was capable of moving accurately in increments of 0.1°, as evidenced by the reliability of the measurements of Ψ seen in Figure *58*.

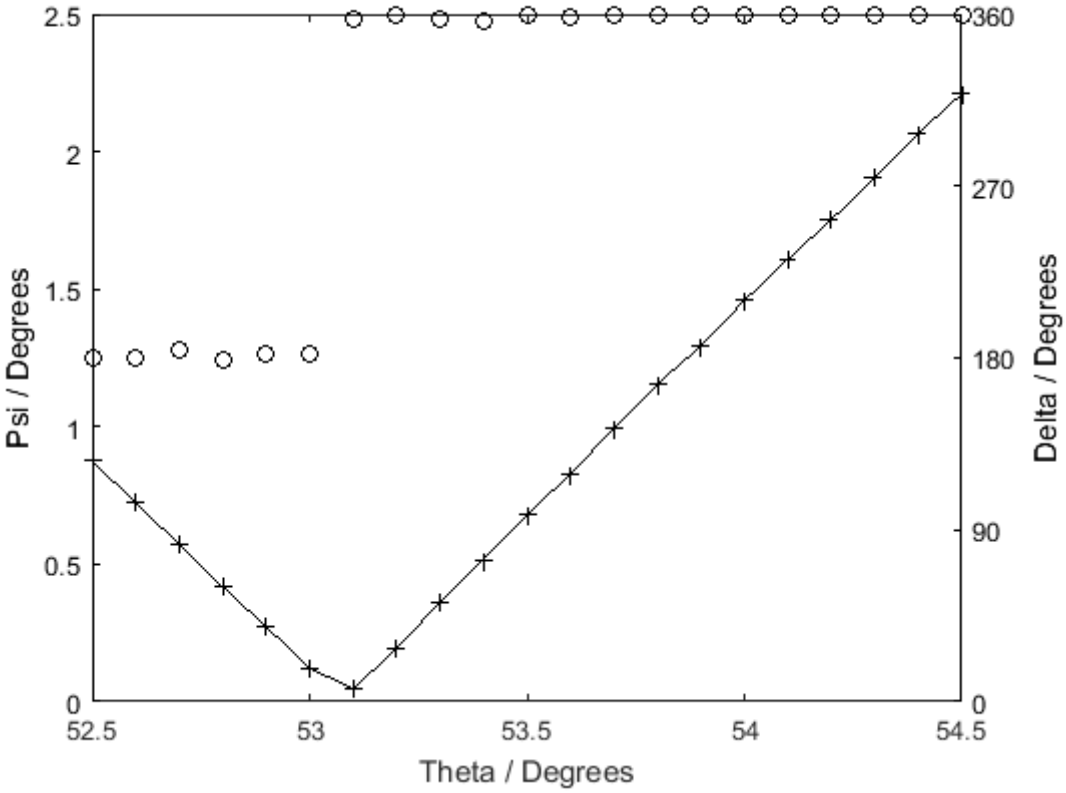

Figure 58 – High resolution variable angle spectroscopic ellipsometry data for deionised water. Ψ is plotted as a solid line with + symbols denoting the data points. Δ points are plotted as circles. The transition through the Brewster angle can be seen with Δ going from 0° to 360°.

As discussed earlier in section 3.4.3, an issue was identified with the accuracy of the angle of the arms of the ellipsometer. From here on the corrections that were discussed there have been applied to ensure that the correct angle is being displayed in the value for theta. This is only accurate to approximately ±0.05 degrees, so slight differences in the angle between experiments should not be treated as real.

Further evidence of the consistency of Ψ is shown in Figure *59*. Three data sets for deionised water have been plotted for Ψ and Δ. The values of Ψ on either side of the Brewster angle are consistent with one another, and show very little noise. At the Brewster angle the data for Ψ appears different for the data set plotted in black compared to the other two sets, however this is merely that the black data set has a data point almost exactly at the Brewster angle, while the other two sets have points on either side causing the tip to appear blunted. There is also a difference in Δ between the black data set and the other two data sets shown. The black set has a more sudden transition from 180° to 360° than the other sets. All three sets have Δ going to 360°, which suggests that there is a higher density surface layer, however the sharper transition suggests that the density increase is less pronounced for the black data set than the others. If this is real, then this suggests that the water surface layer is variable depending on the conditions even when dealing with high purity samples, so changes in temperature or slight impurities could be the cause of these differences. As stated above, the slight horizontal shift between the data sets is not real, merely the result of the angle drift of the ellipsometer and the correction which has been applied.

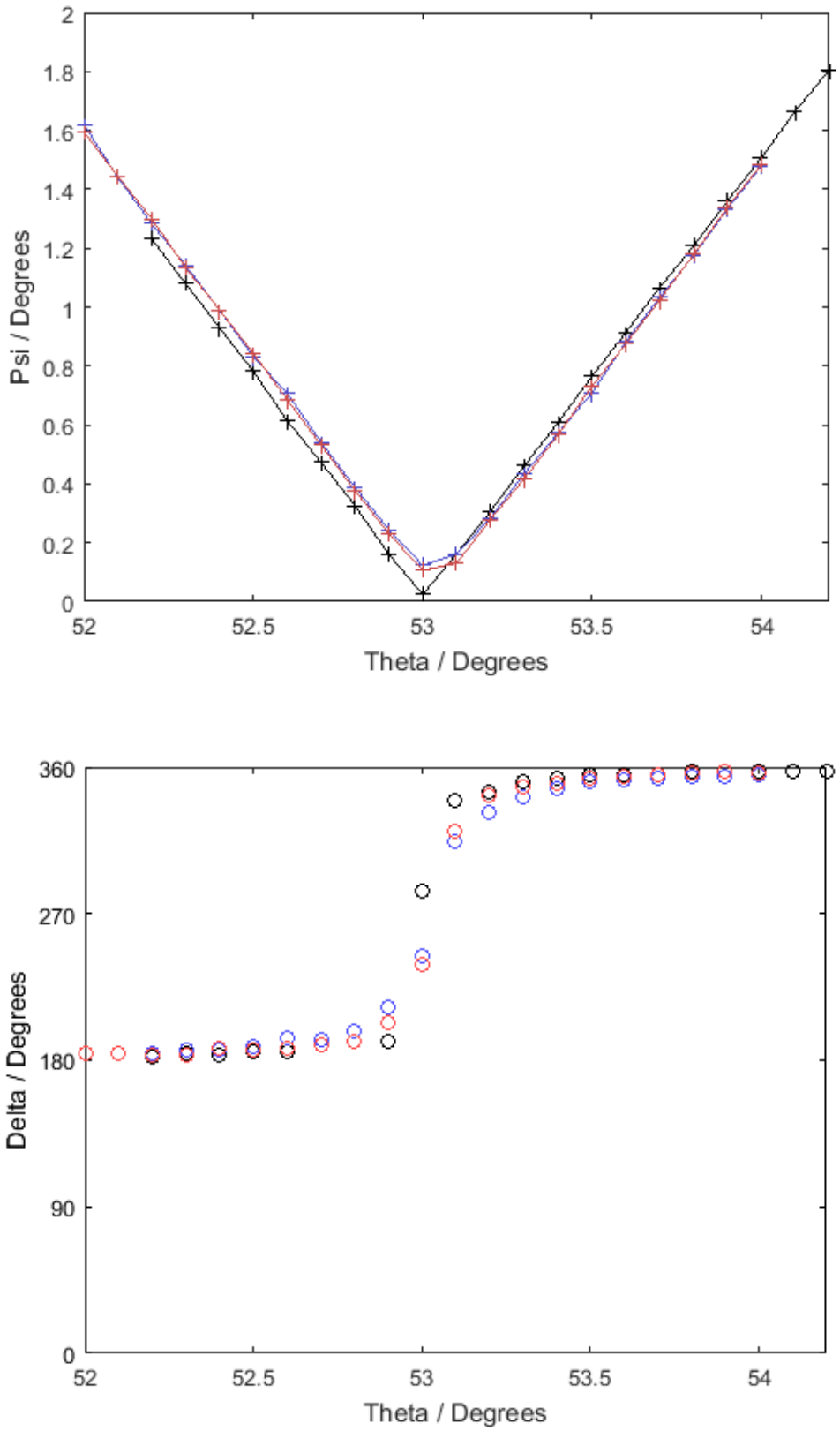

Figure 59 – Variable angle spectroscopic ellipsometry data for deionised water. The top figure shows Ψ data and the bottom figure shows Δ. Three data sets are plotted in different colours: black, blue, and red. Each data set was collected under the same conditions, each two days apart. All three data sets show Δ transition to 360°. The data sets in red and blue are near identical, while the black data set is slightly offset. This is likely caused by the systematic inaccuracy of the angle of incidence.

Figure *60* shows two data sets for deionised water which have radically different Δ data. The values for Ψ are almost identical between the two sets, however while the black data set has Δ rise to 360°, the blue data set decreases to 0°. Both data sets have a quick transition through the Brewster angle suggesting that neither has an especially different surface environment to the bulk, however this implies the data set in black has a slight density increase at the surface which does not appear to be true for the blue set.

Figure *61* shows two variable angle data sets for deionised water, one of which shows notably different data for both Ψ and Δ. The transition through the Brewster angle in this data set is much slower than was normally observed, occurring over an angle of incidence range of 1° as opposed to other data sets where this ordinarily took <0.5° to occur. The recorded values for Ψ in this data set do not drop below a value of 0.4, which is much higher than was otherwise observed. A nonzero value of Ψ through the Brewster angle indicates a nonzero extinction coefficient, suggesting that this sample was not as transparent to the incident light as other deionised water. The Δ transition, while going to 360°, is much slower than in other data sets.

Further testing showed that when the water surface was contaminated with dust, the Δ transitioned to 0° rather than 360°, and very small impurities within the solutions could cause changes in the recorded values of Δ. This will be discussed further in section 7.3. It is probable that one of these factors caused the differences which can be seen in Figure *60* and Figure *61*, however it is also possible that this variation within what spectroscopic ellipsometry can observe for deionised water is real.

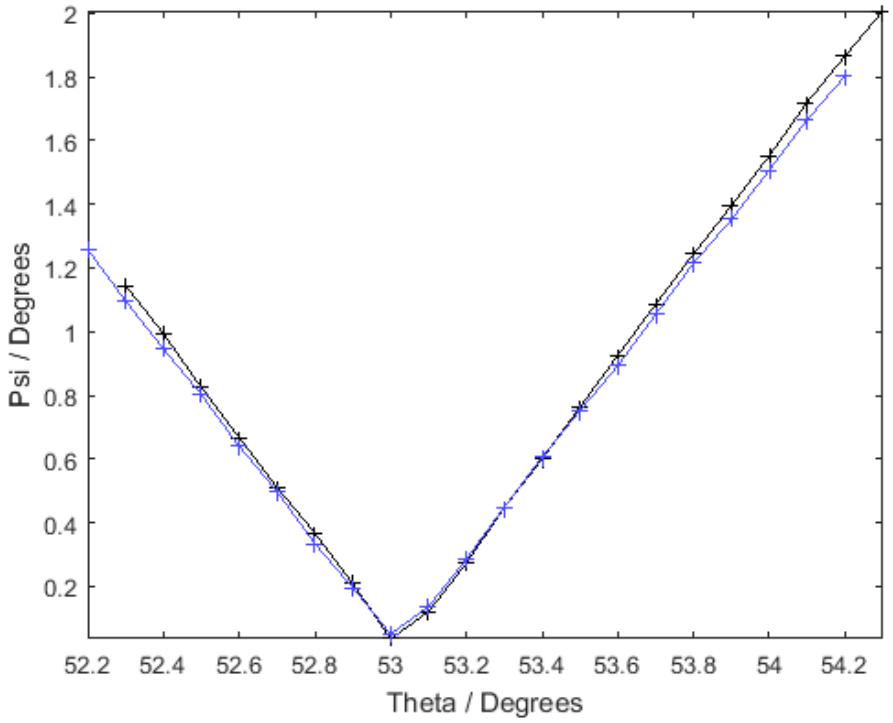

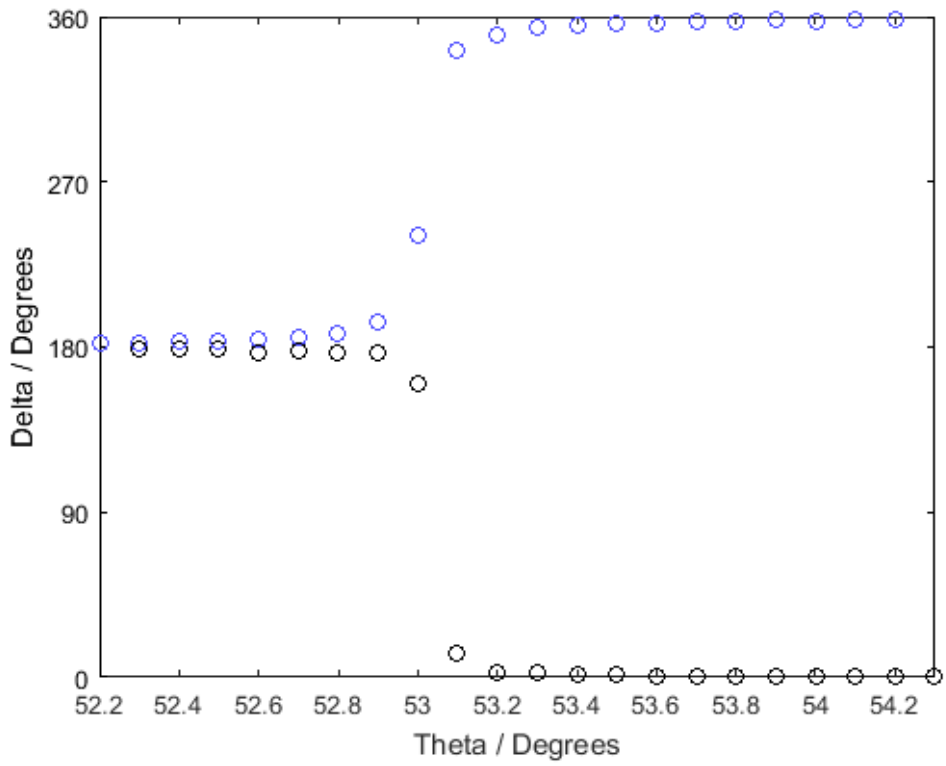

Figure 60 – Variable angle spectroscopic ellipsometry data for two samples of deionised water. Both data sets show near identical values of Ψ, while Δ transitions to 360° for one sample, and 0° for the other.

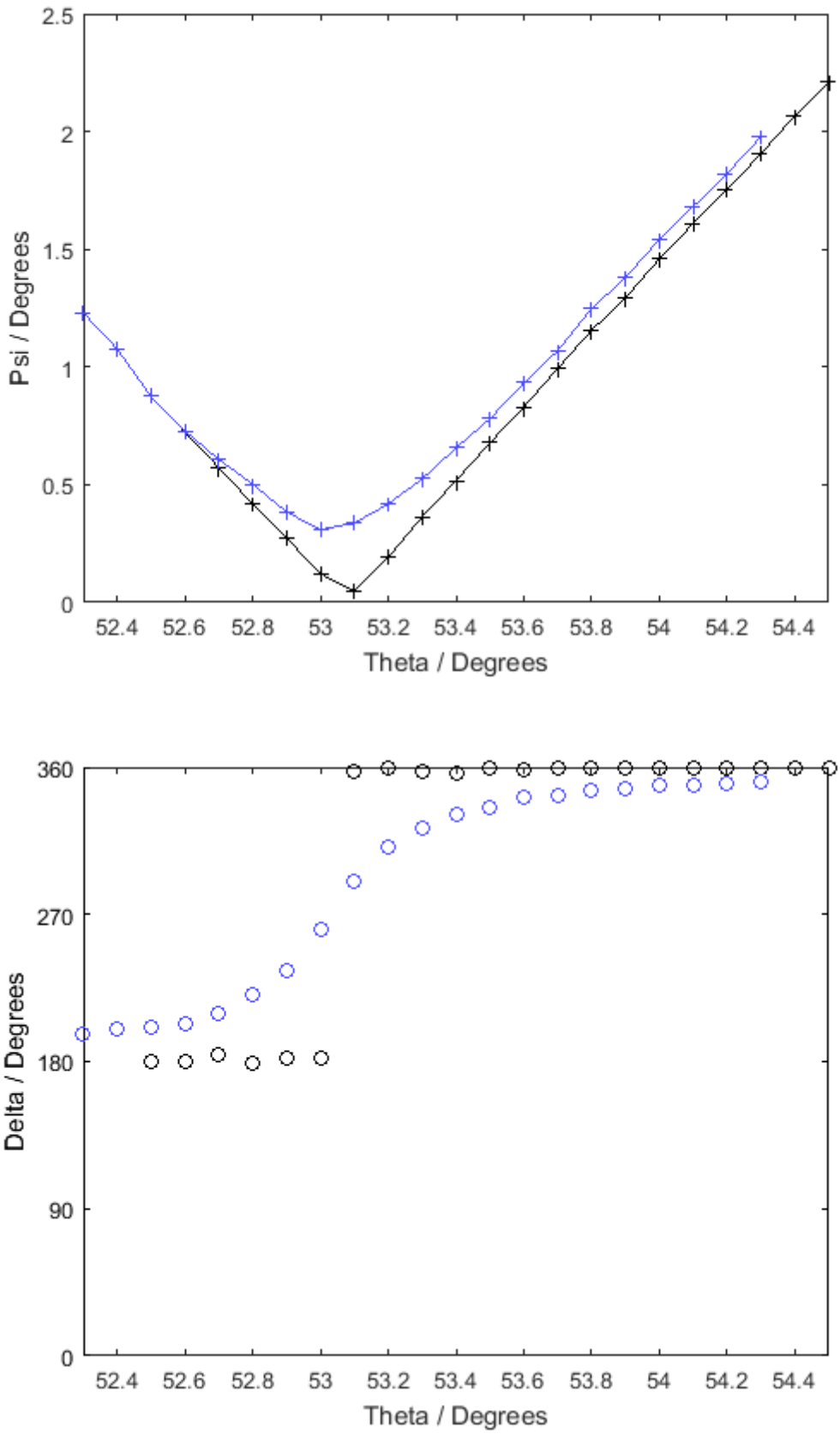

Figure 61 – Variable angle spectroscopic ellipsometry data for two samples of deionised water. The data set depicted in blue shows distinctly different data than was otherwise observed. Ψ and Δ both transition very slowly through the Brewster angle.

7.2 Organic Solvent Data

7.2.1 – Solvent Choice

In order to compare the data being acquired for this project compared to past data collected by Greef and Frey[115], a selection of the organic solvents used in that paper were tested. Ethanol and dodecane were selected because they were both used in the original paper, while methanol was also used because it was fully parameterised in the simulation package being used.

7.2.2 – Experimental Data

All experiments used 2° range of angle of incidence, with a resolution of 0.1°, around each solvent's Brewster angle, and has been adjusted to correct the angle as specified earlier using the Brewster angle of glass as a reference.

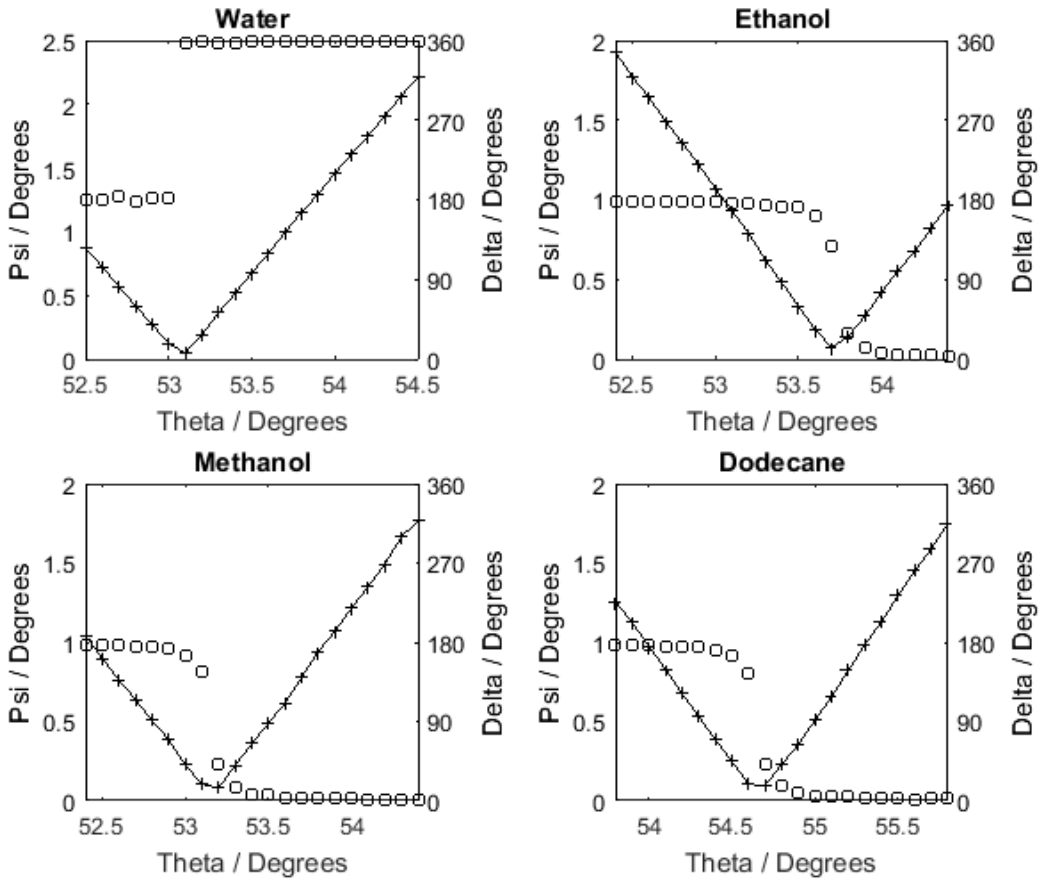

Figure 62 – Variable angle ellipsometry data for water, Ethanol, Methanol and Dodecane. Ψ plotted as a line with + symbols denoting data points, Δ is depicted as circles. For all experiments, theta passes through the Brewster angle of the liquid causing a 180° shift in Δ. In the case of water, this transition passes upwards to 360°, while the other three solvents tested transition downwards to 0°.

Figure *63* shows the relevant data from the aforementioned study. This paper used Brewster angle ellipsometry, the same as was used in section 7.1, to collect values of Ψ and Δ for water and several organic solvents. The same trend can be seen through the two data sets, though the method of data collection is different. Both data sets show Δ going to 360° as Ψ passes close to 0 for water, while Δ only ever goes to 0° for organic solvents. Additionally, in Figure *62*, all three organic solvents have very similar Δ shape as they go to zero, suggesting that they have a similar surface structure, with a gradually decreasing density from the bulk liquid to the atmosphere, with no higher density surface layer.

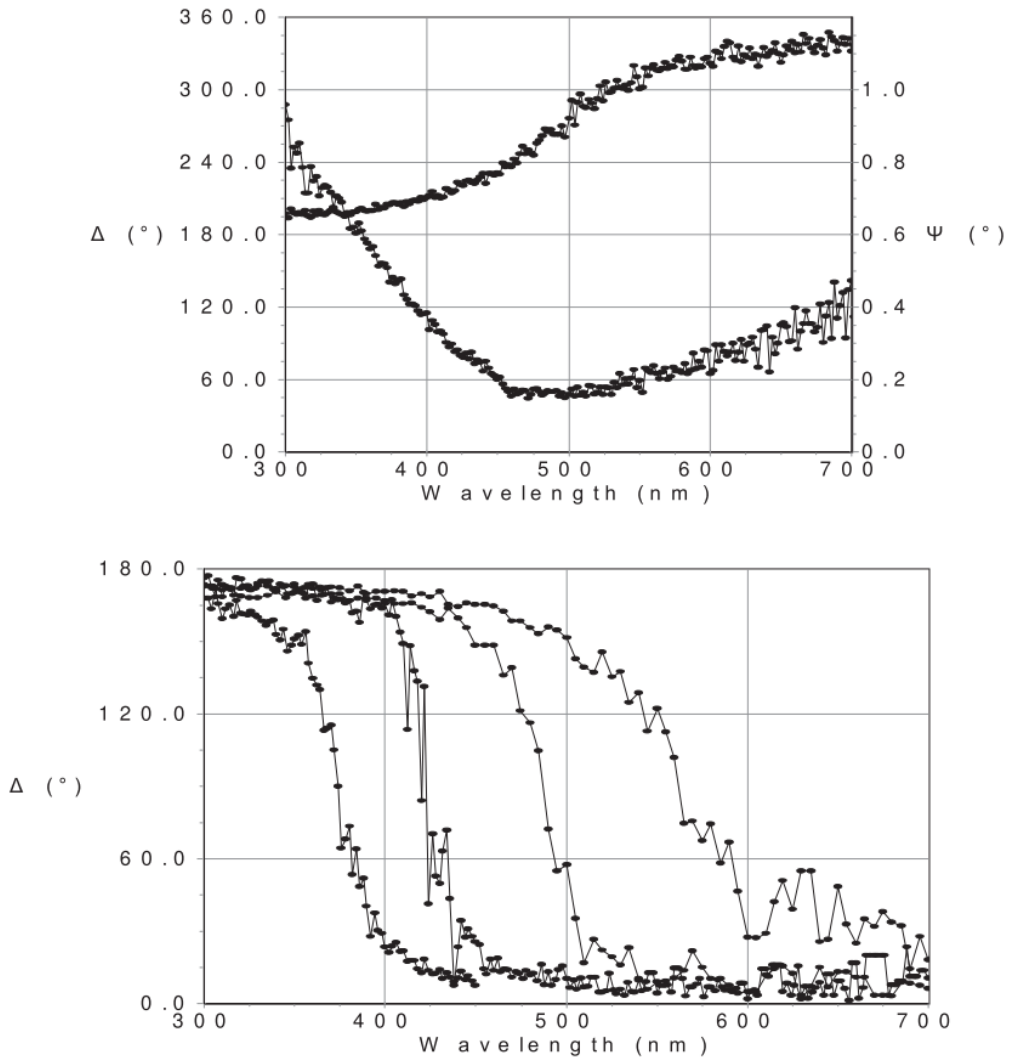

Figure 63 – Top, Ψ and Δ data for water (52.9°) from Greef 2008 paper. Bottom, Δ data for organic solvents, from left to right, with their angles of incidence, paraffin (56°), DMSO (55.8°), ethanol (53.7°), dodecane (54.7°) from Greef 2008 paper.

7.2.3 – Water/Ethanol Mixtures

In order to test the sensitivity of ellipsometry to the changes of the air/water interface, a selection of water/ethanol mixtures were tested to see the transition from water-like values of Δ, to ethanol-like. The following range of mixtures were tested.

Mole Percentage Ethanol	**Mass Percentage Ethanol**
0	0
0.1	0.28
0.5	1.48
1	2.54
2	4.89
5	11.75
10	22.02
50	71.58
100	100

Table 5 – Water/Ethanol solutions used in variable angle spectroscopic ellipsometry by mole and mass percentage

As shown previously, Δ transitions from 180° to 360° for water, and to 0° for ethanol. Therefore at some concentration of ethanol in water, there will be a shift from going to 360° to 0°. Figure *64* and Figure *65* show the Ψ and Δ data for each of these mixtures. Figure *65* shows the data for pure water, and then from 1 mol% ethanol up to 100 mol% ethanol. 0.1 mol% and 0.5 mol% were excluded from this graph because it was not possible to precisely place these two data sets between the sets for water and 1 mol% ethanol due to the imprecision in the ellipsometer angle. They are instead plotted with pure water and 1 mol% ethanol in Figure *64*.

It can be seen in Figure *64*, that the transition between Δ transitioning to 360° rather than 0° occurs around 0.5 mol%. In this data set, very near the Brewster angle, there are data points at 150° and 315°, heading in both directions, while all the data sets of a lower concentration of ethanol are have a clear transition to 360° and all those with a greater concentration have a clear transition to 0°.

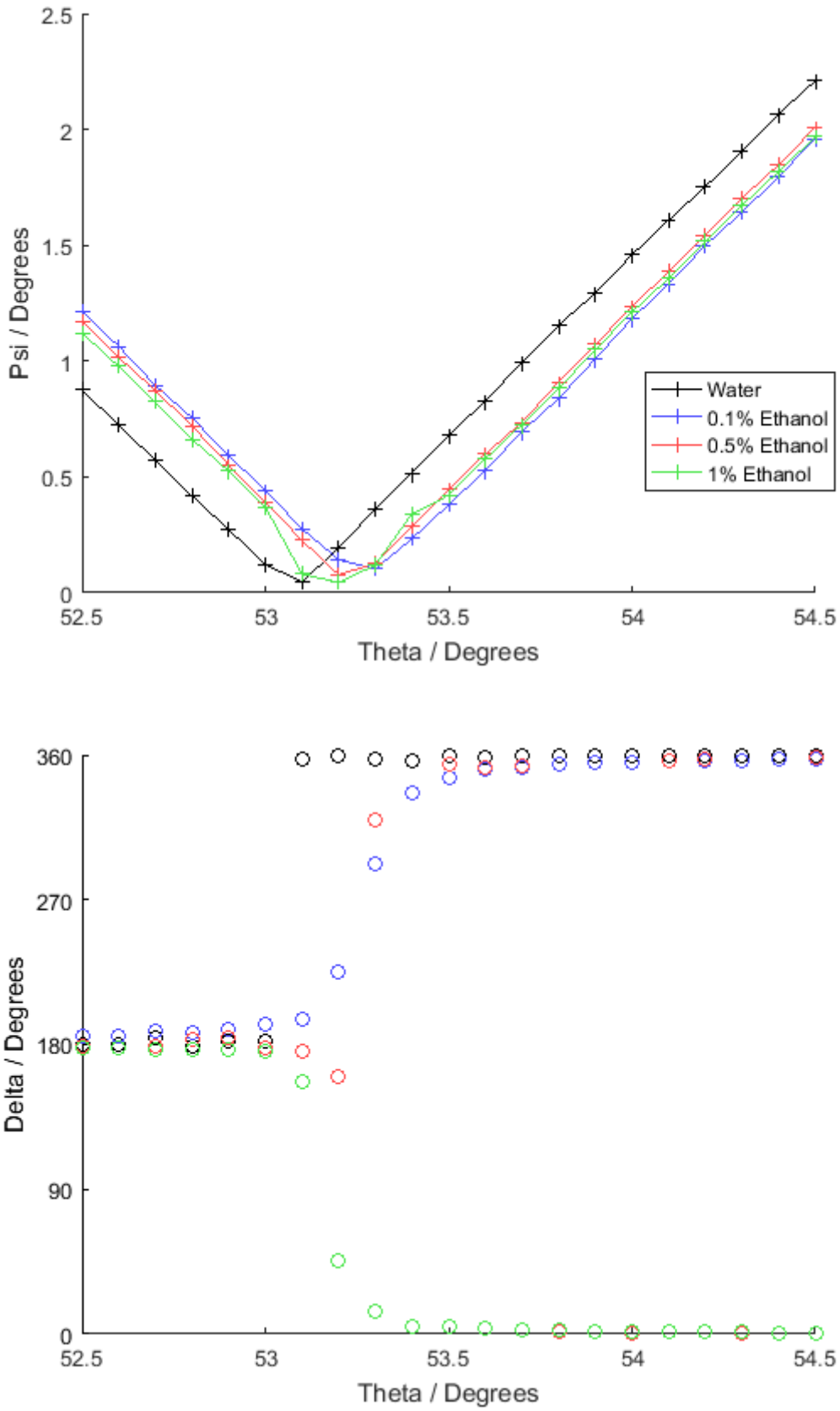

Figure 64 - Ψ (top) and Δ (bottom) data for low percentage water/ethanol mixtures. The values of theta are not precise due to the imprecision in measuring the angle of incidence of the ellipsometer. The change from Δ transitioning from 360° to 0° can be seen at 0.5 mol%.

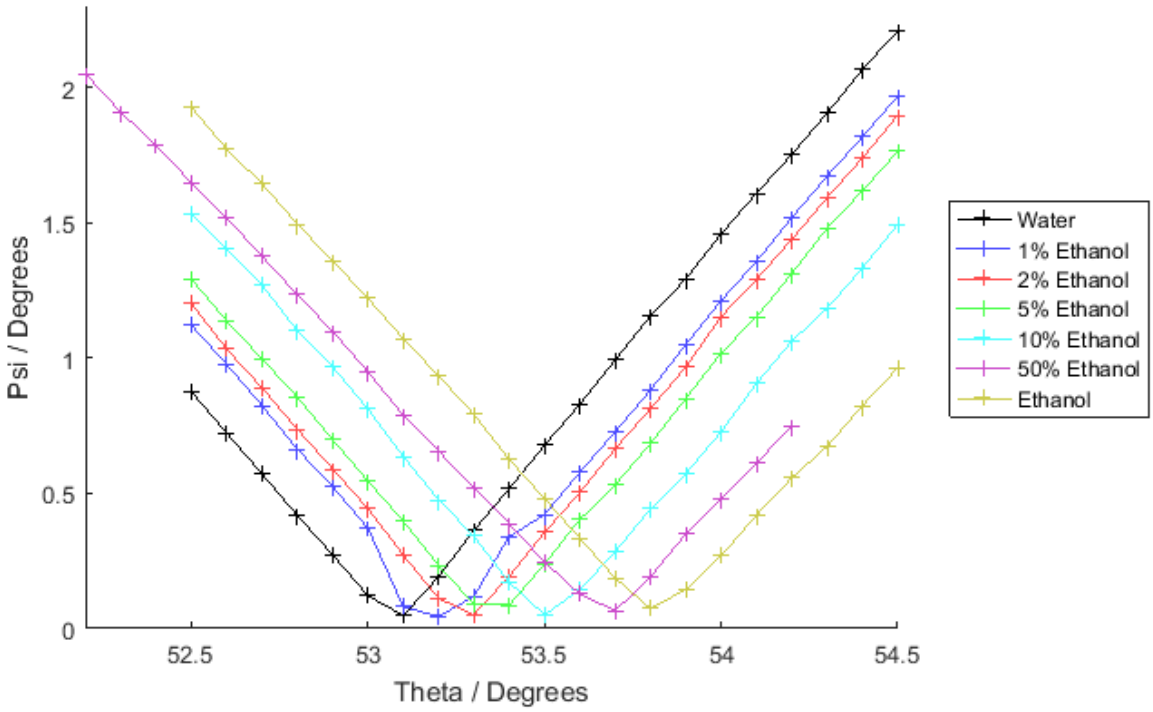

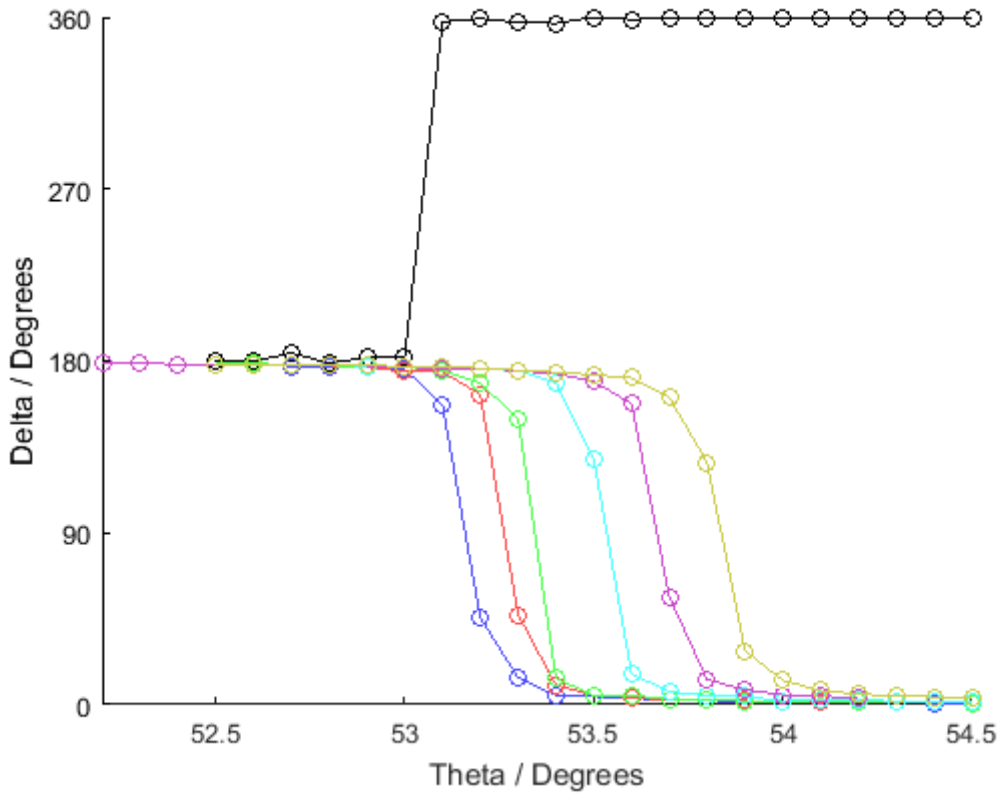

Figure 65 - Ψ (Top) and Δ (Bottom) data for deionised water and water/ethanol mixtures from 1 mol% up to 100 mol%. Due to the number of data sets for Δ, each data set is highlighted with a line. The Brewster angle can be seen to shift towards the value for ethanol as the concentration of ethanol increases.

The Brewster angle for these data sets can be calculated as the intercept between the values for Ψ on either side of the Brewster angle. These have been calculated for the data sets plotted in Figure *65*. The calculated values of Brewster angle have been plotted as a function of percentage shift towards the value of pure ethanol from water and compared to the surface tension, density and freezing point of water/ethanol mixtures in Figure *66*. The change in Brewster angle is most similar to the change in surface tension for water/ethanol mixtures, which is as would be expected since they are both surface properties, compared to the bulk properties of density and freezing point. This is because of the surface excess of ethanol in water ethanol mixtures.

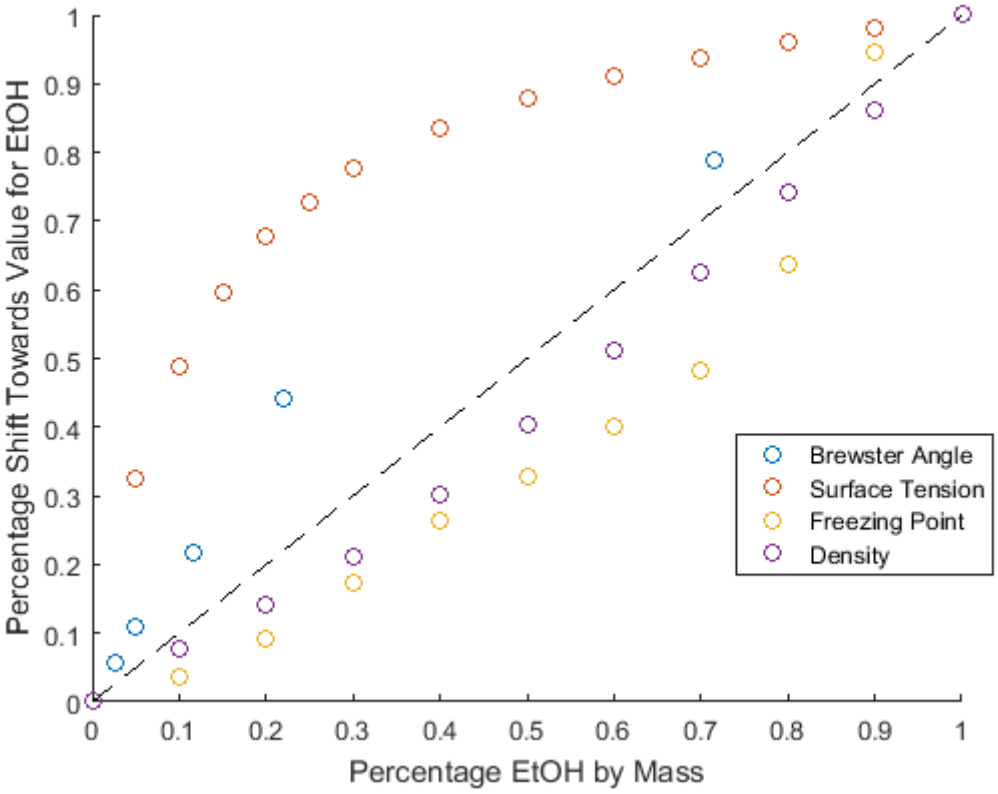

Figure 66 – Comparison of surface and bulk properties by percentage mass ethanol. Dashed line shows y=x. The bulk properties of density and freezing point mostly stay below the dashed line, while the surface properties increase at a much greater rate with a lower percentage of ethanol.

7.3– Water Impurities

7.3.1 – Water Purity

Further experiments showed a difference in the Δ profiles between different purities of water. Figure *67* shows the Ψ and Δ data for four different purities of water. Both deionised and tap water show Δ transitioning to 360°, while ion chromatography water and molecular biology water show Δ to 0°. These water samples were chosen because they have different impurities at varying concentrations. Water for ion chromatography (Sigma Aldrich) is listed with concentrations of ionic impurities all lower than at least 10 µg/kg and a conductivity of less than 2 µS/cm. Water for molecular biology (Sigma Aldrich) is made to have extremely low levels of organic impurities as well as low ionic content. Deionised water, by comparison is a lower purity while still maintaining a low ionic concentration. Tap water has by far the lowest purity of the samples presented.

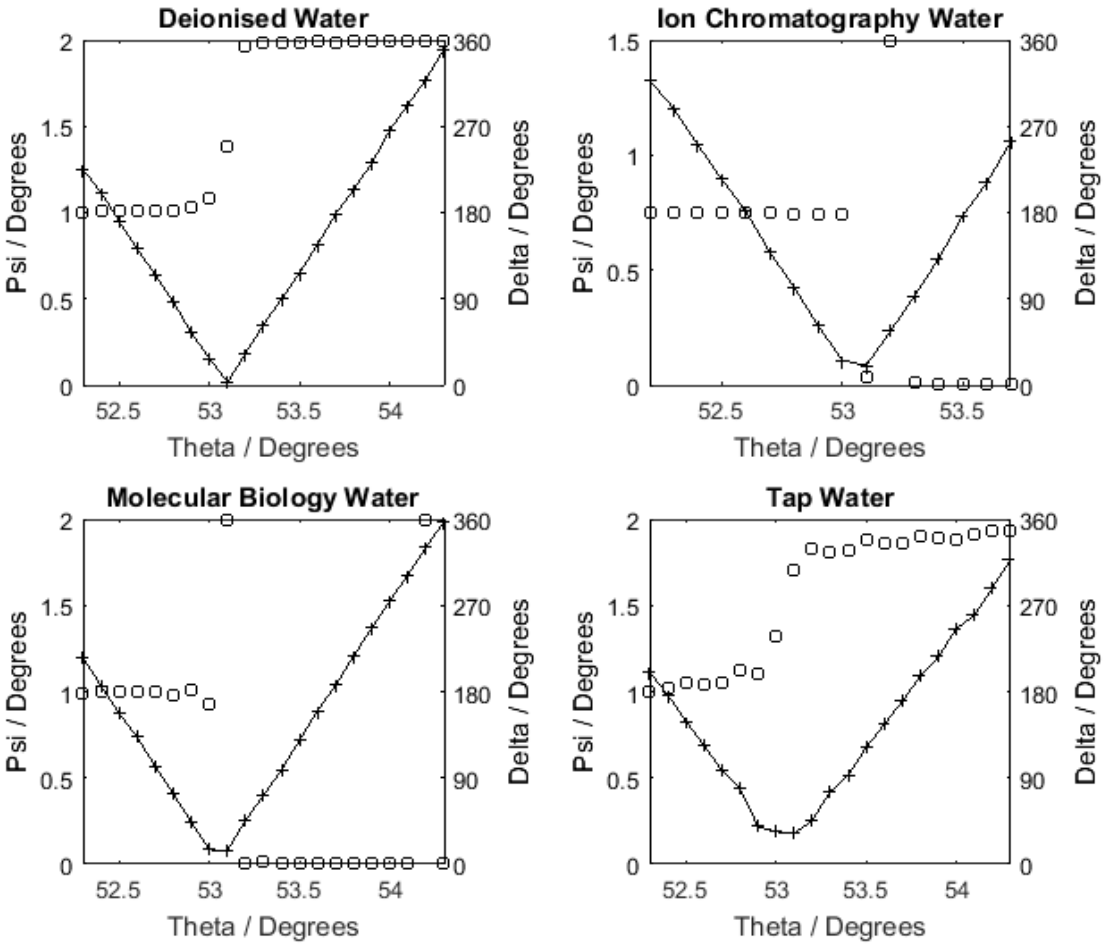

Figure 67 - Ψ and Δ data for different purity of waters. Ψ is shown as a solid line, while Δ is shown as a scatter plot. Deionised water and tap water show Δ transition to 360°, while the higher purity water samples show Δ transition to 0°.

A mixture of deionised and ion chromatography water was also tested, and shows Δ to 360°, though there is more noise than was otherwise seen between 0° and 360° beyond the Brewster angle. This is shown in Figure *68*. This change in Δ between different purities of water implies that small ionic impurities may having an effect at the surface at very low concentrations.

7.3.2 – Acid and Alkali Impurities

To test the effect of impurities on the values of Ψ and Δ measured through ellipsometry, low concentrations of HCl and NaOH were added to the highest purity water sample, ion chromatography water. These data sets are shown in Figure *69* and Figure *70*. As with the prior experiments, Ψ is unaffected, however Δ changes around 1 mM in both cases. Between 0.1 mM and 1 mM HCl, the measured value of Δ past the Brewster angle changes from 0° to 360°, indicating that the increase in ionic concentration is having an effect at the air/water interface. NaOH was only tested at a higher concentration of 1 mM and 10 mM, where Δ is transitioning to 360°. In both cases, the observed Brewster angle was not affected.

7.3.3 –Salt Impurities

In addition to testing acidic and alkaline samples, three salts were tested: NaCl, KI and $CaCO_3$. These salts were selected for their simple structures and varying molecular size. At 1 mM in ion chromatography water, the only salt which had an effect on the Δ values measured past the Brewster angle was $CaCO_3$.

At 1 mM, HCl, NaOH and $CaCO_3$ all affect the ellipsometry measurements of ion chromatography water, causing a Δ transition to 360°. At the same concentration, NaCl and KI are not having a noticeable impact. This does not guarantee that these two compounds are not present at the surface, but suggests that they are not having an effect on the surface density. HCl and NaOH are a strong acid and a strong base respectively, while $CaCO_3$ is a weak base. Since NaCl has no impact on Δ, while NaOH and HCl do, this suggests that the H^+ and OH^- ions are affecting the structure of the interface rather than the Na^+ and Cl^- ions.

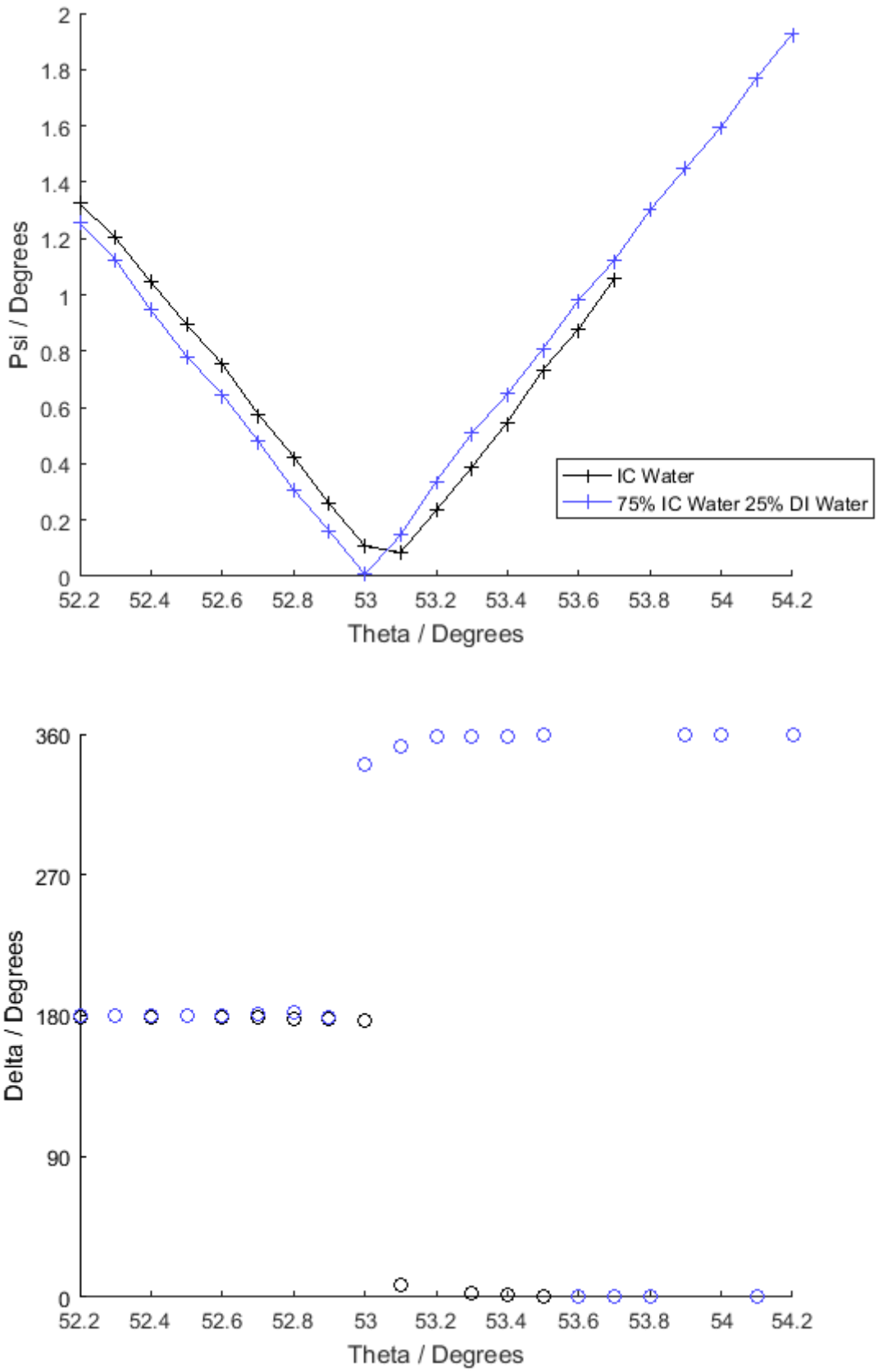

Figure 68 – Comparison of Ψ and Δ data for ion chromatography purity water and deionised water mixture. Ψ is shown as a solid line, while Δ is shown as a scatter plot. Addition of deionised water to ion chromatography water alters the Δ transition from 360° to 0°.

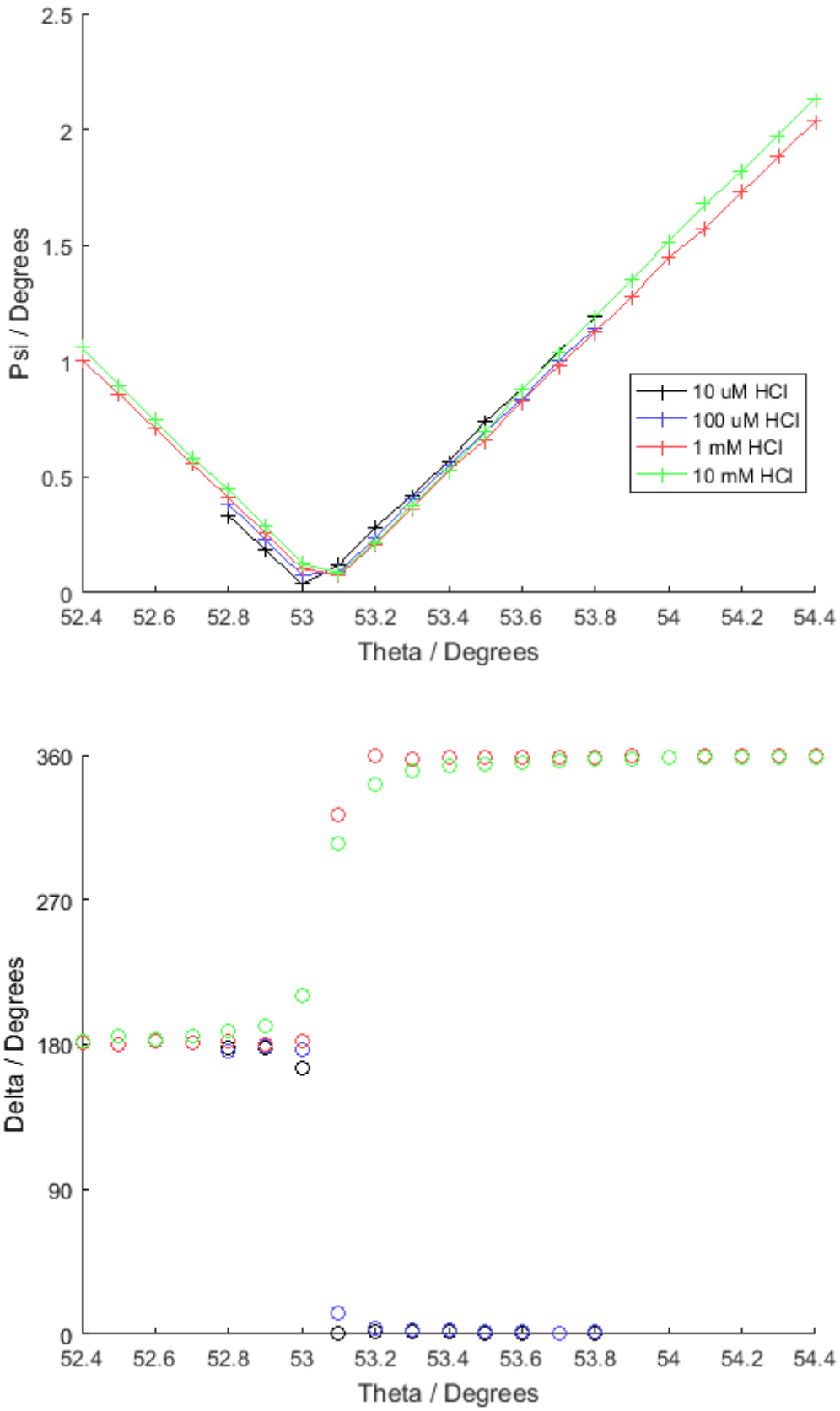

Figure 69 – Ψ (left) and Δ (right) data for HCl solutions in IC water. A change in the recorded values for Δ is seen between 100 µM and 1 mM.

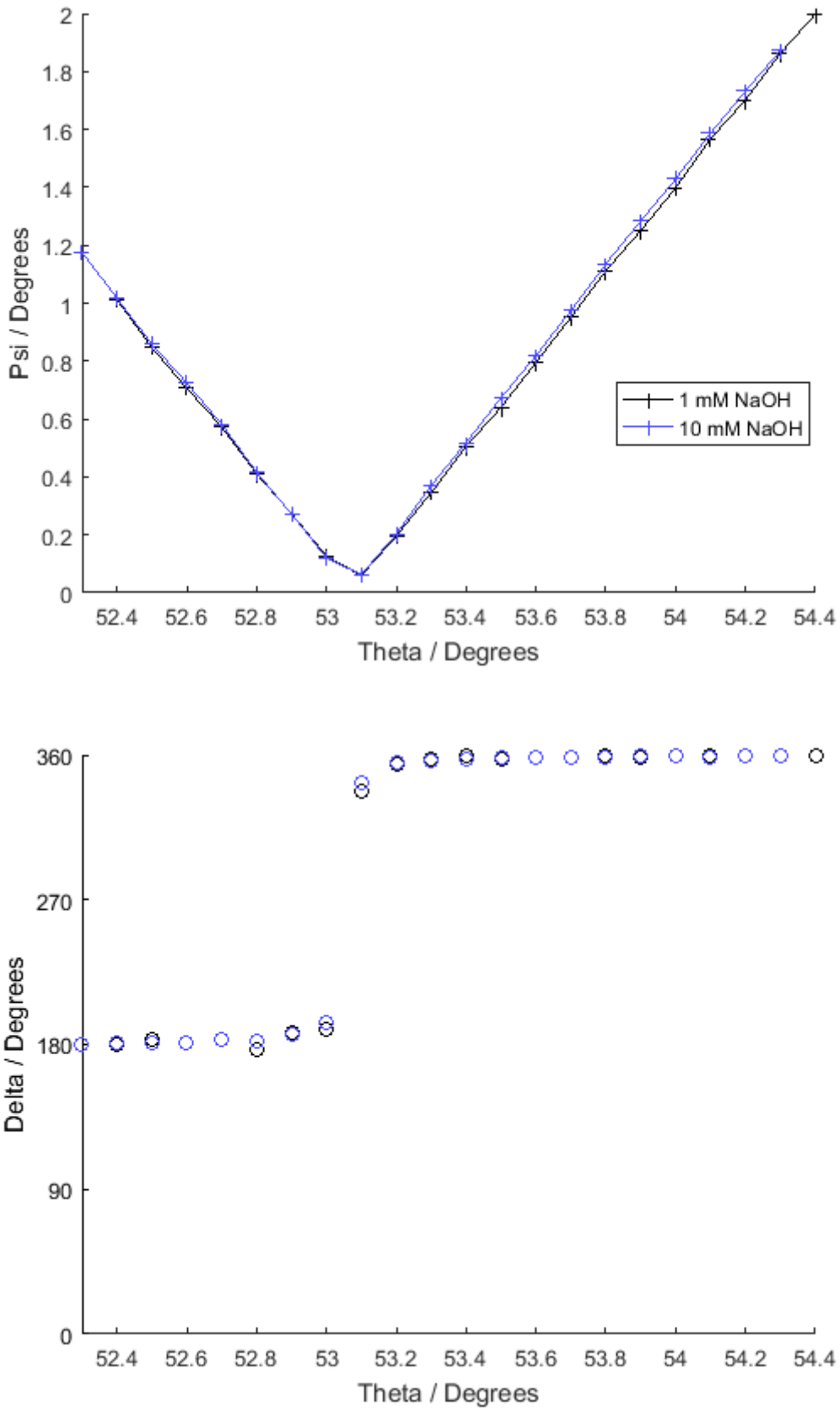

Figure 70 – Ψ (top) and Δ (bottom) data for NaOH solutions in IC water. Both 1mM and 10 mM show Δ transition to 360°.

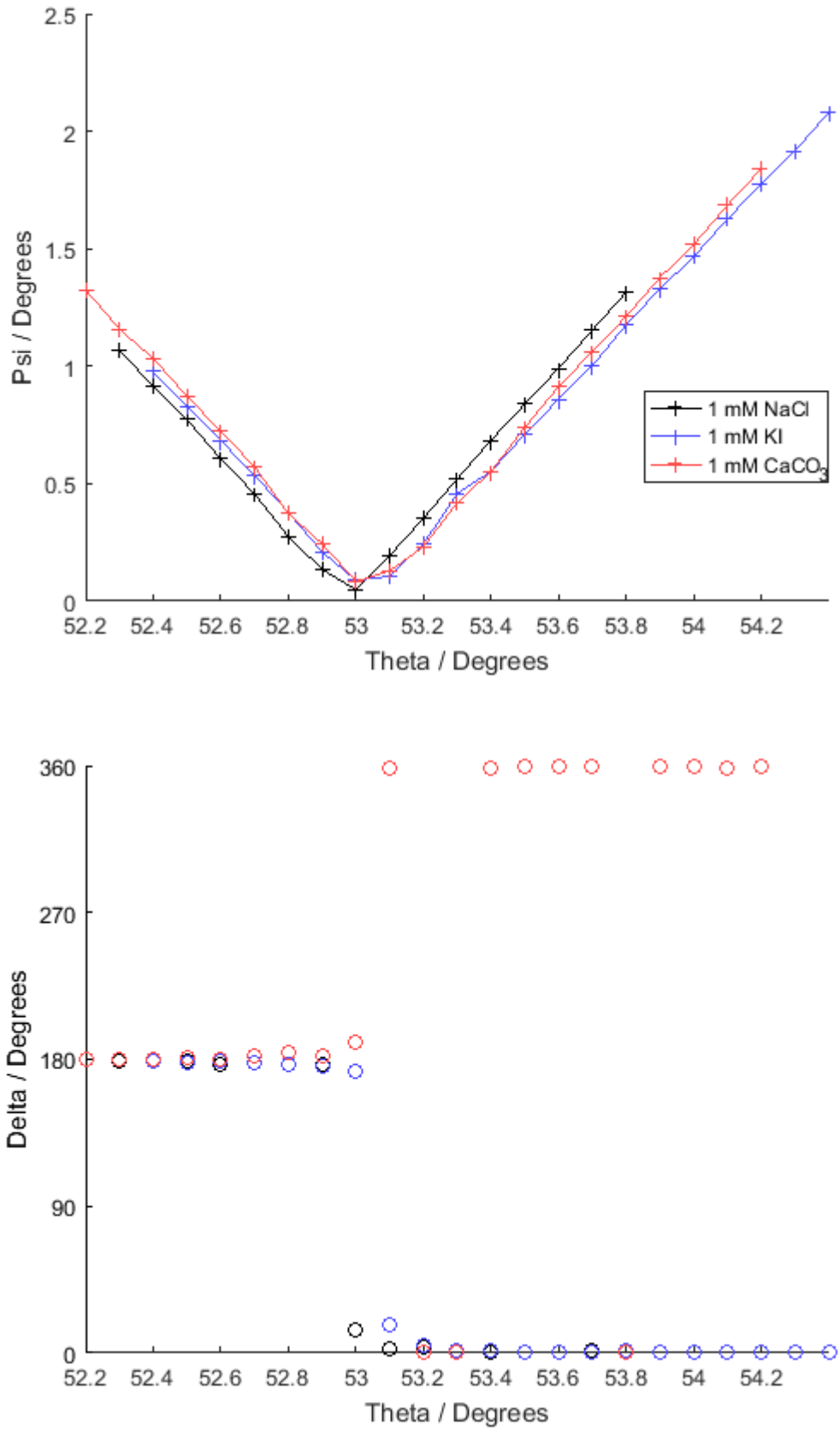

Figure 71 – Comparison of Ψ (top) and Δ (bottom) data for three neutral salts in IC water at 1 mM. At this concentration, only $CaCO_3$ had an observable impact at the surface.

7.4 – PNP Ellipsometry

7.4.1 – 70° Angle of Incidence

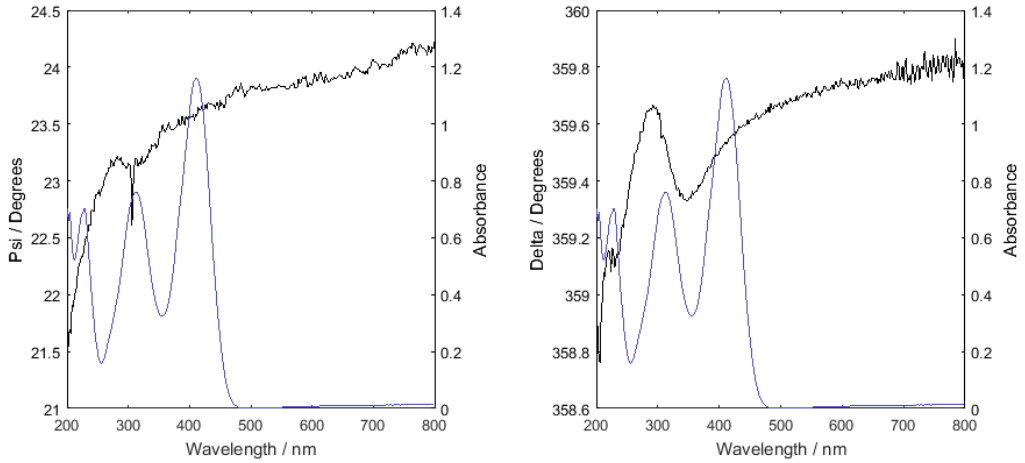

Figure 72 - Ψ (left) and Δ (right) data for 15 mM PNP solution at 70° AOI with UVVis spectrum of a PNP solution in water overlaid in blue. Δ is close to 360° across the entire spectrum since the experiment was performed far past the Brewster angle.

Figure *72* shows Ψ and Δ data for a 15 mM PNP solution at 70° AOI. In both data sets, features can be seen around 320 nm which corresponds to the peak caused by the phenol absorption, as seen in UV/Vis spectroscopy. No peak is seen for the phenolate around 420 nm, since the phenolate is not observed at the surface, as shown in 1987 by Bhattacharyya et al.[8]

7.4.2 – Brewster Angle

Figure *73* and Figure *74* show Ψ and Δ data for a 15 mM PNP through the Brewster angle. Figure *73* shows the variable angle data, with Δ increasing to 360°. This could be indicative of the PNP surface layer, however the data is comparable to the Δ which was seen for the normal air/water interface. Figure *74* shows Brewster angle ellipsometry data. Since this experiment depends on varying the wavelength rather than the angle, the spectral features from the phenol absorption can be seen as in Figure *72*.

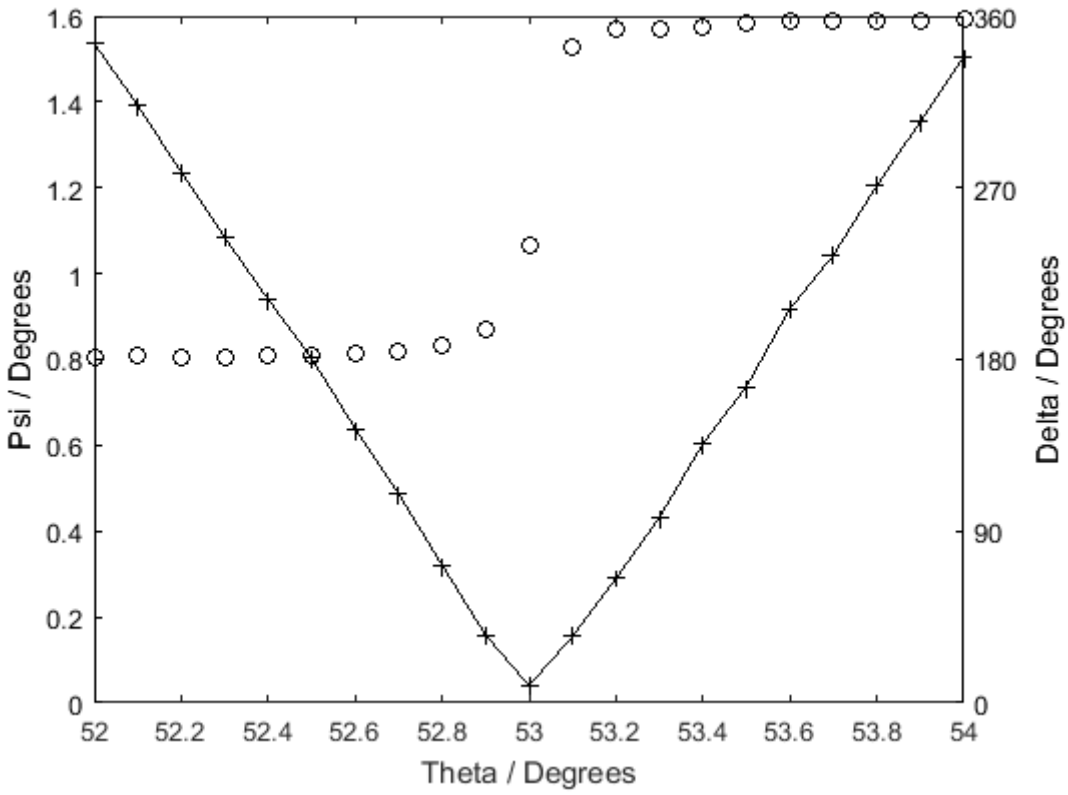

Figure 73 - Ψ (solid line with +s) and Δ (circles) data for a 15 mM PNP solution.

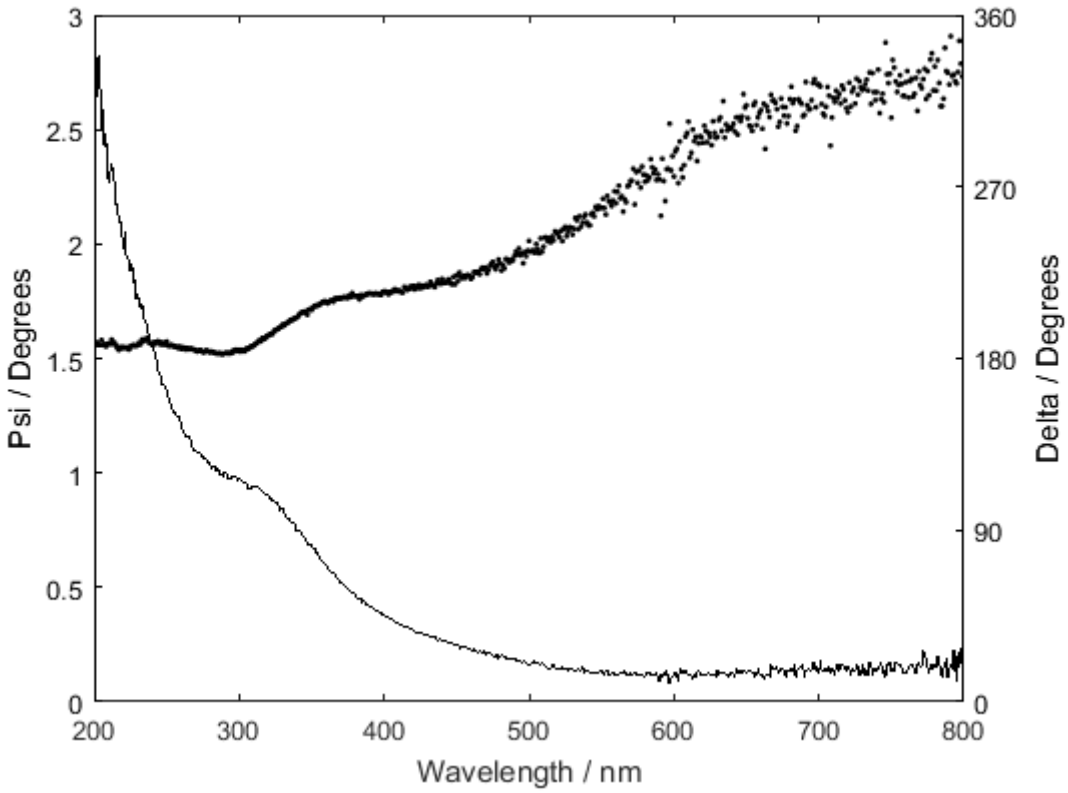

Figure 74 - Ψ (solid line) and Δ (scatter plot) data of a 15 mM PNP solution at 52.9° angle of incidence.

7.4.3 – Titration

In order to watch the change at the interface if a PNP solution as the pH changes, ellipsometry experiments were performed as the pH was increased by titration. A 30 mM PNP solution was prepared, and acidified with HCl. The pH was measured with a probe before each experiment, accurate to 0.1 pH. Between experiments, a small volume was pipetted out of the sample, and this was replaced by an equal volume of 30 mM PNP, 100 mM NaOH solution to increase the pH. The calibration of the machine with the sample was optimised and the experiment repeated. Decrease in delta peak around 320 nm as the pH increases and the phenol concentration drops. The peak around 300 nm decreases as the pH increases to neutral. Since this peak is likely caused by the phenol absorption, as the pH increases, the concentration of the phenol form of PNP drops, and so this peak becomes less intense.

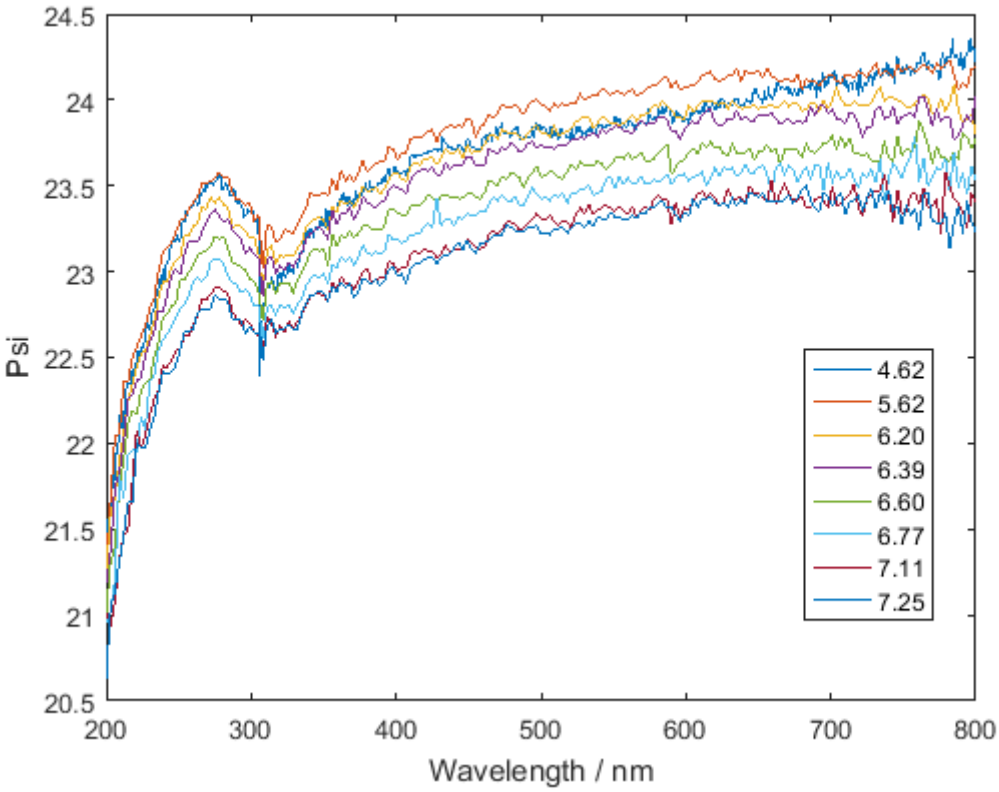

Figure 75 - Ψ data for the titration of a 30 mM PNP solution. The solution started at a pH of 4.62, and an alkaline solution of PNP was added between each run and the pH was remeasured.

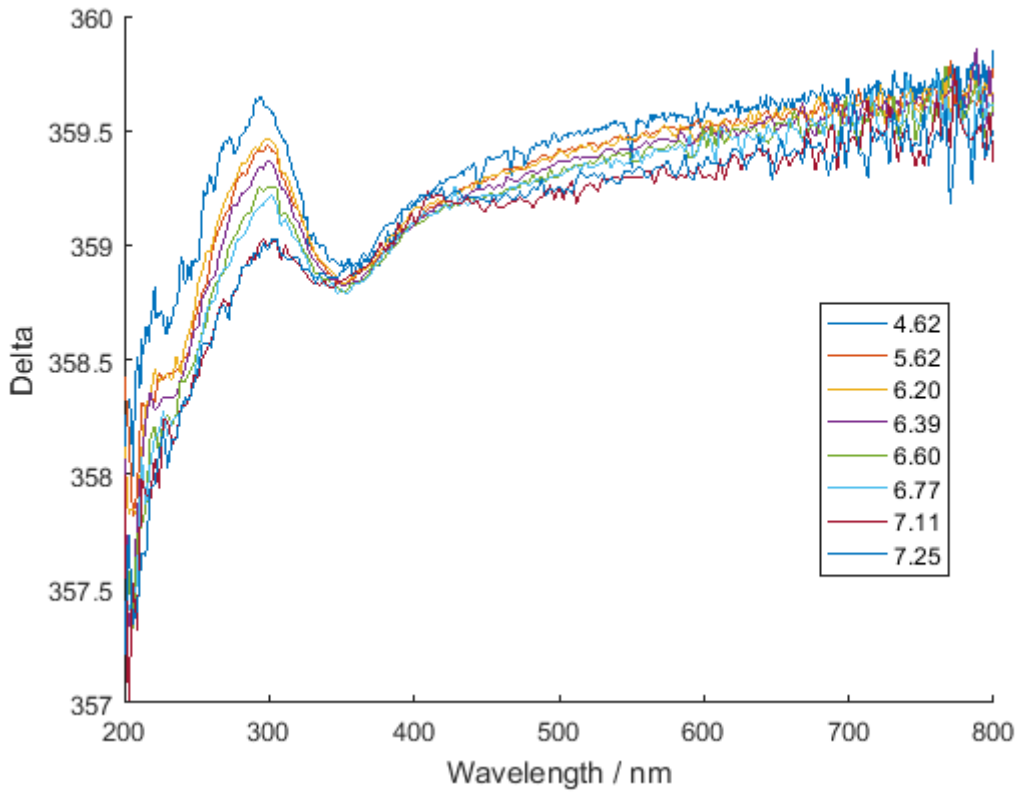

Figure 76 – Δ data for the titration of the same 30 mM PNP solution described in Figure 75

7.5 – Simulation Data

Running parallel to this work, work was done to simulate the air/water interface to calculate the surface properties of Ψ and Δ by Dr Frank Longford. This work was performed in AMBER and consisted of a slab of water with vacuum on either side repeating infinitely in the x and y planes due to periodic boundary conditions. The slab of water was made of 500 molecules and used classical models for calculation. The slab of water was a 0.8 nm cube. Vacuum was used instead of modelling air due to the volume of the simulation. To fill the vacuum to atmospheric pressure, only a single N_2 molecule would be needed, therefore this was not included due to the minimal impact it would have.

Simulations were run for 8 ns to equilibrate to a surface and then the density was measured through the z axis, giving a density profile for the simulation. Taking the density through the simulation without defining any surface gives a normal density profile for a liquid as shown for $q_m = 0$ in Figure *78*.

Therefore, work was undertaken to define an intrinsic surface with respect to the location of the molecules within the simulation which would generate a transition of Δ to 360° for water, but to 0° for other solvents, such as methanol. This was done by creating a 3D surface which tracked through simulation based on the positions of the outer water molecules and calculating the density along the z axis from this surface. Fitting this surface strenuously to the positions of the water molecules gave a very spiky surface, with a very dense surface layer. This is understandable, as this defines the surface as where water molecules are located, so it is self-selecting to create a high density at the surface. Conversely, applying a much looser fit for the surface gave a much smaller surface density peak. Two intrinsic surfaces are shown in Figure *77*.

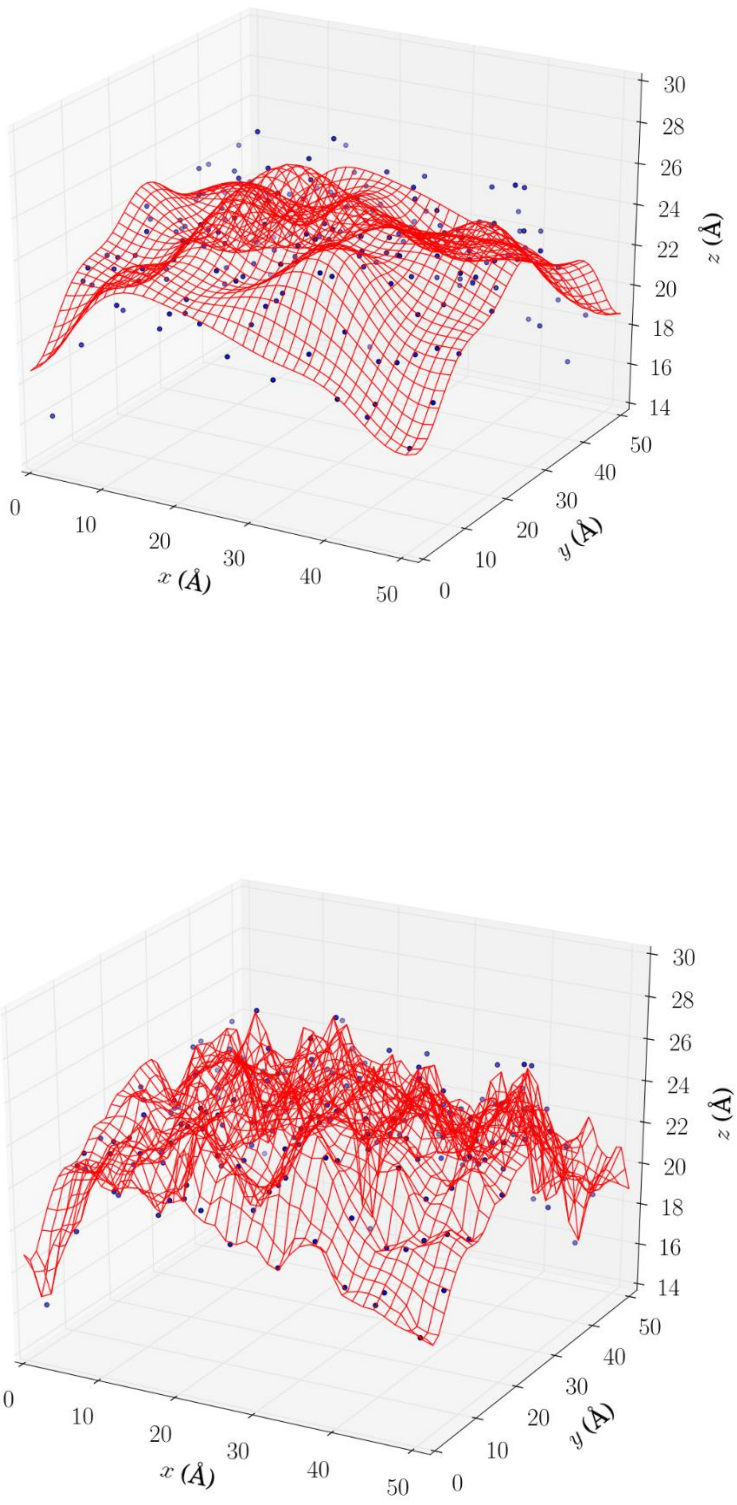

Figure 77 – Two intrinsic surface models for a simulated surface. The blue dots show molecular positions and the red mesh indicates the location of the intrinsic surface. The top image shows a loose fit to the molecular locations, while the bottom image is much higher resolution.

Figure *78* shows the density profiles of simulations of water and methanol using varying resolutions of the intrinsic surface, q_m[117]. A value of 0 for q_m would relate to a flat plane with no defined intrinsic surface. As q_m increases, the intrinsic surface is more tightly bound to the locations of the molecules at the surface, and therefore there is an increasing surface density peak which is observed. This also causes the density directly behind the intrinsic surface to drop closer to 0 because it is not probable for molecules to be directly behind the intrinsic surface when it is such a high resolution.

Methanol is a larger molecule than water which accounts for the differences observed along the z axis of the density profiles. As a result, the surface increases more gradually when there is no intrinsic surface applied for methanol compared to water, and as the intrinsic surface increases in resolution, there is a slightly longer gap between the surface peak and the second peak due to the larger size of methanol molecules. This is also the cause of the higher density value for the simulations of water, since it packs more densely.

Figure *79* shows the Clausius-Moretti-Lorenz-Lorenz effective refractive index distributions calculated for water and methanol using a range of resolutions of the intrinsic surface for each simulation[118]. The calculated refractive indices for the ordinary and extraordinary polarisations are shown, and no noticeable birefringence is observed for any resolution of the intrinsic surface of water or methanol. Above a resolution of $q_m = 10$, there is a greater refractive index calculated for the water surface than the bulk, which is not seen for methanol. This is not a great enough difference to cause the difference in experimental data between water and methanol for Δ on its own, however this supports the hypothesis that water has an apparent surface layer of higher density than the bulk.

Further calculations to extrapolate the ellipsometric coefficients of Ψ and Δ from the intrinsic surface have been started, but are not yet robust enough to definitively explain the experimental results obtained in this work. This is partially due to the classical methods of calculation, which do not properly account for processes such as polarizability which could have a large impact at how ellipsometry views the surface. Additionally, the method for the calculation of Ψ and Δ is designed for a flat surface, rather than the intrinsic surfaces used in these simulations. This reduces the certainty that any predictions are valid as the resolution of the intrinsic surface increases.

The work done in sections 7.2 and 7.3 involving water/solvent mixtures and impurities in water was not modelled in the simulations performed because of the size of the simulations. At the concentration which most of the compounds had an observable impact on the experimental value of Δ, 1 mM, the impurity would be represented by approximately 1 molecule compared to 500 water molecules at the surface, which is expected to have little impact on the surface formed.

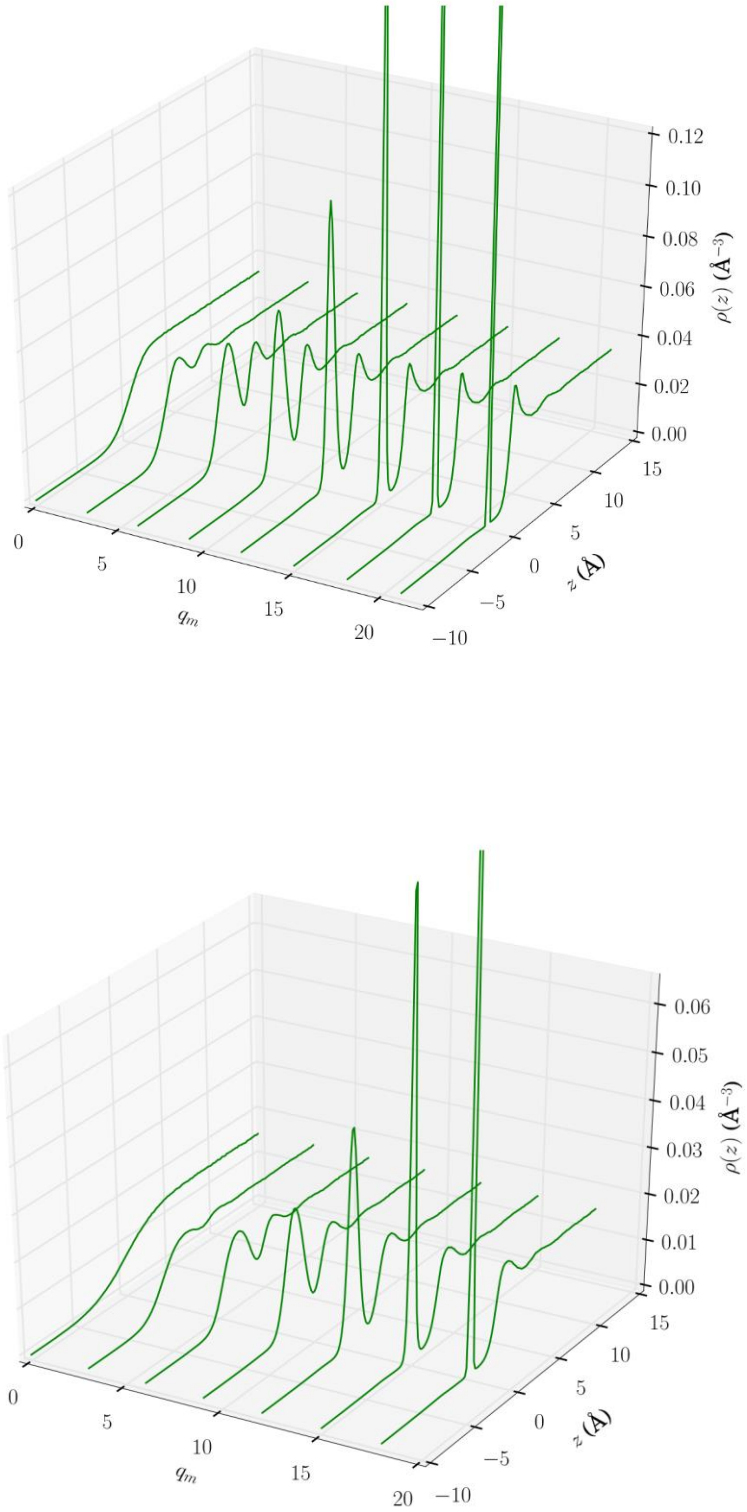

Figure 78 – Density profiles for water (top) and methanol (bottom) for different resolutions of the intrinsic surface. q_m is the resolution of the intrinsic surface, z is the distance through the simulation and ρ(z) is the density. Increasing resolution of the intrinsic surface in both cases leads to a higher surface density peak as the surface is more tightly constrained to the surface molecule location.

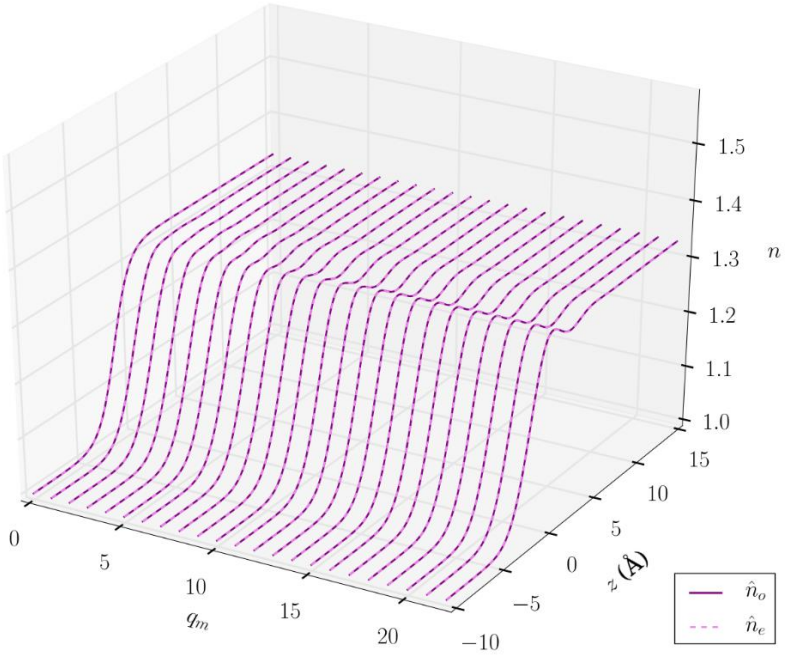

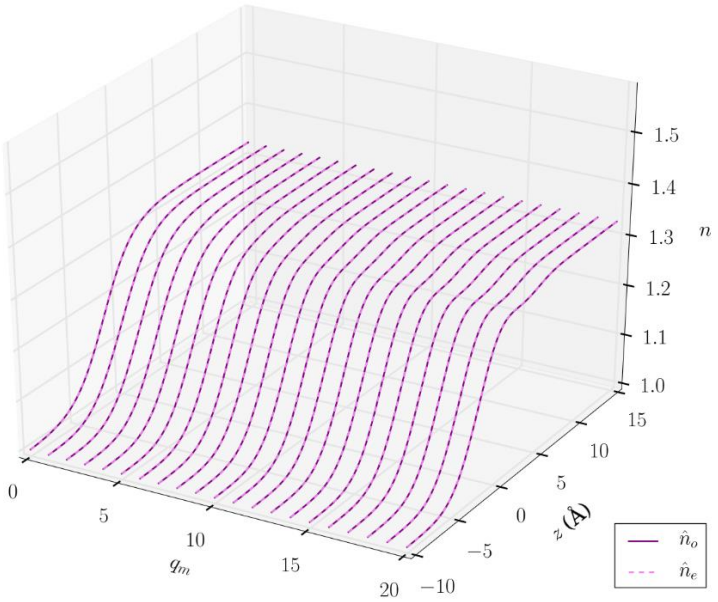

Figure 79 – Calculated refractive indices of the simulations of water (top) and methanol (bottom) for different resolutions of the intrinsic surface. n_0 and n_e are the calculated refractive indices for the ordinary and extraordinary polarisations of light. These values were calculated using the Clausius-Mosetti-Lorenz-Lorenz method. At high resolutions there is a noticeable increase of the refractive index for water, which is not observed for methanol.

7.6 Conclusions and Further Work

Through this work, it can be seen that spectroscopic ellipsometry is an effective tool for studying air/liquid interfaces both by the variation of wavelength and angle of incidence. As noted by previous studies, by measuring Δ through the Brewster angle of the liquid, ellipsometry can differentiate between water and organic solvents by the direction of the 180° shift which occurs, either towards 360° for water or 0° for all the organic solvents which have been tested. Further to previous work, this study has shown that the purity of water also has an impact on the measurement of Δ, with certain very high purities giving a Δ transition to 0°. The addition of various neutral salts as well as acids and bases had varying impacts on this at low concentrations, suggesting that they have a role in the structure of the air/water interface at a potentially enhanced concentration.

Simulations running alongside this work have proven fruitful to help understand the measurements which ellipsometry is making at the air/water interface and the structural differences which cause the difference in experimental data between water and organic solvents. These simulations suggest a higher refractive index for water at the interface, which is not present for other solvents as a potential factor for these differences. These simulations do not currently factor in the work concerning purity which was performed for this work, and could also be expanded to encompass more complex interactions within the simulation such as intermolecular polarizability.

Further experimental work could be performed to continue to understand the role of purity on measurements of Δ at the Brewster angle of water. The compounds which have already been studied could be tested at varying concentrations, as was performed for HCl, in order to see the concentrations at which they have a measureable impact on Δ. Additionally, the impacts of other conditions on the air/water interface could be studied through variable angle spectroscopic ellipsometry, such as temperature in order to gain a better understanding of the interface.

Chapter 8 – Final Conclusions

Initial work on this project aimed to study crystallisation. This was performed through three areas: SHIM, MBANP polymorphism tests and the SCXRD sublimation experiments. These experiments had varying levels of success. The SHIM setup was designed and refined to improve the resolution of the technique to the diffraction limit of the wavelength, at close to 1 µm. From this point the imaging system was used to generate images of the second harmonic signal of the crystal, similar to other second harmonic imaging techniques, such as SONICC. A novel experiment was also designed to watch the nucleation and growth of noncentrosymmetric crystals through their second harmonic signal. This experiment showed promise, with results showing very intense second harmonic signals at the start of crystal growth, which were attributed to the presence of small nucleates in solution. Unfortunately, development of this technique beyond this point was not possible due to equipment failure.

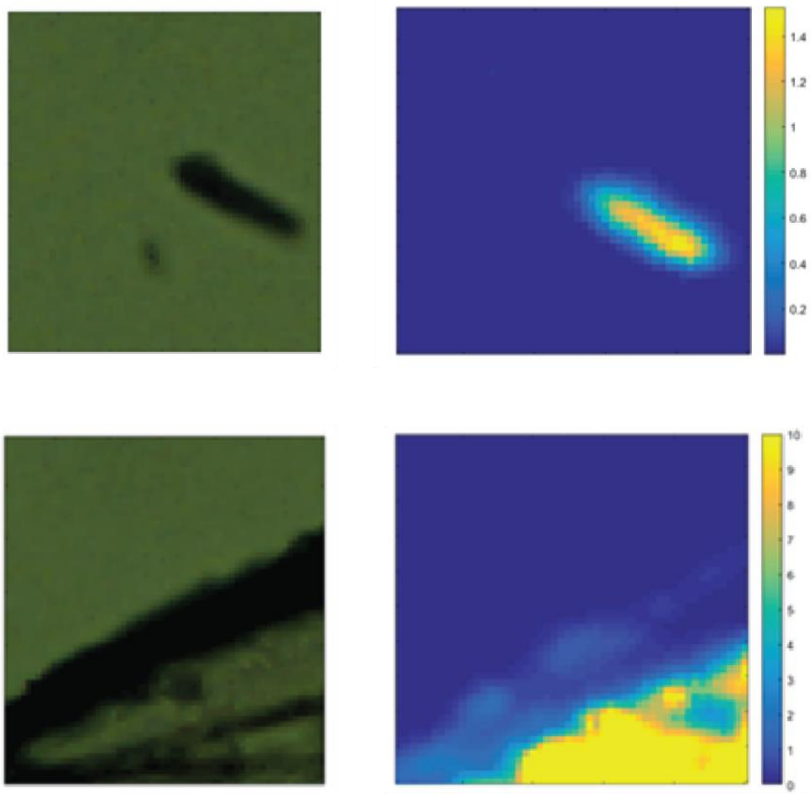

Figure 80 – Example images collected by SHIM of MBANP crystals. Left images show optical images, right images show second harmonic intensity. Top images show a small MBANP crystal, bottom images show the edge of a larger crystal.

Parallel to this work, a study was performed on the crystallisation habits of MBANP. Despite trying a variety of solvents, it was found that they all caused the crystallisation of the same polymorph of MBANP, that which was quoted in the literature.

A final experiment was designed to study crystals through SCXRD. In this experiment, a urea crystal was sublimed over the course of several hours to look at the ratio of Bragg vs non-Bragg scattering. The conditions of this experiment were perfected for the properties of a urea crystal, and a complete data set was successfully collected. The intensity of the Bragg peaks were easy to analyse due to their high intensity, even for a small crystal, however, the much weaker non-Bragg scattering was more challenging to extract from the Bragg scattering and background noise. Further analysis required the simulation of small crystals, to build and simulate the effects of thermal disorder and defects, to compare to the experimental data. This analysis proved to be beyond the scope of the project, and therefore it was not pursued further.

The effect UV irradiation upon PNP was first noted in the 19th century, and has been studied intermittently since then. In this work, a sample of PNP was fully converted to the irradiated form for the first time by repeated grinding and exposure to a broadband UV light. After this, the irradiated sample was successfully recrystallized to make a sample which was capable of undergoing SCXRD. Interestingly, the sample showed the presence of two polymorphs, which matched exactly with the α and β polymorphs of PNP, despite growing from diethyl ether, a solvent which only produces the α form of PNP. Due to the elusive nature of hydrogen atoms in SCXRD, it was not possible to fully verify the most popularly theorised mechanism of PNP irradiation, a transfer of the phenolic hydrogen to the nitro group, but the recrystallization of the irradiated sample supports this theory. Dissolution of the irradiated sample in water caused it to change back into PNP, however dissolution in aprotic organic solvents, such as diethyl ether kept the irradiated structure. If the hydrogen transfer theory is correct, it is easy to see that the irradiated compound can easily transfer the hydrogen back to the phenol when it is in an aqueous environment, but that an aprotic environment would cause the irradiated structure to persist.

PNP was also studied at the air/water interface as it formed a surface layer through Langmuir Blodgettry and tensiometry. Langmuir Blodgett experiments showed a decrease in surface tension over time, which could be broken down into two stages, an initial exponential like step, which followed a first order time dependent Langmuir rate, and a second, much longer pseudo zero order stage. On a molecular level, the first stage of this layers growth is caused by the movement of the PNP to the surface, while the second stage is a reorganisation of the PNP at the interface. It was noted that during Langmuir Blodgett experiments, the layer only became compressible after undergoing the pseudo zero order step. This correlates with past literature work, which found that at the early stages of the growth of the layer, PNP was only loosely bound at the surface. Further analysis of the Langmuir Blodgettry work was hampered by issues with reproducibility of data. While some progress was made to understanding the experimental preparation which was required to gain

good quality data, namely vigourously stirring the solutions while carefully controlling the temperature of the solution, it was not possible to get the experiment to run reliably within the limited time for which the experimental equipment was available.

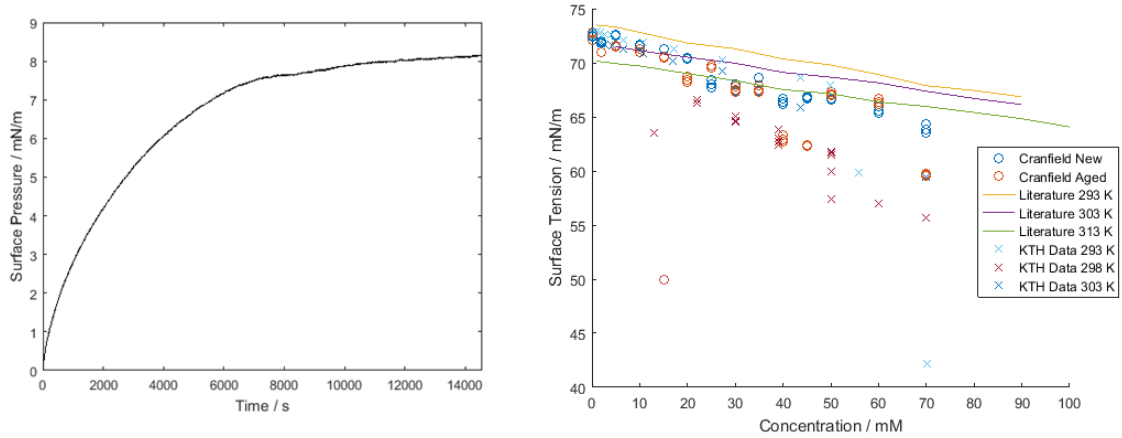

Figure 81 – Left, surface pressure data of a 15 mM solution of PNP over four hours, initial growth is a time dependent first order Langmuir, while this gives way to a pseudo linear step. Right, tensiometer data for PNP solutions with respect to concentration, showing the increasing potential surface pressure change with as the concentration increases.

This work agrees with the past literature work on the surface activity of PNP by Paluch and Filek, who studied the very early stages of the layer's lifetime by a flowing jet method, but did not study the surface tension beyond the first second of its formation, leading them to find the lower limit of the surface tension effect of PNP on water by concentration. By using tensiometry, this work has studied how the surface tension of the PNP solutions decrease further with time. Absolute surface tension values show that as the concentration of PNP increases, the maximum surface tension drop increases due to the equilibrium between the surface and bulk supporting a higher concentration of PNP at the surface. There is also some tensiometry evidence of a very organised surface film, which has a 20-30 mN/m decrease of surface tension, however there is not conclusive evidence for this layer's existence, or reliable methods for its formation.

Past work at the air/water interface suggests that there is a possible surface layer of higher density than the bulk. Initial work in this project was planned to replicate this data, since early ellipsometry data did not show the phenomenon. Brewster angle ellipsometry of water showed that it produced a shift of Δ from 180° to 360° through the Brewster angle, as shown previously by Frey and Greef in 2008. Variable angle spectroscopic ellipsometry was then used to continue to probe the air/water interface. Unlike previous studies, different purity levels of water were tested, along with tests to determine the effect of impurities on ultrapure water. It was found that ultrapure water samples had a Δ transition to 0° through the Brewster angle, while lower purities including deionised water

and tap water both produced a transition to 360°. Further to this it was found that the addition of millimolar concentrations of multiple ionic compounds were capable of effecting the Δ data of the ultrapure water, causing a transition to 360°. It is possible that this effect of purity is responsible for the difference in data between the literature sources, however since not all the papers report the exact purities of the water used in their experiments, it is not possible to state this with absolute certainty.

This data does however suggest that these impurities are having a profound effect at the air/water interface, even at low concentrations, causing a layer of higher density or other increased level of order which is responsible for the change in the ellipsometry data collected for this work. Within the selection of molecules which were tested, it is clear that both acidic (HCl) and basic (NaOH) compounds are impactful at the interface, however interestingly, KI, a salt which is well known for its surface activity, due to the large size of the iodide ion, did not affect the measurement of Δ at the concentration tested.

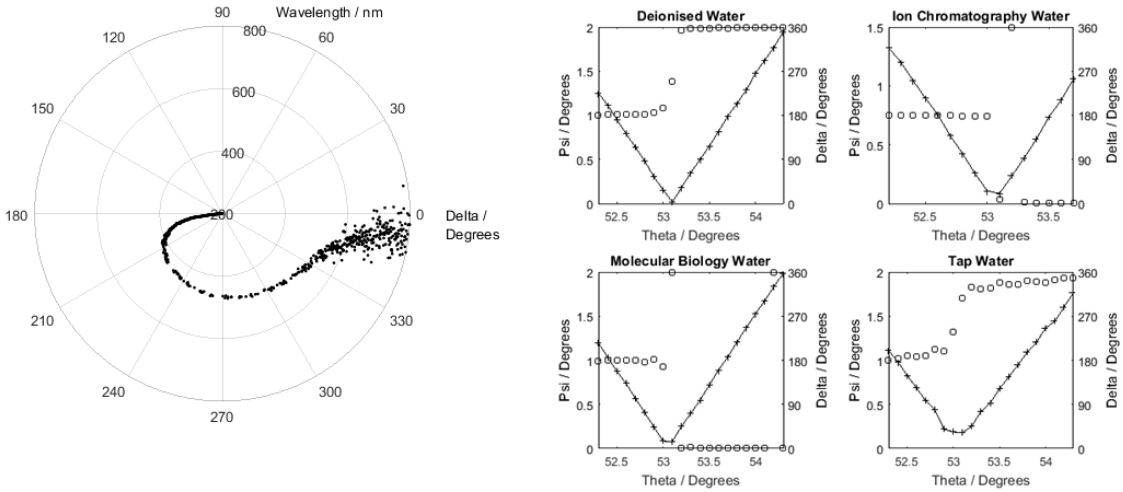

Figure 82 – Left, Polar plot of a Brewster angle ellipsometry experiment on deionised water showing a transition from 180° to 360°. Right, variable angle ellipsometry experiments showing the effect of purity on the measurement of Δ. Both high purity waters show a transition to 0°, while the lower purity samples show a transition to 360°.

Bibliography

1. Frederick, B. Y. Additivity of Intermolecular Forces at Interfaces. 1. Determination of the Contribution to Surface and Interfacial Tensions of Dispersion Forces in Various Liquids. *J. Phys. Chem.* **67,** 2538–2541 (1963).

2. Fowkes, F. M. Attractive Forces at Interfaces. *Ind. Eng. Chem.* **56,** 40–52 (1964).

3. Vargaftik, N. B., Volkov, B. N. & Voljak, L. D. International Tables of the Surface Tension of Water International Tables of the Surface Tension of Water. *Am. Inst. Phys.* **12,** 817–820 (2014).

4. Vazquez, G., Alvarez, E. & Navaza, J. M. Surface Tension of Alcohol + Water from 20 to 50 C. *J. Chem. Eng. Data* **40,** 611–614 (1995).

5. Surface Tension Database. Available at: surfacetension.de.

6. Hu, D. L., Chan, B. & Bush, J. W. M. The hydrodynamics of water strider locomotion. *Nature* **424,** 663–666 (2003).

7. Zisman, W. A. Relation of the Equilibrium Contact Angle to Liquid and Solid Constitution. *Adv. Chem.* 1–51 (1964).

8. Bhattacharyya, K., Sitzmann, E. V. & Eisenthal, K. B. Study of chemical reactions by surface second harmonic generation: p-Nitrophenol at the air–water interface. *J. Chem. Phys.* **87,** 1442 (1987).

9. Paluch, M. & Filek, M. Effect of para-substituted phenols on the surface potential and on the surface tension at the water/air interface. *J. Colloid Interface Sci.* **73,** 282–286 (1980).

10. Song, H., Kim, F., Connor, S., Somorjai, G. A. & Yang, P. Pt Nanocrystals : Shape Control and Langmuir - Blodgett Monolayer Formation. *J. Phys. Chem.* **109,** 188–193 (2005).

11. Tao, A. *et al.* Langmuir − Blodgett Silver Nanowire Monolayers for Molecular Sensing Using Surface-Enhanced Raman Spectroscopy. *Nano Lett.* **3,** 1229–1233 (2003).

12. Nagarajan, R. Self-Assembly : The Neglected Role of the Surfactant Tail †. *Langmuir* **18,** 31–38 (2002).

13. Asaki, T. J., Thiessen, D. B. & Marston, P. L. Effect of an Insoluble Surfactant on Capillary Oscillations of Bubbles in Water : Observation of a Maximum in the Damping. *Phys. Rev. Lett.*

75, 2686–2689 (1995).

14. Smith, R. D. & Berg, J. C. The collapse of surfactant monolayers at the air—water interface. *J. Colloid Interface Sci.* **74,** 273–286 (1980).

15. Garti, N., Wellner, E. & Sarig, S. Effect of Surfactants on Crystal Structure Modification of Stearic Acid. *J. Cryst. Growth* **57,** 577–584 (1982).

16. Avila, L. V. N., Saraiva, S. M. & Oliveira, J. F. Stability and collapse of monolayers of stearic acid and the effect of electrolytes in the subphase. *Colloids Surfaces A Physicochem. Eng. Asp.* **154,** 209–217 (1999).

17. Cui, X., Mao, S., Liu, M., Yuan, H. & Du, Y. Mechanism of Surfactant Micelle Formation. *Langmuir* **24,** 10771–10775 (2008).

18. Zana, R., Benrraou, M. & Rueff, R. Surfactants . 1 . Effect of the Spacer Chain Length on the Critical Micelle Concentration and Micelle Ionization Degree. *Langmuir* **7,** 1072–1075 (1991).

19. Domínguez, A., Fernández, A., González, N., Iglesias, E. & Montenegro, L. Determination of Critical Micelle Concentration of Some Surfactants by Three Techniques. *J. Chem. Educ.* **74,** 1227–1231 (1997).

20. Losche, M., Schmitt, J., Decher, G., Bouwman, W. G. & Kjaer, K. Detailed Structure of Molecularly Thin Polyelectrolyte Multilayer Films on Solid Substrates as Revealed by Neutron Reflectometry. *Macromolecules* **31,** 8893–8906 (1998).

21. Decher, G., Hong, J. D. & Schmitt, J. Buildup of ultrathin multilayer films by a self-assembly process : III . Consecutively alternating adsorption of anionic and cationic polyelectrolytes on charged surfaces. *Thin Solid Films* 831–835 (1992).

22. Bergeron, V. & Langevin, D. Monolayer Spreading of Polydimethylsiloxane Oil on Surfactant Solutions. *Phys. Rev. Lett.* **76,** 3152–3155 (1996).

23. Ulman, A. Formation and Structure of Self-Assembled Monolayers. *Chem. Rev.* **96,** 1533–1554 (1996).

24. Freeman, R. G. *et al.* Self-Assembled Metal Colloid Monolayers: An Approach to SERS Substrates. *Science (80-.).* **267,** 1629–1632 (1995).

25. Deng, K., Collins, R. J., Mehregany, M. & Sukenik, C. N. Performance Impact of Monolayer Coating of Polysilicon Micromotors. *J. Electrochem. Soc* **142,** 1278–1285 (1995).

26. Reina, A. *et al.* Large Area , Few-Layer Graphene Films on Arbitrary Substrates by Chemical Vapor Deposition 2009. *Nano Lett.* **9,** 30–35 (2009).

27. LANGMUIR, I. The Constitution and Fundamental Properties of Solids and Liquids. *J. Am. Chem. Soc.* **252,** (1916).

28. Peterlinz, K. A. & Georgiadis, R. In Situ Kinetics of Self-Assembly by Surface Plasmon Resonance Spectroscopy. *Langmuir* **7463,** 4731–4740 (1996).

29. Gibbs, J. W. On the Equilibrium of Heterogeneous Substances. *Trans. Conneticut Acad. Arts Sci.* **3,** 108–248 (1876).

30. Tarbuck, T. L. & Richmond, G. L. Adsorption and Reaction of CO 2 and SO 2 at a Water Surface. *JACS* **128,** 3256–3267 (2006).

31. Shultz, M. J. *et al.* International Reviews in Physical Chemistry Sum frequency generation spectroscopy of the aqueous interface : Ionic and soluble molecular solutions. *Int. Rev. Phys. Chem.* **19,** 123–153 (2010).

32. Jungwirth, P., Devlin, J. P., Buch, V., Milet, A. & Vacha, R. Water surface is acidic. *PNAS* **104,** 2–7 (2007).

33. Petersen, P. On the Nature of Ions at the Liquid Water Surface. *Annu. Rev. Phys. Chem.* 333–364 (2006). doi:10.1146/annurev.physchem.57.032905.104609

34. Beattie, J. K., Djerdjev, A. M. & Warr, G. G. The surface of neat water is basic. **141,** (2009).

35. Datta, S., Grant, D. J. W. & Hall, W. Crystal Structures of Drugs: Advances in Determination, Prediction and Engineering. *Nature* **3,** 42–57 (2004).

36. Hammond, C. *The Basics of Crystallography and Diffraction*. (1998).

37. Bloembergen, N., Lee, C. H., Chang, R. . & Jha, S. S. Optical Second-Harmonic Generation in Reflection from Media with Inversion Symmetry. *Phys. Rev.* **174,** 813–822 (1968).

38. Marsh, R. E. Some thoughts on choosing the correct space group. *Acta Crystallogr.* 897–907 (1995). doi:10.1107/S0108768195008901

39. Lee, A. Y., Erdemir, D. & Myerson, A. S. Crystal Polymorphism in Chemical Process Development. *Annu. Rev. Chem. Biomol. Eng.* 259–280 (2011). doi:10.1146/annurev-chembioeng-061010-114224

40. Hiremath, R., Basile, J. A., Varney, S. W. & Swift, J. A. Controlling Molecular Crystal

Polymorphism with Self-Assembled Monolayer Templates. *JACS* **127,** 18321–18327 (2005).

41. Braga, D., Grepioni, F., Maini, L. & Polito, M. Crystal Polymorphism and Multiple Crystal Forms. *Struct. Bond* 25–50 (2009). doi:10.1007/430

42. Moulton, B. & Zaworotko, M. J. From Molecules to Crystal Engineering : Supramolecular Isomerism and Polymorphism in Network Solids B . Crystal Engineering vs Crystal Structure. *Chem. Rev.* **101,** 1629–1658 (2001).

43. Huard, S. *Polarization of Light*. (1997).

44. Ward, I. M. Optical and Mechanical Anisotropy in Crystalline Polymers. *Proc. Phys. Soc.* **80,** 1176–1188 (1962).

45. Doyle, W. T. Graphical approach to Fresnel's equations for reflection and refraction of light. *Am. J. Phys.* 643–647 (2015).

46. Mccrackin, F. L., Passaglia, E., Stromberg, R. R. & Steinberg, H. L. Measurement of the Thickness and Refractive Index of Very Thin Films 1 and the Optical Properties of Surfaces by Ellipsometry. *J. Res. Natl. Bur. Stand. (1934).* **67,** 363–377 (1963).

47. Arwin, H. Ellipsometry on thin organic layers of biological interest : characterization and applications. *Thin Solid Films* 377–378 (2000).

48. Vedam, K. Spectroscopic ellipsometry : a historical overview. *Thin Solid Films* 1–9 (1998).

49. Brewster, D. On the Laws Which Regulate the Polarisation of Light by Reflexion from Transparent Bodies. *Philos. Trans. R. Soc. London* **105,** 125–159 (1815).

50. Hénon, S. & Meunier, J. Microscope at the Brewster angle : Direct observation of first-order phase transitions in monolayers Microscope at the Brewster transitions in monolayers angle : Direct observation of first-order phase. *Rev. Sci, Instrum.* **62,** 936–939 (1991).

51. Azzam, R. M. A. Division-of-amplitude Photopolarimeter (DOAP) for the Simultaneous Measurement of All Four Stokes Parameters of Light. *Int. J. Opt.* **29,** 685–689 (1982).

52. Franken, P. A. & Ward, J. . Optical Harmonics and Nonlinear Phenomena. *Rev. Mod. Phys.* **35,** 23–39 (1968).

53. Boyd, R. W. *Nonlinear Optics*. (2003).

54. Franken, A. P., Hill, A. E., Peters, C. W. & Weinreich, G. Generation of Optical Harmonics. *Phys. Rev. Lett.* **7,** 118–120 (1961).

55. Zipfel, W. R. *et al.* Live tissue intrinsic emission microscopy using multiphoton-excited native fluorescence and second harmonic generation. *PNAS* **100,** 7075–7080 (2003).

56. Wampler, R. D. *et al.* Selective detection of protein crystals by second harmonic microscopy. *J. Am. Chem. Soc.* **130,** 14076–7 (2008).

57. Wong, T. M., Byers, J. D., Yee, H. I. & Hicks, J. M. Circular Dichroism Spectroscopy at Interfaces: A Surface Second Harmonic Generation Study. *J. Phys. Chem.* **97,** 1383–1388 (1993).

58. Higgins, D. A., Abrams, M. B., Byerly, S. K. & Corn, R. M. Resonant Second Harmonic Generation Studies of p-Nitrophenol Adsoprtion at Condensed-Phase Interfaces. 1994–2000 (1994).

59. Chen, C., Wu, B., You, G., Jiang, A. & Huang, Y. High-Efficiency and Wide-Band Single-Harmonic-Generation Properties of the New Crystal β-BaB2O4. in *International Quantum Electronics Conference* MCC5 (Optical Society of America, 1984).

60. Kleinman, D. A. Theory of Second Harmonic Generation of Light. *Phys. Rev.* **128,** 1761–1775 (1962).

61. Fejer, M., Magel, G., Jundt, D. & Byer, R. Quasi-Phase-Matched Second Harmonic Generation: Tuning and Tolerances. *IEEE J. Quantum Electron.* **28,** 2631–2654 (1992).

62. Coppens, P. & Schmidt, G. M. J. The crystal structure of the α-modification of p -nitrophenol near 90° K. *Acta Crystallogr.* **18,** 62–67 (1965).

63. Coppens, P. & Schmidt, G. M. J. The crystal structure of the metastable (β) modification of p -nitrophenol. *Acta Crystallogr.* **18,** 654–663 (1965).

64. Hadzi, D., Novak, A. & Gordon, J. E. Infrared Spectra and Hydrogen Bonding in, Some Adducts of Phenols with Their Phenoxides and Other Oxygen Bases. **67,** 1118–1124 (1962).

65. Selvakumar, S., Susai, M., Babu, S. A., Ramalingam, S. & Rajesh, A. L. Crystal growth and DFT insight on sodium para- nitrophenolate para- nitrophenol dihydrate single crystal for NLO applications. *J. Mol. Struct.* **1125,** 1–11 (2016).

66. MINEMOTO, H., Ozaki, Y., SONODA, N., SASAKI, T. & Sasaki, N. S. Crystal Growth and the Nonlinear-Optical Properties of 4-Nitrophenol Sodium-Salt Dihydrate and Its Deuterated Material. *J. Appl. Phys.* **76,** 3975–3980 (1994).

67. Selvakumar, S., Boobalan, M. S., Anthuvan Babu, S., Ramalingam, S. & Leo Rajesh, A. Crystal

growth and DFT insight on sodium para-nitrophenolate para-nitrophenol dihydrate single crystal for NLO applications. *J. Mol. Struct.* **1125,** 1–11 (2016).

68. John, C. J., Amalanathan, M., Twinkle, A. R., Srinivasan, P. & Joe, I. H. Vibrational spectra and first order hyperpolarizability studies of dimethyl amino pyridinium 4-nitrophenolate 4-nitrophenol. *Spectrochim. Acta - Part A Mol. Biomol. Spectrosc.* **81,** 151–161 (2011).

69. Bhattacharyya, K., Sitzmann, E. V & Eisenthal, K. B. Study of chemical reactions by surface second harmonic generation: p-Nitrophenol at the air–water interface. *J. Chem. Phys.* **87,** 1442 (1987).

70. Shen, Y. R. Surface studies by optical second harmonic generation : An overview Surface studies by optical second harmonic generation : An overview. *J. Vac. Sci. Technol. B Microelectron. Process. Phenom.* **1464,** 3–6 (1985).

71. Heinz, T. F., Loy, M. M. T. & Thompson, W. A. Study of symmetry and disordering of Si(111)-7×7 surfaces by optical second harmonic generation. *J. Vac. Sci. Technol. B* **1467,** 1–5 (1985).

72. Hicks, J. M., Kemnitz, K. & Eisenthal, K. B. Studies of Liquid Surfaces by Second Harmonic Generation. *J. Phys. Chem.* 560–562 (1986).

73. Guyot-Sionnest, P., W.Chen & Shen, Y. R. General considerations on optical second-harmonic generation from surfaces and interfaces. *Phys. Rev. B* **33,** 8254–8263 (1986).

74. Castro, A., Ong, S. & Eisenthal, K. B. Studies of Molecular Properties at the Surface of a Liquid Jet by Second Harmonic Generation. *Chem. Phys. Lett.* **163,** 3–7 (1989).

75. Eisenthal, K. B. Liquid Interfaces Probed by Second-Harmonic and Sum-Frequency Spectroscopy. *Chem. Rev.* 1343–1360 (1996).

76. Sarkar, N., Das, K., Das, S., Nath, D. & Bhattacharyya, K. Effect of Urea and Surfactant on p-Nitrophenol at the Water Surface: A Surface Second-harmonic Generation Study. *J. Chem. Soc. Faraday Trans.* **91,** 1769–1773 (1995).

77. Das, K. *et al.* Salt effect on p-nitrophenol at the water surface: A surface second harmonic generation study. *J. Chem. Soc. - Faraday Trans.* **92,** 4993–4996 (1996).

78. Zhao, X., Goh, M. C. & Eisenthal, K. B. Effects of Long-chain Molecules on the Population and Orientation of Organic Molecules at the Air/Water Interface. *J. Phys. Chem.* **131,** 2222–2224 (1990).

79. Haslam, S., Croucher, S. G., Hickman, C. G. & Frey, J. G. Surface second harmonic generation

studies of the dodecane/water interface: the equilibrium and kinetic behaviour of p-nitrophenol and tri-n-butyl phosphate. *Phys. Chem. Chem. Phys.* **2,** 3235–3245 (2000).

80. Sagert, N. H., Lee, W. & Quinn, M. J. The adsorption of tri-n-butylphosphate at the n-dodecane-water interface. *Can. J. Chem.* **57,** 1218–1223 (1979).

81. Abdel-Kader, M. M., Gwaily, S. E. & El Zayat, M. Y. Phase Transitions in Some Hydrogen-Bonded Molecules. *Phys. Status solidi* **57,** 49–57 (2002).

82. Wojcik, G. & Mossakowska, I. Polymorphs of p -nitrophenol as studied by variable-temperature X-ray diffraction and calorimetry : comparison with m -nitrophenol research papers. *Acta Crystallogr. Sect. B* **62`,** 143–152 (2006).

83. Fritzsche, J. Ueber die Producte der Einwirkung der Salpeter- saure auf die Phensaure; *Adv. Synth. Catal.* **5,** 150–167 (1859).

84. Kulkarni, G. U., Kumaradhas, P. & Rao, C. N. R. Charge Density Study of the Polymorphs of p -Nitrophenol. *Chem. Mater.* **10,** 3498–3505 (1998).

85. KUMARADHAS, P., GOPALAN, R. S. & KULKARNI, G. U. A charge density study of the effect of irradiation on the a-form. *Proc. Indian Acad. Sci.* **3,** 569–579 (1999).

86. Kulkarni, G. U., Kumaradhas, P. & Rao, C. N. R. Charge Density Study of the Polymorphs of p -Nitrophenol. 3498–3505 (1998).

87. Antherton, N. M., Heath, J. P., Shohoji, M. C. B. & Torrance, C. A. Single-crystal ENDOR study of γ-irradiated p-nitrophenol. *J. Chem. Soc., Faraday Trans.* **86,** 3197–3200 (1990).

88. Bejan, I. *et al.* The photolysis of ortho-nitrophenols: a new gas phase source of HONO. *Phys. Chem. Chem. Phys.* **8,** 2028–2035 (2006).

89. Ernst, H. a. *et al.* Ultrafast Dynamics of o -Nitrophenol: An Experimental and Theoretical Study. *J. Phys. Chem. A* **119,** 9225–9235 (2015).

90. Grygoryeva, K. *et al.* Photochemistry of Nitrophenol Molecules and Clusters: Intra- vs Intermolecular Hydrogen Bond Dynamics. *J. Phys. Chem. A* **120,** 4139–4146 (2016).

91. Wong, J. M., Li, Q. X., Hammock, B. D. & Seiber, J. N. Method for the Analysis of 4-Nitrophenol and Parathion in Soil Using Supercritical Fluid Extraction and Immunoassay. *J. Agric. Food Chem.* **39,** 1802–1807 (1991).

92. Tremp, J., Mattrel, P., Fingler, S. & Giger, W. Phenols and nitrophenols as tropospheric

pollutants: Emissions from automobile exhausts and phase transfer in the atmosphere. *Water. Air. Soil Pollut.* **68,** 113–123 (1993).

93. Chen, D. & Ray, A. K. Photodegradation Kinetics of 4-Nitrophenol in TiO2 Suspension. *Wat. Res.* **32,** 3223–3234 (1998).

94. Zhang, W. *et al.* Kinetics , degradation pathway and reaction mechanism of advanced oxidation of 4-nitrophenol in water by a UV / H 2 O 2 process. *J. Chem. Technol. Biotechnol.* **794,** 788–794 (2003).

95. Lifka, J., Ondruschka, B. & Hofmann, J. The Use of Ultrasound for the Degradation of Pollutants in Water: Aquasonolysis – A Review. *Eng. Life Sci.* **3,** 253–262 (2003).

96. Oturan, M. A., Peiroten, J., Chartrin, P. & Acher, A. J. Complete Destruction of p-Nitrophenol in Aqueous Medium by Electro-Fenton Method. *Environ. Sci. Technol.* **34,** 3474–3479 (2000).

97. Bhatnagar, A. & Sillanpää, M. Utilization of agro-industrial and municipal waste materials as potential adsorbents for water treatment — A review. *Chem. Eng. J.* **157,** 277–296 (2010).

98. Bhatnagar, A. & Minocha, A. K. Conventional and non-conventional adsorbents for removal of pollutants from water – A review. *Indian J. Chem. Technol.* **13,** 203–217 (2006).

99. Shnidman, B. Y. L. The solubility of urea in water. (1932).

100. Vijayan, N., Ramesh Babu, R., Gunasekaran, M., Gopalakrishnan, R. & Ramasamy, P. Growth, optical, thermal and mechanical studies of methyl 4-hydroxybenzoate single crystals. *J. Cryst. Growth* **256,** 174–182 (2003).

101. Srinivasan, K., Biravaganesh, R., Gandhimathi, R. & Ramasamy, P. Growth and characterization of NMBA (4-nitro-4 0 -methyl benzylidene aniline) single crystals. **236,** 381–392 (2002).

102. Srinivasan, K., Sankaranarayanan, K., Thangavelu, S. & Ramasamy, P. Influence of organic solvents on the habit of NMBA (4-nitro-4 -methyl benzylidene aniline) crystals. **212,** 246–254 (2000).

103. Bailey, R. T., Cruickshank, F. R., Pugh, D. & Sherwood, J. N. Growth perfection and properties of organic non-linear materials. *Acta Crystallogr. Sect. A Found. Crystallogr.* **47,** 145–155 (1991).

104. P. Kerkoc, M. Zgonik, K. Sutter, Ch. Bosshard, and P. G. 4-(N,N-Dimethylamino)-3-acetamidonitrobenzene single crystals for nonlinear-optical applications. **7,** (1990).

105. Baumert, J.-C., Twieg, R. J., Bjorklund, G. C., Logan, J. a. & Dirk, C. W. Crystal growth and characterization of 4-(N,N-dimethylamino)-3-acetamidonitrobenzene, a new organic material for nonlinear optics. *Appl. Phys. Lett.* **51,** 1484 (1987).

106. Tseng, H.-C., Lee, C.-Y., Weng, W.-L. & Shiah, I.-M. Solubilities of amino acids in water at various pH values under 298.15K. *Fluid Phase Equilib.* **285,** 90–95 (2009).

107. Zhou, X. *et al.* Solubility of l-phenylalanine in water and different binary mixtures from 288.15 to 318.15K. *Fluid Phase Equilib.* **316,** 26–33 (2012).

108. Wojcik, G. & Mossakowska, I. Polymorphs of p-nitrophenol as studied by variable-temperature X-ray diffraction and calorimetry: Comparison with m-nitrophenol. *Acta Crystallogr. Sect. B Struct. Sci.* **62,** 143–152 (2006).

109. Kissick, D. J., Wanapun, D. & Simpson, G. J. Second-order nonlinear optical imaging of chiral crystals. *Annu. Rev. Anal. Chem. (Palo Alto. Calif).* **4,** 419–37 (2011).

110. Kogut, A. D. & Pogorzelski, S. J. Kinetics of marine surfactant adsorption at an air / water interface . Baltic Sea studies *. **43,** (1981).

111. Beaglehole, D. Ellipsometry of Liquid Surfaces. *J. Phys. Colloq.* **44,** 147–154 (1983).

112. Beaglehole, D. Thickness of the Surface of Liquid Argon near the Triple Point. *Phys. Rev. Lett.* **43,** 2016–2018 (1979).

113. Penfold, J. The structure of the surface of pure liquids. *Rep. Prog. Phys.* **64,** 777–814 (2001).

114. Beaglehole, D. Structural changes in the surface of water. *J. Phys. Chem.* **91,** 5091–5092 (1987).

115. Greef, R. & Frey, J. G. The water-like film on water. *phys. stat. sol.* **1186,** 1184–1186 (2008).

116. Stocco, A. & Tauer, K. High-resolution ellipsometric studies on fluid interfaces. *Eur. Phys. J. E* **438,** 431–438 (2009).

117. Tarazona, P. & Chacón, E. Monte Carlo intrinsic surfaces and density profiles for liquid surfaces. *Phys. Rev. B* **70,** 235407 (2004).

118. Matsumoto, M. & Kataoka, Y. Study on liquid–vapor interface of water. I. Simulational results of thermodynamic properties and orientational structure. *J. Chem. Phys.* **88,** 3233–3245 (1988).